A Model Study of the Relative Influences of Scavenging and Circulation on ^{230}Th and ^{231}Pa in the western North Atlantic

Paul Lerner*[a], Olivier Marchal[b], Phoebe J. Lam[c], Wilford Gardner[d], Mary Jo Richardson[d], and Alexey Mishonov[e]

[a] *Goddard Institute for Space Studies, New York City, NY 10026, USA*
[b] *Woods Hole Oceanographic Institution, Woods Hole, MA 02543, USA*
[c] *University of California Santa Cruz, Santa Cruz, CA 95064, USA*
[d] *Texas A&M University, College Station, TX 77843, USA*
[e] *Earth System Science Interdisciplinary Center, University of Maryland, College Park, MD 20740, USA*

October 17, 2019

*Corresponding Author. Address: Goddard Institute for Space Studies, 2880 Broadway, NYC, NY (Tel:1-212-678-5548)
email address: paul.lerner@nasa.gov

ABSTRACT

The oceanic cycles of thorium-230 and protactinium-231 are affected by a number of processes, such as removal by adsorption to settling particles and transport by ocean currents. Measurements obtained as part of GEOTRACES and earlier programs have shown that, in the North Atlantic, the activities of dissolved ^{230}Th (^{230}Th$_d$) and ^{231}Pa (^{231}Pa$_d$) at abyssal depths are lower near the western margin than in the basin interior. At least two factors could explain the lower ^{230}Th$_d$ and ^{231}Pa$_d$ near the margin: (i) intensified scavenging in benthic nepheloid layers (BNLs) extending a thousand meters or more above the seafloor; and (ii) ventilation by relatively ^{230}Th$_d$- and ^{231}Pa$_d$-poor waters emanating from the Deep Western Boundary Current (DWBC).

Here a regional ocean circulation model with 'eddy-permitting' resolution (1/4°) that incorporates ^{230}Th and ^{231}Pa is used in an effort to reproduce the observed distributions of ^{230}Th and ^{231}Pa in the western North Atlantic. In this model, ^{230}Th and ^{231}Pa removal from solution is governed by a prescribed distribution of particulate matter that is derived from a recent synthesis of nephelometer and transmissometer data. The model simulates a meandering Gulf Stream and a DWBC along the continental slope and rise, although noticeable differences with physical observations also exist. A model solution is found that explains most of the variance of ^{230}Th$_d$ measurements (85%) and ^{231}Pa$_d$ measurements (81%) from (pre-)GEOTRACES cruises. On the other hand, measurements of particulate ^{230}Th (^{230}Th$_p$) and ^{231}Pa (^{231}Pa$_p$) are more difficult to reproduce, with the same solution accounting for only 49% (11%) of the ^{230}Th$_p$ (^{231}Pa$_p$) variance. Sensitivity experiments suggest that the low ^{230}Th$_d$ and ^{231}Pa$_d$ activities observed near the western margin are due to enhanced removal rates of both nuclides in BNLs rather than to deep water ventilation from the western boundary. The radionuclide activities present in the DWBC at its inflow location are also found to strongly influence the basin-scale distributions of ^{230}Th and ^{231}Pa. Overall, our study points to BNLs as important sites of ^{230}Th and ^{231}Pa scavenging in the ocean and illustrates the difficulty to explain simultaneously radionuclide measurements in dissolved and particulate forms in the studied area.

Keywords: ^{230}Th, ^{231}Pa, regional ocean circulation model, Deep Western Boundary Current, reversible exchange, particle concentration effect, nepheloid layer

1. Introduction

Thorium-230 (half-life of 75.6 kyr; Cheng et al. (2013)) and protactinium-231 (32.8 kyr; Robert et al. (1969)) are two naturally-occurring radioisotopes that are produced from the radioactive decay of uranium-234 and uranium-235, respectively. Uranium isotopes display quasi-conservative behaviour in seawater and concentrations proportional to salinity (e.g., Owens et al. (2011)), so that the production rates of ^{230}Th and ^{231}Pa are expected to be approximately uniform in the world's oceans. Both ^{230}Th and ^{231}Pa are thought to be removed from the water column through a reversible exchange (adsorption and desorption) with settling particles (Nozaki et al. 1981; Bacon and Anderson 1982), a process often referred to as 'particle scavenging'. A convenient measure of the intensity of particle scavenging is provided by the distribution coefficient, $K_D = A_p/(A_d P)$, where A_d (A_p) is the activity (in units of dpm) of the radionuclide in the dissolved (particulate) phase per kg of seawater and P is the bulk particle concentration in units of grams of particles per gram of seawater. In the open ocean, K_D for ^{230}Th is typically of the order of 10^7 g g^{-1}, indicating a strong tendency for Th to adsorb onto marine particles, whereas K_D for ^{231}Pa is generally lower by one order of magnitude (Moran et al. 2002; Hayes et al. 2015a). As a result of their different sensitivities to particle scavenging, Th and Pa represent two model types for the fate of trace metals, Th being removed from the open ocean primarily by settling particles and Pa largely by lateral transport to other environments (Anderson et al. 1983b,a; Henderson and Anderson 2003).

The distributions of ^{230}Th and ^{231}Pa in the North Atlantic have been documented in a number of studies. Early work showed that the activities of dissolved ^{230}Th (^{230}Th$_d$) or dissolved ^{231}Pa (^{231}Pa$_d$) from distant locations exhibit a similar increase with depth in the upper $\sim$ 1000 m of the water column but present large horizontal variations in the abyssal region below (for syntheses see Marchal et al. (2007); Luo et al. (2010)). More recently, the distributions of ^{230}Th and ^{231}Pa in both dissolved and particulate forms have been determined with unprecedented horizontal and vertical resolutions along the U.S. GEOTRACES North Atlantic section GA03 (Hayes et al. 2015a). Consistent with pre-GEOTRACES data, ^{230}Th$_d$ or ^{231}Pa$_d$ from distant locations showed a similar increase with depth in the upper 1000 m but large lateral variations at greater depths. Below about 1000 m, stations west of Bermuda displayed lower ^{230}Th$_d$ and ^{231}Pa$_d$ than stations east of Bermuda (Fig. 1).

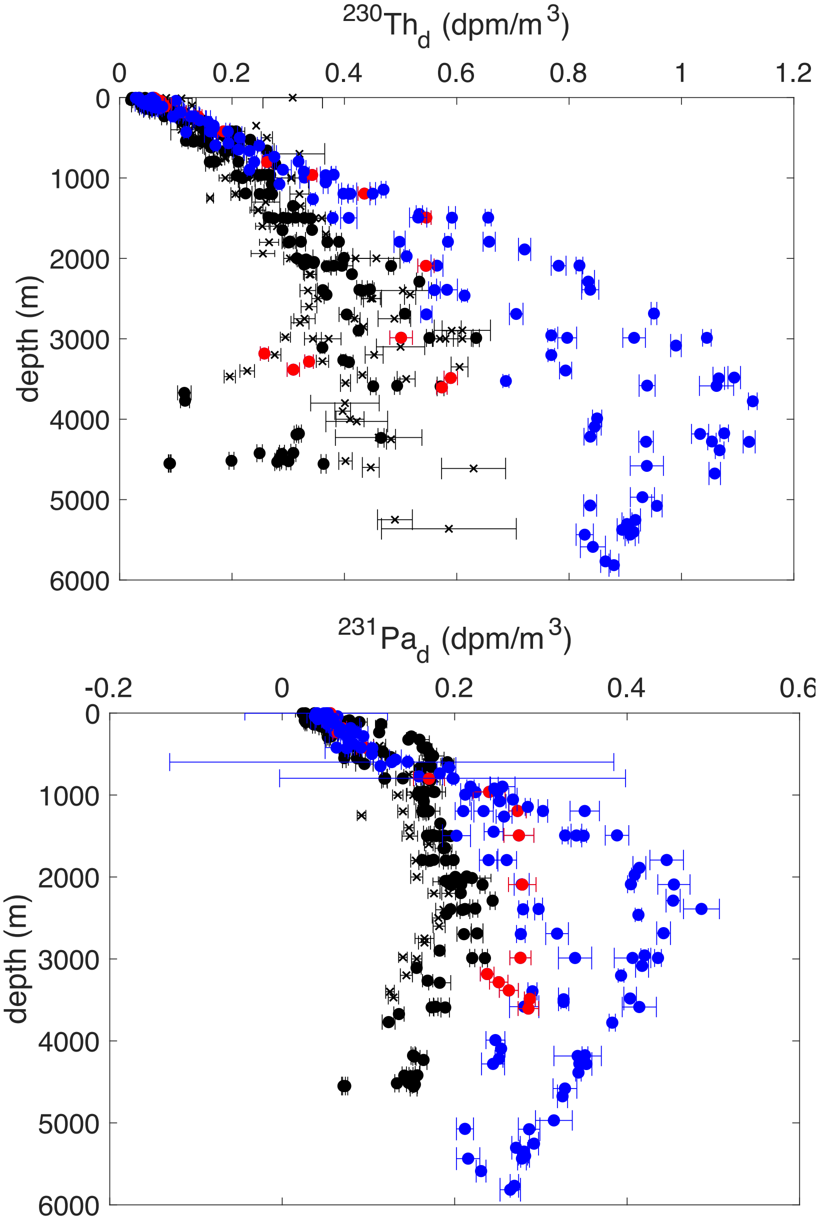

Fig. 1. Vertical profiles of dissolved ^{230}Th and ^{231}Pa activities in the North Atlantic. Data from stations west (east) of Bermuda are shown with black (blue) circles and data from station GT11-16, near the TAG hydrothermal vent, are shown with red circles. The horizontal bars show the measurement uncertainties (see Table 1 for data sources).

At stations west of Bermuda, $^{230}\mathrm{Th}_d$ and $^{231}\mathrm{Pa}_d$ increased with depth down to about 2000–4000 m but decreased with depth below. Whereas the activity increase with depth observed in the upper part of the water column is consistent with a reversible exchange of Th and Pa with settling particles (Bacon and Anderson 1982), the reversal in the vertical activity gradient at mid-depth and the large horizontal activity gradients in the deeper part await further investigation.

At least three factors could explain the departures of $^{230}\mathrm{Th}_d$ and $^{231}\mathrm{Pa}_d$ measurements from the profiles expected from reversible exchange: (i) spatial variations in particle scavenging due to variations in bulk particle concentration, (ii) spatial variations in particle scavenging due to variations in particle composition, and (iii) the ventilation of deep layers by components of the North Atlantic Deep Water (NADW). Each of these factors is introduced in turn below.

Particle scavenging in oceanic waters appears to vary with bulk particle concentration (P). Two observed characteristics of metal sorption in natural waters are in apparent contradiction with physico-chemical adsorption theory: (i) the time scales of sorption reactions are long, reaching days to weeks and more, and (ii) K_D is negatively correlated with particle concentration – the so-called particle concentration effect (e.g., Honeyman and Santschi (1989)). Colloids have for a long time been invoked to explain the slow Th sorption kinetics (e.g., Tsunogai and Minagawa (1978)). In the model developed by these authors, dissolved Th species rapidly and irreversibly adsorb onto colloidal particles, which then reversibly aggregate with larger filterable particles. Santschi et al. (1986) proposed that if the sorption of a metal ion has particle aggregation as a rate-limiting step, then the rate of sorption should vary with particle number or particle concentration. In the Brownian-pumping model, both characteristics (i-ii) result from the same underlying processes: the rapid formation of metal-colloid surface site complexes (adsorption) and the slow coagulation of colloids with filterable particles (Honeyman and Santschi 1989). More generally, the negative correlation between K_D and P could arise from at least two factors: (i) higher concentrations of Th-binding colloids, small enough to pass through typical filters, may keep apparent Th concentrations high in the 'dissolved' phase, and (ii) the surface area per mass of particles may decrease at greater particle mass, which would reduce the number of available binding sites (Henderson et al. 1999; Pavia et al. 2018). Owing to their high specific surface area and complexation capacity, colloidal particles may be of great importance in the cycling of particle-reactive elements (e.g., Guo et al. (1997)), and laboratory studies suggested that they could significantly influence Th scavenging in oceanic waters (e.g., Guo et al. (1997); Quigley et al. (2001, 2002)).

The ^{230}Th, ^{231}Pa, and particle data collected along GA03 indicated that particle concentration influences solid-solution partitioning and sorption rates in North Atlantic waters (Hayes et al. 2015b; Lerner et al. 2017). Hayes et al. (2015b) found that K_D for ^{230}Th and ^{231}Pa generally decreased with particle concentration along GA03. Lerner et al. (2017) derived estimates of the apparent first-order rate constant for Th adsorption onto particles (k_1) from an inversion of size-fractionated ^{228,230,234}Th and particle data gathered at eleven stations east of Bermuda. They found that k_1 generally decreases with depth, with the time scale $1/k_1$ averaging 1.0 yr in the upper 1000 m and (1.4 – 1.5) yr below. A positive relationship between k_1 and P was found, consistent with the notion that k_1 increases with the number of surface sites available for adsorption (e.g., Honeyman et al. (1988)). In contrast to the influence of colloids as envisioned by the Brownian pumping hypothesis, Lerner et al. (2017) provided evidence that the particle concentration effect may arise from the joint effect of P on the rate constants for Th attachment to, and detachment from, particles.

Particle scavenging could be intensified at abyssal depths in the western North Atlantic due to the presence of benthic nepheloid layers (BNLs) (Fig. 2). Vertical traces from nephelometers have long revealed that BNLs are common near the western margin in depths greater than 3000 m where a clear water minimum is typically found; in contrast to the western basins, the eastern basins generally show low turbidity (Eittreim et al. 1969, 1976; Biscaye and Eittreim 1977). A recent synthesis of light scattering and attenuation data illustrated that the particle load in excess of the concentration at the clear water minimum decreases eastward in the western North Atlantic by up to one order of magnitude (Gardner et al. 2017). In line with this result, particulate matter concentrations estimated from size-fractionated particle composition data featured intense BNLs along GA03 in the western North American margin with $P > 1000$ mg m^{-3}, two to three orders of magnitude higher than in surrounding waters (Lam et al. 2015). These observations suggest that intensified scavenging due to high particle concentrations could contribute to the relatively low ^{230}Th$_d$ and ^{231}Pa$_d$ in the deep waters west of Bermuda.

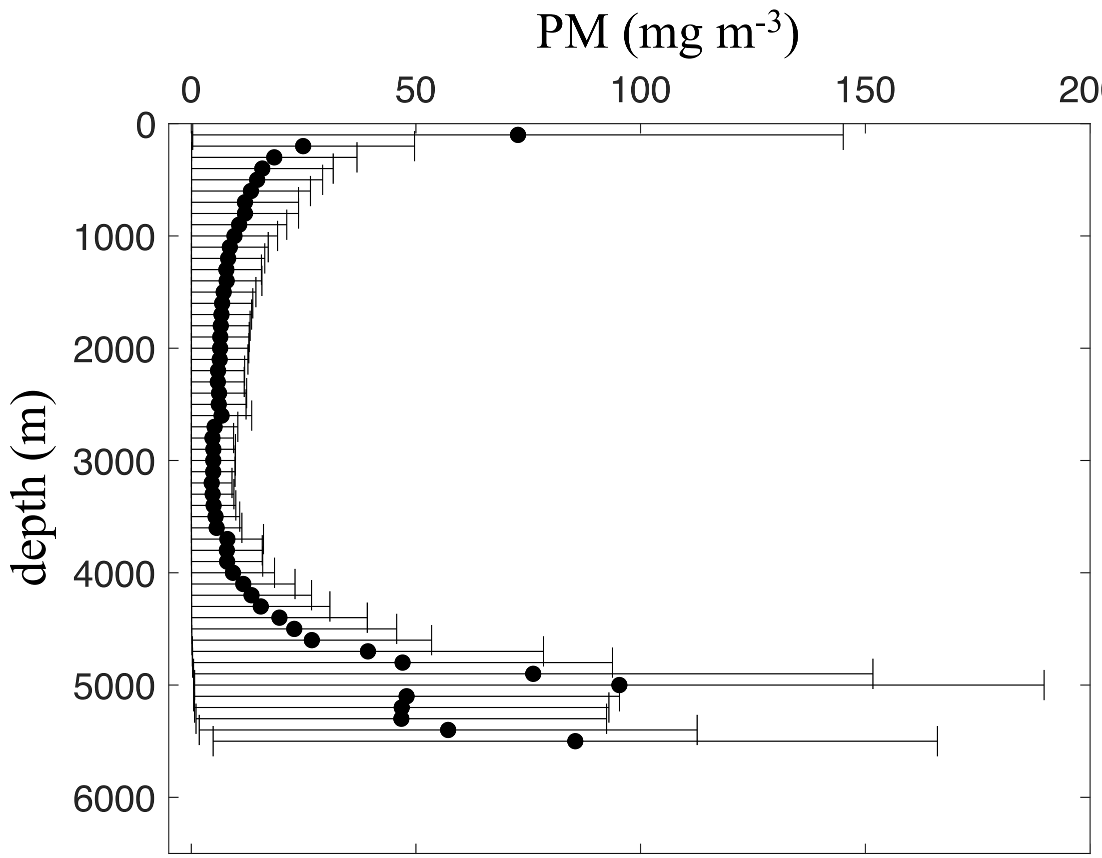

Fig. 2. Regionally averaged vertical profile of particulate matter (PM) concentration in the western North Atlantic. Each circle is an average based on (i) optical measurements converted empirically to PM concentration and (ii) a linear interpolation at the same vertical levels of the concentration estimates obtained from optical profiles at different stations. The horizontal bars show the standard errors of the averages (data compilation from Gardner et al. (2017)).

Particle scavenging in the ocean seems to vary also with the chemical composition of particles (e.g., Anderson et al. (1983a); Chase et al. (2002); Geibert and Usbeck (2004); Scholten et al. (2005); Roberts et al. (2009); Chuang et al. (2013); Lin et al. (2014)). A number of studies provided evidence for a role of particle composition on the sorption of ^{230}Th and ^{231}Pa in North Atlantic waters. Roy-Barman et al. (2005) reported that ^{230}Th of particles collected by sediment traps deployed in the eastern North Atlantic is positively correlated with Mn, Ba, and lithogenic fractions and does not covary with $CaCO_3$ or biogenic silica (bSi). Radioisotope and particle data from section GA03 provided further insight into the effects of particle type on Th and Pa scavenging in the North Atlantic (Hayes et al. 2015b; Lerner et al. 2018).

Hayes et al. (2015b) inferred enhanced scavenging by authigenic Fe and Mn (hydr)oxides in the form of hydrothermal particles emanating from the Middle Atlantic Ridge (MAR) and particles resuspended from reducing environments near the seabed off the West African coast. Biogenic silica was not found to be a significant scavenging phase for Th and Pa, presumably because of its low abundance and small variance at the sampled stations. Lerner et al. (2018) examined the dependence of their k_1 estimates (below about 100 m) on particle composition (particulate organic C, $CaCO_3$, bSi, lithogenic material, and Fe and Mn (hydr)oxides) at stations east of Bermuda. Particle composition was found to explain a larger fraction of k_1 variance for stations within the Mauritanian upwelling region ('eastern stations') than for stations west of that region ('western stations'). The k_1 variance explained by particle composition was mainly due to biogenic particles at the 'eastern stations' and to Mn oxides at the 'western stations'. Interestingly, the proportions of k_1 variance explained by particle composition and particle concentration were not significantly different (Lerner et al. 2018).

In addition to variations in particle scavenging intensity, ventilation of the deep basins by components of NADW has been postulated to impact the distributions of $^{230}\mathrm{Th}_d$ and $^{231}\mathrm{Pa}_d$ in the North Atlantic (e.g., Moran et al. (1997); Vogler et al. (1998); Moran et al. (2002)). The Deep Western Boundary Current (DWBC) in the western North Atlantic transports cold waters from the northern North Atlantic toward the equatorial region (e.g., Schmitz and McCartney (1993)) and appears to act as a major conduit from which deep layers in the North Atlantic are ventilated. The dynamical processes responsible for the ventilation of deep basins from the western boundary are varied and complex, involving, e.g., recirculation gyres (e.g., Hogg et al. (1986); Pickart and Hogg (1989)), mesoscale eddies (e.g., Pickart et al. (1997)), offshore entrainment in the region where the DWBC and the Gulf Stream cross over (e.g., Bower and Hunt (2000a,b)), deep cyclones accompanying meander troughs in the Gulf Stream path (e.g., Andres et al. (2016)), and stirring between the boundary and the interior (e.g., Le Bras et al. (2017, 2018)).

Tracer measurements have shed considerable light on deep ventilation in the North Atlantic. Tritium and excess helium-3 data indicated that the deep water in the subpolar gyre is ventilated by NADW on time scales of about 10–15 yr (Doney and Jenkins 1994). Chlorofluorocarbon (CFC) data showed that deep layers in the North Atlantic are renewed on decadal time scales by Labrador Sea Water (LSW) and Denmark Strait Overflow Water (DSOW) originating from the western boundary (e.g., Rhein et al. (2015)). From multiple tracer data collected along GA03, Holzer et al. (2018) estimated that abyssal waters have a mean age ranging from 200 to 400 yr and are younger in the western basins. Overflow waters last ventilated in the Arctic Ocean and in the Norwegian and Greenland Seas would contribute about 40% of waters present in the western basins where $\sim$60% of these overflow waters are younger than 160 yr (Holzer et al. 2018).

Early measurements of $^{230}\mathrm{Th}_d$ in the Labrador Sea and the Denmark Strait presented relatively small values compared to those observed at more southern locations in the Atlantic Ocean (Moran et al. 1995, 1997, 2002), suggesting that ventilation by LSW and DSOW would tend to decrease $^{230}\mathrm{Th}_d$ in the deep North Atlantic. Similarly, recent measurements obtained on filtered seawater collected in the Labrador Sea, Irminger Sea, Iceland Basin, and West European Basin along GEOTRACES section GA01 (Deng et al. 2018) showed $^{230}\mathrm{Th}_d$ and $^{231}\mathrm{Pa}_d$ activities that are lower than those measured further south in the Atlantic Ocean. The low $^{230}\mathrm{Th}_d$ and $^{231}\mathrm{Pa}_d$ near the bottom in the Labrador Sea and Irminger Sea appeared to be related to the presence of young (e.g., CFC-rich) waters, whilst enhanced scavenging of both nuclides near the seafloor would also occur in overflow waters (Deng et al. 2018).

In summary, at least two processes could contribute to the relatively low $^{230}\mathrm{Th}_d$ and $^{231}\mathrm{Pa}_d$ observed at abyssal depths in the western North Atlantic: (i) intensified particle scavenging in thick or rapidly cycling BNLs and (ii) ventilation by $^{230}\mathrm{Th}_d$- and $^{231}\mathrm{Pa}_d$-poor components of NADW from the western boundary. In this paper, we apply a regional ocean circulation model in order to study the effects of these two processes on the distributions of both radionuclides. The model is configured to represent the western North Atlantic with 'eddy-permitting' ($1/4°$) resolution and includes a description of $^{230}\mathrm{Th}$ and $^{231}\mathrm{Pa}$ cycling. In this description, the rates of $^{230}\mathrm{Th}$ and $^{231}\mathrm{Pa}$ removal from solution are determined by a prescribed distribution of particulate matter concentration based on a recent compilation of nephelometer and transmissometer data. Results from the circulation-scavenging model are then compared to (i) physical oceanographic observations provided from satellite altimetry and repeat sections between the New England continental shelf and Bermuda; and (ii) radionuclide measurements obtained from (pre-)GEOTRACES cruises. Finally, numerical experiments are performed with the model in order to evaluate the sensitivity of the simulated distributions of $^{230}\mathrm{Th}$ and $^{231}\mathrm{Pa}$ in both dissolved and particulate forms to (i) the intensity of particle scavenging, (ii) the strength of the DWBC, and (iii) the radionuclide activities that are present in the DWBC.

Thorium-230 and protactinium-231 have been incorporated in ocean models in previous studies. Both tracers have been included in three-dimensional (3D) models of global ocean circulation (Henderson et al. 1999; Siddall et al. 2005; Dutay et al. 2009; Rempfer et al. 2017; Gu and Liu 2017; van Hulten et al. 2018), in a zonally-averaged circulation model (Marchal et al. 2000), in a 2D (latitude-depth) box model (Luo et al. 2010), and in 3D regional inverse models (Marchal et al. 2007; Burke et al. 2011). Most of these studies were aimed at testing paleoceanographic applications of $^{230}\mathrm{Th}$ and $^{231}\mathrm{Pa}$, more specifically the use of sediment $^{230}\mathrm{Th}$ activity data to correct accumulation rates for the effects of sediment redistribution (Bacon 1984) and the use of the $^{231}\mathrm{Pa}/^{230}\mathrm{Th}$ ratio from Atlantic sediments as a paleocirculation indicator (Yu et al. 1996). The present work complements these earlier studies by isolating the relative influences of particle scavenging and ocean circulation on radionuclide distributions in the western North Atlantic using a model with higher horizontal resolution and a treatment of sorption kinetics that relates specific rates of adsorption to a particle concentration field derived from optical data. On the other hand, our model does not account for fluxes of radionuclides from the seafloor such as due to sediment resuspension (e.g., Rutgers van der Loeff and Boudreau (1997)). Emphasis is placed on understanding water column measurements, although our results may also have implications for the interpretation of sediment records of ^{230}Th and ^{231}Pa.

The remainder of this paper is organized as follows. In section 2, the physical, radionuclide, and optical data sets used in this study are briefly described. Nephelometer and transmissometer data are converted into estimates of particulate matter (PM) concentration using published calibrations, and an estimate of the 3D distribution of PM concentration in the study area is derived. The ocean model is presented in section 3. The physical and geochemical components of the model are detailed, together with the conditions imposed at the surface and at the open boundaries of the regional domain. In section 4, a particular model solution is presented that shows relatively good agreement with physical oceanographic and radionuclide data. The influences of particle scavenging intensity and of DWBC properties (strength and radionuclide contents) are then illustrated in section 5 through a number of sensitivity experiments. Our results are discussed in section 6, with emphasis on the role of BNLs in particle scavenging. A summary and perspectives follow in section 7.

2. Data

a. Physical Data

This study relies on a number of physical datasets. Bathymetric data used to establish the model bottom topography are obtained from ETOPO2 version 2 (ETOPO2v2 2006), a gridded product with 2-min resolution and derived from satellite altimeter and shipboard sounding data. Temperature and salinity data employed to constrain the initial and boundary conditions of the model (section 4 and appendix C) are obtained from the 1/4° resolution climatology (decadal averages, objectively analyzed) of the World Ocean Atlas (Locarnini et al. 2013; Zweng et al. 2013). Climatologic values of potential temperature are first derived from the values of in situ temperature, salinity, and depth of the Atlas using the algorithm developed by Jackett et al. (2004) and assuming 1 dbar = 1 m. Potential temperature and salinity data at model levels are then obtained from their respective climatologic values by linear interpolation (and extrapolation, where needed). Note that the longitudes and latitudes of model grid points are set to coincide with the longitudes and latitudes of the climatologic grid, so no horizontal interpolation is necessary.

Two types of satellite data sets are used in this study. First, surface wind stresses used to provide the mechanical forcing to the model come from the Scatterometer Climatology of Ocean Winds, SCOW (Risien and Chelton 2008). The monthly means of zonal and meridional wind stresses, available at 1/4° resolution, are averaged to produce an annual mean field. The annual mean wind stresses at a given model grid point are then obtained from the closest values of the climatologic fields. Second, observations of dynamic topography are used in order to test the modeled circulation. Monthly observations of sea surface height (SSH) between 1993–2012 are derived from satellite altimetry maps prepared by Ssalto/Duacs and distributed by Aviso+, with support from CNES (`https://www.aviso.altimetry.fr`). These observations are averaged to produce a multi-year annual mean field which is compared to model results.

Finally, horizontal velocity data from line W, between the New England continental shelf and Bermuda, and coinciding with the western segment of GA03 (Fig. 3), are used to provide another test of the modeled circulation. Velocity measurements along line W were obtained from shipboard deployments of Lowered Accoustic Doppler Current Profilers and from moored profiler and current meters between 2004 and 2014 (Toole et al. 2017). The velocity data used in this study are 10-yr averages derived by averaging daily profiles of subinertial-filtered velocity (note that the eastern-most mooring only contains data between 2008 and 2014, so only 6-yr averages are used for that mooring). The daily profiles were constructed by combining moored profiler and current meter data from six moorings deployed along line W (John Toole, personal communication).

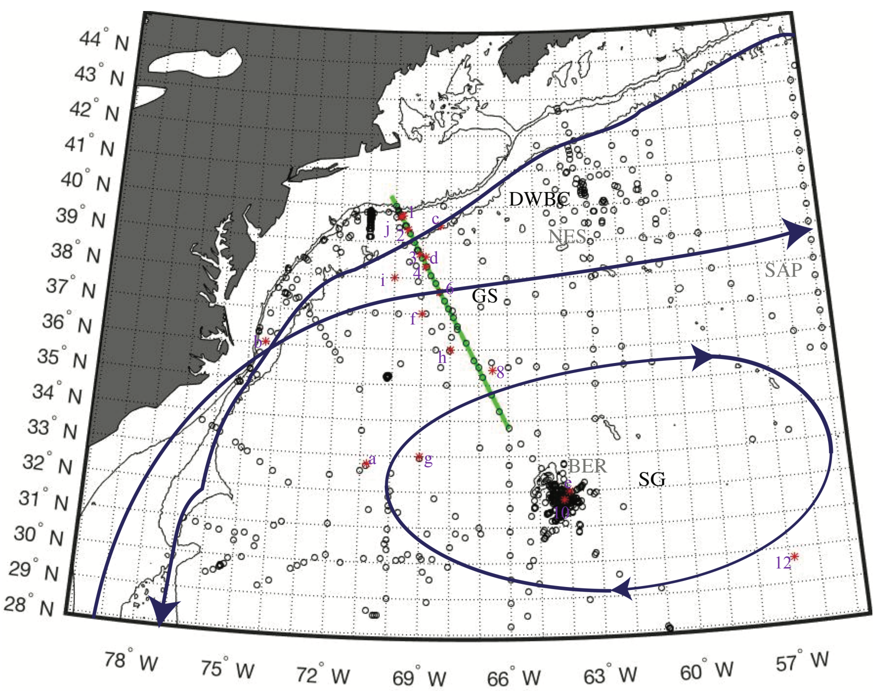

Fig. 3. Map of the study area showing the location of GEOTRACES stations (red stars with numerals), pre-GEOTRACES stations (red stars with letters), and nephelometer and transmissmeter stations (circles). Black lines are isobaths of 200, 1000, and 3000 m, and blue arrows show schematic pathways of

the Gulf Stream (GS), Deep Western Boundary Current (DWBC), Northern Recirculation Gyre (NRG), and Subtropical Gyre (SG). Also shown are the approximate locations of Bermuda (BER), the New England Seamounts (NES), and the Sohm Abyssal Plain (SAP). The green line protruding from the continental shelf and slope south of New England is line W.

b. Radionuclide Data

The ^{230}Th and ^{231}Pa activity data considered in this study originate from both pre-GEOTRACES programs and the GA03 section (Table 1).

Table 1. Thorium-230 and Protactinium-231 Data Used in this Study

station	latitude	longitude	#[a] ^{230}Th$_d$	# ^{230}Th$_p$	# ^{231}Pa$_d$	# ^{231}Pa$_p$	error[b]	reference
CMME-13	32.76°N	70.78°W	8	8	11	0	1σ	Cochran et al. (1987)
S1	36.05°N	74.43°W	11	10	19	0	2σ	Guo et al. (1995)
EN407-3	39.47°N	68.37°W	11	0	0	0	2σ	Luo et al. (2010)
EN407-4	38.6°N	68.89°W	19	0	0	0	2σ	Luo et al. (2010)
EN407-6	39.73°N	69.75°W	19	0	0	0	2σ	R. François (pers. com.)
BATS	32°N	64°W	19	0	0	0	2σ	R. François (pers. com.)
OC278-2	37°N	69°W	11	0	0	0	2σ	R. François (pers. com.)
OC278-3	33°N	69°W	11	0	0	0	2σ	R. François (pers. com.)
OC278-4	36°N	68°W	10	0	0	0	2σ	R. François (pers. com.)
OC278-5	38°N	70°W	11	0	0	0	2σ	R. François (pers. com.)
GT11-01	39.69°N	69.81°W	25	10	25	10	1σ	Hayes et al. (2015a)
GT11-02	39.35°N	69.54°W	17	12	17	12	1σ	Hayes et al. (2015a)
GT11-03	38.67°N	69.10°W	20	12	20	12	1σ	Hayes et al. (2015a)
GT11-04	38.09°N	68.70°W	16	12	16	12	1σ	Hayes et al. (2015a)
GT11-06	37.61°N	68.39°W	20	12	21	12	1σ	Hayes et al. (2015a)
GT11-08	35.42°N	66.52°W	17	12	17	12	1σ	Hayes et al. (2015a)
GT11-10	31.75°N	64.17°W	28	12	28	11	1σ	Hayes et al. (2015a)
GT11-12	29.70°N	56.82°W	18	12	18	12	1σ	Hayes et al. (2015a)
GT11-14	27.58°N	49.63°W	21	12	21	11	1σ	Hayes et al. (2015a)

[a] number of observations. [b] σ is the standard error for data from R. François (pers. com.) and the standard deviation for all other data.

Radionuclide data in both dissolved and particulate forms are used and displayed in Appendix D (Fig. A1–A7).

1) Thorium-230

Measurements of ^{230}Th$_d$ from pre-GEOTRACES cruises generally show an increase with depth in the upper 2500–3000 m of the water column (Fig. A1). Below 2500–3000 m, stations sampled during these cruises feature either uniform ^{230}Th$_d$ or a ^{230}Th$_d$ decrease with depth. To our knowledge, prior to GEOTRACES, only two studies reported ^{230}Th$_p$ measurements in the investigated region (Fig. A1). Cochran et al. (1987) published ^{230}Th$_p$ data for a station in the Hatteras Abyssal Plain, and Guo et al. (1995) reported ^{230}Th$_p$ measurements from a station off Cape Hatteras in the Middle Atlantic Bight. The ^{230}Th$_p$ activities measured at both stations generally increase with depth.

The ^{230}Th$_{d,p}$ data collected along GA03 and used in this study have been described by Hayes et al. (2015a), so only a brief overview is provided below. Broadly, ^{230}Th$_d$ increased with depth in the upper part of the water column at all stations (Fig. A2). At the deepest stations, the ^{230}Th$_d$ data show a continued increase with depth down to 3000–4000 m, where vertical gradients of ^{230}Th$_d$ change sign. These inversions are particularly noticeable at stations GT11-04 to GT11-10. At station GT11-12 (east of Bermuda), ^{230}Th$_d$ below $\sim$ 4000 m tend to be more uniform compared to the activities measured at stations west of Bermuda. Similarly to ^{230}Th$_d$ data, ^{230}Th$_p$ data from GA03 generally show an increase with depth (Fig. A3). Stations GT11-06, GT11-10, and GT11-12 show indications of a reversal in the vertical ^{230}Th$_p$ gradient near 2000–3000 m, with measurements presenting a local maximum in the deepest sample(s), although ^{230}Th$_p$ data from GT11-10 and GT11-12 also display relatively large dispersion and (or) uncertainties. Particularly spectacular are the extremely large ^{230}Th$_p$ activities measured on four near-bottom samples at stations GT11-04 and GT11-08. The ^{230}Th$_p$ activities in these samples approach or exceed 1 dpm m^{-3}, which is larger by one to two orders of magnitude than ^{230}Th$_p$ activities measured at similar depths at other stations and larger than ^{230}Th$_d$ activities measured on the same or nearby samples at the same stations.

2) Protactinium-231

Only a few measurements of ^{231}Pa in the western North Atlantic existed prior to GEOTRACES (Fig. A4). Luo et al. (2010) reported ^{231}Pa$_d$ profiles at two locations at 38.5°N and 39.5°N near the western boundary, which generally show an increase with depth down to 2000–2500 m and a decrease with depth below. Similarly to ^{230}Th$_{d,p}$ data, the ^{231}Pa$_{d,p}$ data obtained along GA03 and used in this study have already been discussed (Hayes et al. 2015a). As for ^{230}Th$_d$ data, ^{231}Pa$_d$ data show an increase with depth in the upper part of the water column at all stations (Fig. A5). At the deepest stations, measurements of ^{231}Pa$_d$ present maxima between 2000–3000 m and a decrease with depth below. Measurements of ^{231}Pa$_p$ display an increase with depth down to 2000–3000 m and a decrease with depth below except for the deepest samples

(Fig. A6). As for $^{230}\mathrm{Th}_p$, stations GT11-04 and GT11-08 show extreme $^{231}\mathrm{Pa}_p$ values in near-bottom samples which largely exceed $^{231}\mathrm{Pa}_p$ and $^{231}\mathrm{Pa}_d$ measured on the same or nearby samples.

c. Optical Data

A relatively large number of optical measurements from nephelometers and beam transmissometers are available in the western North Atlantic (for a recent synthesis, see Gardner et al. (2017)). These instruments can be used to measure the distribution of, respectively, light attenuation and light scattering with vertical resolutions of approximately 2 m and 100-250 m, respectively (note that the range for the light scattering resolution reflects the dependence of the resolution on the rate at which the nephelometer is lowered in the water column;Gardner et al. (1985b)). From measurements of these optical properties, the vertical distribution of PM concentration (P, mg m^{-3}) can be estimated using empirical calibrations.

The following approach is applied to derive a field of PM concentration for use in the geochemical component of the model. First, the light scattering and light attenuation data compiled by Gardner et al. (2017, 2018b) are converted into P estimates using calibration formulae reported by Gardner et al. (2017) for light scattering and Gardner et al. (2018b) for light attenuation. In addition, the light attenuation data from GA03 and available from the GEOTRACES Intermediate Data Product (Schlitzer et al. 2018) are used and converted to P estimates following Gardner et al. (2018b). Second, the PM concentrations at locations where optical data are available are interpolated linearly at the model grid levels. The errors produced by vertical interpolation are expected to be generally small given the high vertical resolution of the optical profiles and are neglected in this work. Note that the model is based on terrain-following (s) coordinates, not depth coordinates (section 3), so that the levels at which P values are interpolated occur along s-surfaces, not depth surfaces. Finally, the interpolated P values are mapped along each s-surface using a minimum variance (Gauss-Markov) procedure in order to obtain an estimate of PM concentration at each model grid point along that surface (for details see Appendix A). Note that in this study the PM concentrations at model grid points are fixed and not allowed to be transported by advection or mixing.

3. Ocean Model

a. Domain

The model domain considered in this study is the western North Atlantic north of 28°N and west of 55°W (Fig. 3). It is bounded in the west by the 200-m isobath, which is taken as a closed boundary. The other two boundaries – the latitude of 28°N and the longitude of 55°W – are open. The model grid has a horizontal resolution of 1/4° and includes 31 vertical levels. It is determined by a trade-off between a desire to simulate the circulation with greatest detail possible and the large computational cost associated with the simulation of steady-state distributions of ^{230}Th and ^{231}Pa (section 4). The vertical levels of the model are s-coordinates defined from

$$s = \frac{z - \eta}{h + \eta}. \tag{1}$$

Here z is the local depth, η is the free surface elevation, and $h = h(x, y)$ is the water depth where x and y denote, respectively, the longitude and latitude coordinates in the domain. The model topography $h(x, y)$ is derived by averaging the bathymetric data from ETOPO2v2 (2006) in model grid cells.

b. *Physical Component*

The physical component of the model is the Princeton Ocean Model (POM) – a primitive-equation model based on s-coordinates and a free surface (Blumberg and Mellor 1987; Mellor 2002). The computer code applied in this study is `pom2k.f`. Note that in the present application, the variation of the Coriolis parameter with latitude is taken into account according to $f = f_o + \beta(y - y_o)$, where $f_o = 2\Omega \sin\phi_o$, $\beta = (2\Omega/r)\cos\phi_o$, $\Omega = 7.29 \times 10^{-5}$ s^{-1} is Earth angular velocity, $r = 6371$ km is the Earth radius, $\phi_o = 36.375$°N, and y_o is the value of y corresponding to the latitude ϕ_o. The basic equations of POM are the governing equations for the zonal velocity component (u) and the meridional velocity component (v), the hydrostatic approximation, the governing equations for (potential) temperature (T) and salinity (S), and the condition of incompressibility. These equations are complemented with a nonlinear equation of state (Mellor 1991).

c. *Geochemical Component*

The geochemical component of the model includes governing equations for ^{230}Th and ^{231}Pa in both the dissolved phase and the particulate phase. The dissolved and particulate activities in the model are intended to represent the dissolved and particulate activities as measured on water samples and defined operationally by filtration. The basic equations of the geochemical component are

$$\frac{\partial A_d}{\partial t} + \mathbf{u} \cdot \nabla A_d = \lambda A_\pi + k_{-1} A_p - k_1 A_d + \frac{\partial}{\partial z}\left(\kappa_{\mathcal{T}} \frac{\partial A_d}{\partial z}\right) + F_d, \tag{2a}$$

$$\frac{\partial A_p}{\partial t} + \mathbf{u} \cdot \nabla A_p + w_p \frac{\partial A_p}{\partial z} = k_1 A_d - k_{-1} A_p + \frac{\partial}{\partial z}\left(\kappa_{\mathcal{T}} \frac{\partial A_p}{\partial z}\right) + F_p. \tag{2b}$$

Here A_d (A_p) is the activity of ^{230}Th or ^{231}Pa in dissolved (particulate) form expressed in dpm m^{-3}, $\mathbf{u}$ is the fluid velocity, w_p is the particle settling speed, λ is the radioactive decay constant for ^{230}Th or ^{231}Pa, A_π is the activity of the radioactive parent (^{234}U for ^{230}Th and ^{235}U for ^{231}Pa), k_1 (k_{-1}) is a first-order apparent rate constant for Th or Pa adsorption onto particles (Th or Pa desorption from particles), $\kappa_\mathcal{T}$ is a vertical turbulent diffusivity, and the terms (F_d, F_p) denote the effects of horizontal mixing. Clearly, t is time and $\nabla = \hat{x}(\partial/\partial x) + \hat{y}(\partial/\partial y) + \hat{z}(\partial/\partial z)$ is the gradient operator where $(\hat{x}, \hat{y}, \hat{z})$ are unit vectors. Vertical and horizontal mixing processes are represented as for temperature and salinity: the diffusivity $\kappa_\mathcal{T}$ is obtained from a turbulent closure scheme (Mellor and Yamada 1982) which involves the solution of governing equations for turbulent kinetic energy $(q^2/2)$ and for $q^2 l$, where l is a turbulence length scale, and the terms (F_d, F_p) are parameterized according to Smagorinsky (1963).

Note that the radioactive decay terms are omitted in (2a-2b). The half-lives of ^{230}Th and ^{231}Pa exceed by several orders of magnitude the time scales of solid-solution equilibration of Th and Pa in laboratory experiments (e.g., Nyffeler et al. (1984); Geibert and Usbeck (2004)). Likewise, the value of $\lambda = 9.17 \times 10^{-6}$ yr^{-1} for ^{230}Th is very small compared to observational estimates of k_1 and k_{-1} of $\geq$ O(10^{-1} yr $^{-1}$) for Th in oceanic waters (for a compilation see Marchal and Lam (2012); Lerner et al. (2017)).

The influence of particle concentration on particle scavenging is accounted for in the model as follows. Both theoretical considerations (e.g., Honeyman et al. (1988)) and empirical evidence (e.g., Lerner et al. (2017)) suggest that the apparent rate constant for metal adsorption onto particles, k_1, increases with the (bulk) concentration of particles. In our model, k_1 is set to vary with particle concentration according to

$$k_1(x, y, z) = k_{1,b} + k_1' P(x, y, z). \tag{3}$$

Here $P(x, y, z)$ is the particle concentration estimated from the optical measurements (Appendix A), k_1' describes the variation of the adsorption rate constant with particle concentration, and $k_{1,b}$ is a background value intended to account for the effect of particles that are not detected by the optical instruments (for a discussion of instrumental sensitivities, see, e.g., McCave (1986) and Boss et al. (2009)).

Three comments are in order regarding the geochemical component of the model. First, in a more general treatment, k_1 would be a function of P^b where the exponent b could be different from one. From a compilation of k_1 estimates reported in the literature, Honeyman et al. (1988) showed that k_1 appears to be proportional to P^b with $b = 0.51$ (their Table 2). These authors argued that such a variation of the adsorption rate constant with particle concentration could explain the particle concentration effect. In contrast, in their analysis of Th isotope and particle data collected east of Bermuda along GA03, Lerner et al. (2017) estimated that b ranges from 0.95 to 1.62 (their Table 4), depending on the technique used to regress $\ln k_1$ against $\ln P$ and on the application of a smoothing condition on the vertical distribution of the rate parameters. Consistent with the latter result, a value of $b = 1$ is assumed in this study.

Second, in contrast to k_1, the desorption rate constant (k_{-1}) and the particle settling speed (w_p) are assumed to be independent of particle concentration or any other particle (or water) property. The k_{-1}

values estimated from Th isotope and particle data at GA03 stations east of Bermuda (Lerner et al. 2017) do not exhibit a consistent vertical trend, except at four stations where k_{-1} appears to decrease with depth. Near-surface values of k_{-1} estimated at these stations are also high relative to the other stations. The w_p values estimated by Lerner et al. (2017) tend to be larger and display enhanced vertical variability below 2000 m, except at the TAG hydrothermal vent of the MAR, where their w_p estimates are low relative to the other stations. In the present study, k_{-1} and w_p are taken as uniform throughout the model domain for simplicity.

Finally, the rate parameters $(k_{1,b}, k_1', k_{-1})$ are allowed to be different for ^{230}Th and ^{231}Pa in the model in order to account for the differences in the sorption kinetics of Th and Pa in oceanic waters (e.g., Moran et al. (2002); Hayes et al. (2015a)). The particle settling speed, w_p, is also allowed to be different for the two nuclides, a treatment suggested by the fact that (i) Th and Pa may be carried by different particulate phases in the ocean (e.g., Chase et al. (2002); Geibert and Usbeck (2004); Roberts et al. (2009); Chuang et al. (2013)), and (ii) different particles types may have different sinking speeds (e.g., biogenic silica, lithogenic material, and calcium carbonte may sink much more rapdily than particulate organic carbon (Armstrong et al. 2001; Klaas and Archer 2002)). The value of w_p for ^{230}Th is determined by fitting (using ordinary least-squares) the equation $^{230}\mathrm{Th}_p(\mathrm{z}) = {}^{230}\mathrm{Th}_p(0) + \lambda^{234}_{\text{Th-230}}\mathrm{U}z/w_p$ to a composite profile compiled from all $^{230}\mathrm{Th}_p$ data in the upper 3000 m for stations GT11-01 to GT11-12 (not shown). This popular approach to constrain w_p(Th) from $^{230}\mathrm{Th}_p$ data (e.g., Bacon and Anderson (1982); Krishnaswami et al. (1976, 1981); Rutgers van der Loeff and Berger (1993); Scholten et al. (1995); Venchiarutti et al. (2008)) yields an estimate of w_p(Th) of 1800 m yr^{-1}, the value used in our simulations. In contrast, the value of w_p for ^{231}Pa, which is generally less sensitive to particles and thus more strongly influenced by circulation than ^{230}Th, is determined by a trial-and-error approach until good agreement with $^{231}\mathrm{Pa}_{d,p}$ data is achieved. Thus, the value of w_p for $^{230}\mathrm{Th}_p$ is determined by disregarding the effects of advection and mixing, whereas the value of w_p for $^{231}\mathrm{Pa}_p$ is determined by taking such effects into account.

A trial-and-error approach is also used to determine the value of the other geochemical parameters with two exceptions: $k_{1,b}$ for Th is fixed to 0.4 yr^{-1}, a value consistent with k_1 estimates for GA03 stations east of Bermuda in waters with low particle concentration (Lerner et al. 2017), and $k_{1,b}$ for Pa is fixed to a lower value, 0.04 yr^{-1}, consistent with the different particle sensitivities of Pa and Th in seawater (e.g., Moran et al. (2002); Hayes et al. (2015a)). Values for each parameter in the geochemical component of the model are listed in Table 3.

d. Boundary Conditions

The conditions imposed at the horizontal and lateral boundaries of the model domain are summarized below (for details see appendices B-C). Consider first the horizontal boundaries. At the sea surface, the model is forced with an annual mean wind field derived from satellite scatterometry (Risien and Chelton 2008), and the simulated values of temperature and salinity in the surface layer are restored to annual mean fields from the World Ocean Atlas (Locarnini et al. 2013; Zweng et al. 2013) (section 2a). The restoring approach implies that the surface (T, S) fields simulated by the model will not depart too markedly from the climatologic fields – a desirable result – with the caveat that the modeled variability due to eddy activity will be muted to some degree. At the bottom, a shear stress condition is applied and a condition of no flux is specified for $^{230}\text{Th}_{d,p}$ and $^{231}\text{Pa}_{d,p}$.

Consider then the lateral boundaries. The western boundary (aligned with the 200-m isobath) is a closed boundary. This treatment implies that the model simulations presented in this paper will not represent the exchanges of momentum, energy, and material between the continental shelf and the continental slope (e.g., Garvine et al. (1988); Lozier and Gawarkiewicz (2001); Gawarkiewicz et al. (2004); Churchill and Gawarkiewicz (2009)). At the other two lateral boundaries (along 28°N and along 55°W), radiation conditions are specified in order to minimize the reflection of perturbations generated within the domain. Along specific segments of these boundaries, inflows and outflows representing the Gulf Stream, the DWBC, and Sargasso Sea water entering or exiting the domain are also applied, following previous regional model studies of the western North Atlantic (e.g., Thompson and Schmitz (1984); Ezer (2016a,b)). Note that, at the DWBC inflow, the boundary values of ^{230}Th and ^{231}Pa are based on measurements in deep waters in the Labrador Sea, except for $^{231}\text{Pa}_d$ whose value exceeds these measurements, which we found produced a reference solution that more closely agreed with the available radionuclide measurements. At all other locations along the open boundaries, ^{230}Th and ^{231}Pa values are based on measurements at station GT11-14, which is situated to the east of the model domain (Appendix C).

e. Method of Solution

The differential equations of the model are solved as follows (for details see Blumberg and Mellor (1987); Mellor (2002)). First, the differential equations are expressed in terrain-following (s) coordinates. The particle settling speed w_p, which appears in equation (2b), is converted into an equivalent speed in s-coordinates using the relationship,

$$\omega_p = w_p \cos\theta, \tag{4}$$

where θ is the angle between the vertical axis and the normal to the s-surface. Here $\cos\theta$ is approximated from

$$\cos\theta = \frac{1}{\sqrt{(\partial z/\partial x)_s^2 + (\partial z/\partial y)_s^2 + 1}}, \tag{5}$$

where the partial derivatives are evaluated using central differences. Second, the dynamical equations of POM are separated into equations for slow motions (internal mode) and fast motions (external mode). This 'mode splitting' technique allows the calculation of the free surface elevation at relatively small computational cost. Finally, the differential equations represented in s-coordinates are solved using finite differences on a staggered C grid. The advection terms in the governing equations for $(T, S, A_d, A_p, q^2/2, q^2 l)$ are solved using a central difference scheme, and these equations are integrated forward in time using a leap frog scheme with an Asselin filter. The equations for the external mode are integrated with a time step of 15 s and the equations for the internal mode, including the activity equations (2a–2b), are integrated with a time step of 450 s. Unless stipulated otherwise, the model parameters take the values listed in Tables 2–3.

Table 2. Parameters of the physical model component

Physical Parameters

		value	units
ρ_o	reference density	1025	kg m^{-3}
g	acceleration due to gravity	9.806	m s^{-2}
C	Smagorinsky coefficient	0.2	1
κ	von Kármán constant	0.4	1
$\kappa_{u,o}$	background vertical viscosity	0	m^2 s^{-1}
$\kappa_{T,o}$	background vertical diffusivity	0	m^2 s^{-1}
P_r	turbulent Prandtl number	5	1
z_r	bottom roughness parameter	0.01	m
τ	restoring time scale for SST and SSS	14.4	d

Numerical Parameters

		value	units
Δt_E	time step for external mode	15	s
Δt_I	time step for internal mode	450	s
Δs	step interval for advective terms[a]	5	1
$h_{\max}$	maximum depth in radiation condition	200	m
$u_{\max}$	maximum velocity for CFL violation	100	m s^{-1}
c	constant of Asselin filter	0.1	1
α	weight for sea surface slope term[b]	0	1

[a] Step interval during which the advective terms of the external mode are not updated

[b] Weight used in the external mode equations

Table 3. Parameters of the geochemical model component

		value	units
$\lambda_{\text{Th-230}}$	radioactive decay constant of ^{230}Th	9.17×10^{-6}	yr^{-1}
$\lambda_{\text{Pa-231}}$	radioactive decay constant of ^{231}Pa	2.12×10^{-5}	yr^{-1}
^{234}U	activity of ^{234}U	2750	dpm m^{-3}
^{235}U	activity of ^{235}U	108	dpm m^{-3}
$k_1(\text{Th})$	adsorption rate constant for Th	variable	yr^{-1}
$k_1(\text{Pa})$	adsorption rate constant for Pa	variable	yr^{-1}
$k_{1,b}(\text{Th})$	background value of $k_1(\text{Th})$	0.4	yr^{-1}
$k_{1,b}(\text{Pa})$	background value of $k_1(\text{Pa})$	0.04	yr^{-1}
$k_1'(\text{Th})$	sensitivity of $k_1(\text{Th})$ to particle concentration	0.04	yr^{-1} mg^{-1} m^3
$k_1'(\text{Pa})$	sensitivity of $k_1(\text{Pa})$ to particle concentration	0.02	yr^{-1} mg^{-1} m^3
$k_{-1}(\text{Th})$	desorption rate constant for Th	3.69	yr^{-1}
$k_{-1}(\text{Pa})$	desorption rate constant for Pa	18.45	yr^{-1}
$w_p(\text{Th})$	settling speed of $^{230}\text{Th}_p$	1800	m yr^{-1}
$w_p(\text{Pa})$	settling speed of $^{231}\text{Pa}_p$	2400	m yr^{-1}

4. Reference Solution

A large number of experiments have been conducted with the model in an effort to reproduce the circulation and the radionuclide distributions observed in the western North Atlantic. In this section, we describe a particular model solution, obtained with parameter values listed in Tables 2–3, which shows relatively good agreement with the observations. This solution is called the 'reference' solution below. The word 'reference' is meant to imply that this solution is used as a pivot against which results from other simulations are compared, not that it is the most accurate simulation that could be obtained from the model.

The model is integrated forward in time until the circulation and the radionuclide distributions reach quasi-steady states. The initial conditions of the model are the following: (i) the ocean is at rest ($\mathbf{u} = 0$, $q^2 = 0$, and $q^2 l = 0$) with a flat surface ($\eta = 0$), (ii) the (T, S) distributions are set to the annual mean distributions from the World Ocean Atlas (Locarnini et al. 2013; Zweng et al. 2013), and (iii) the $^{230}\text{Th}_{d,p}$

and $^{231}\mathrm{Pa}_{d,p}$ distributions are specified from idealized vertical profiles which broadly reproduce data from station GT11-14 (located east of the domain along GA03) and which are also used as lateral boundary conditions (Appendix C; Fig. A7). The model is first integrated diagnostically for a period of 10 days, with $(T, S, {}^{230}\mathrm{Th}_{d,p}, {}^{231}\mathrm{Pa}_{d,p})$ fixed to their initial values, and then prognostically for a period of 2545 days ($\sim$ 7 yr), with $(T, S, {}^{230}\mathrm{Th}_{d,p}, {}^{231}\mathrm{Pa}_{d,p})$ allowed to vary according to their respective governing equations. At this time, the domain averages of kinetic energy $\rho_o|\mathbf{u}^2|/2$, $^{230}\mathrm{Th}_{d,p}$, and $^{231}\mathrm{Pa}_{d,p}$ have reached quasi-steady values (Fig. 4).

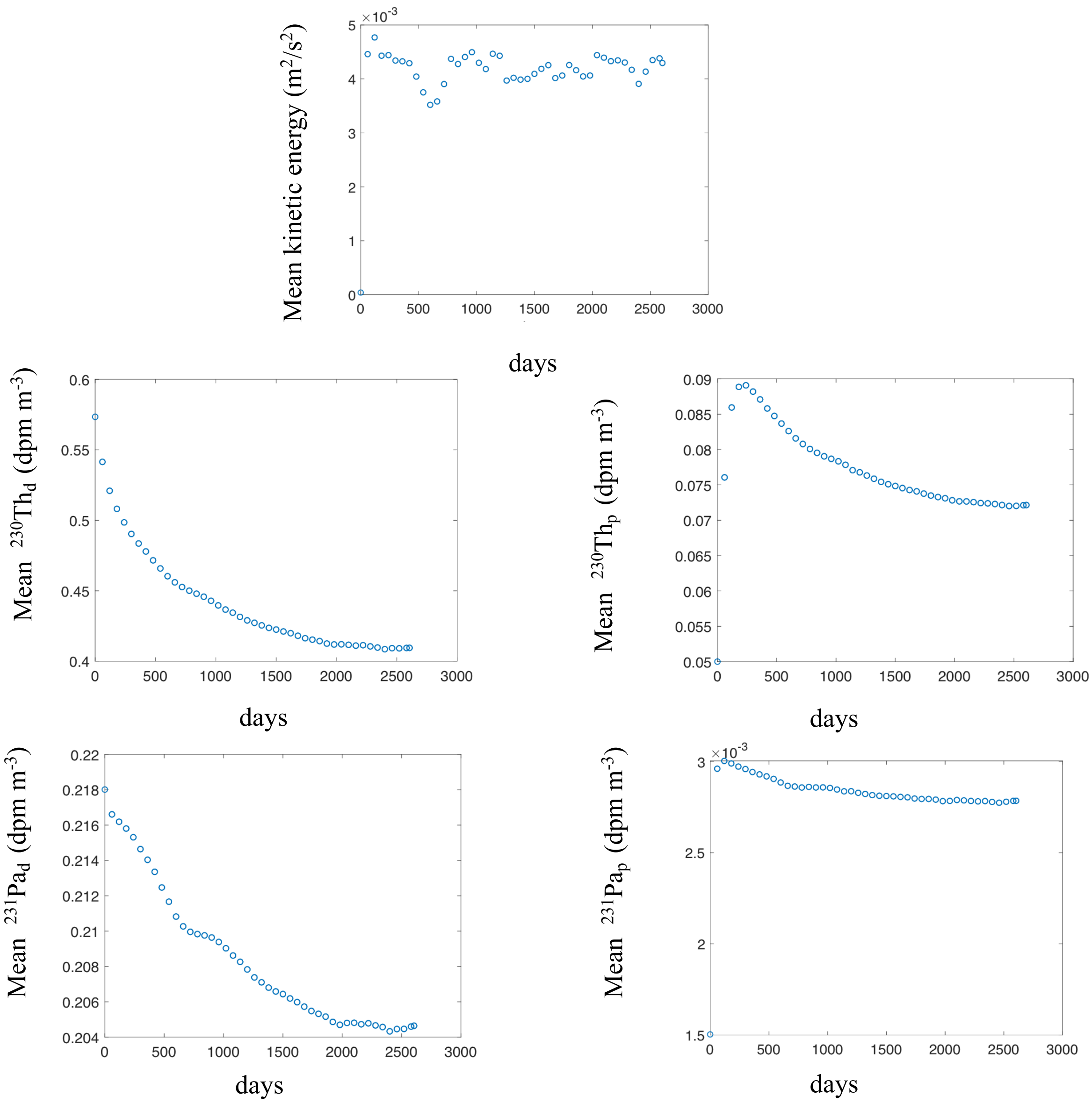

Fig. 4. Time series of the domain-averaged kinetic energy, $^{230}\mathrm{Th}_d$, $^{230}\mathrm{Th}_p$, $^{231}\mathrm{Pa}_d$, and $^{231}\mathrm{Pa}_p$ in the reference solution

Notice that the integration time needed to attain quasi-steady state is longer for ^{230}Th and ^{231}Pa ($\sim$ 6 yr) than it is for the mean kinetic energy ($\sim$ 1 yr). Hence the model results reported in this paper are averages for the last 2190 days (6 yr) of the integration for sea surface elevation and velocities, and for the last 365 d (1 yr) of the integration for $^{230}\mathrm{Th}_{d,p}$ and $^{231}\mathrm{Pa}_{d,p}$.

a. Circulation

1) Sea Surface Elevation

The distribution of the sea surface elevation simulated by the model is compared to the distribution of the multi-year annual mean SSH derived from satellite altimetry (Fig. 5).

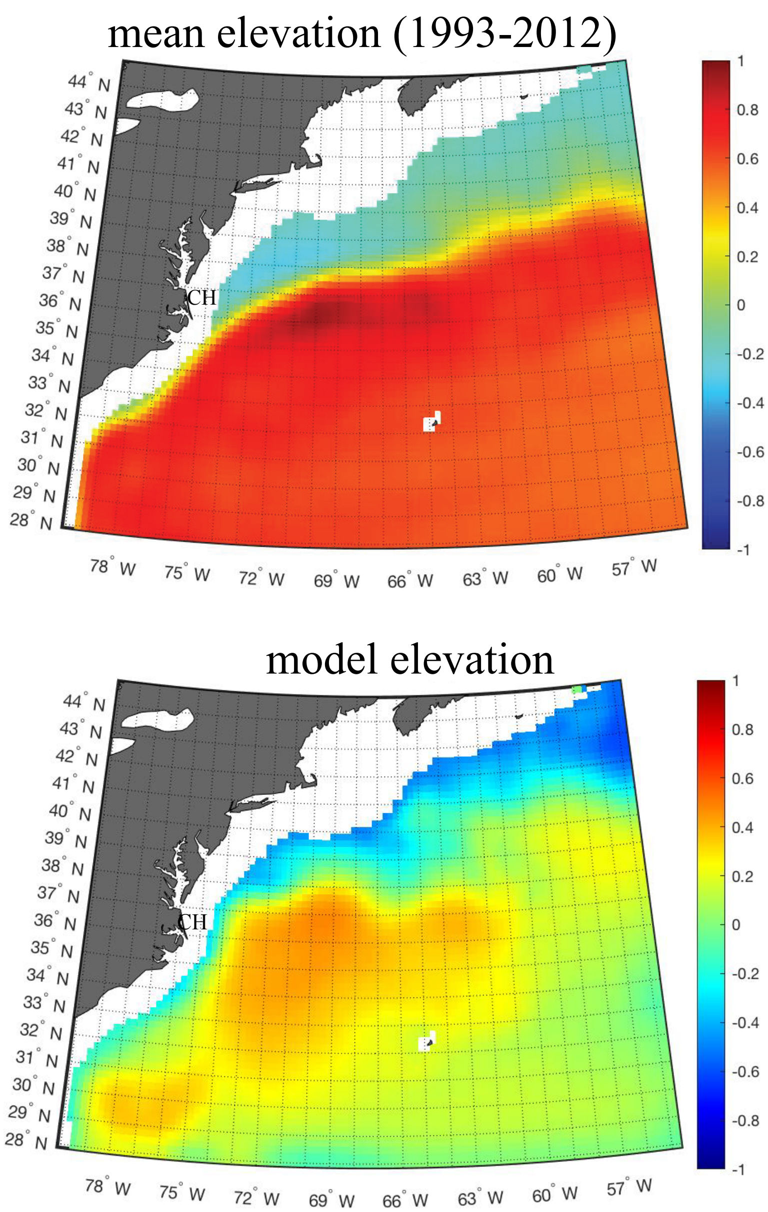

Fig. 5. Averages of sea surface height (m) as observed from satellite altimeter data during the period 1993-2012 (top) and as simulated in the reference solution (bottom). The average pathway of the Gulf Stream coincides with the yellow band (upper panel) and "CH" stands for Cape Hatteras.

The SSH distribution from satellite altimeters reveals the average pathway of the Gulf Stream during the observation period (1993–2012). Maxima in SSH occur just south of the Gulf Stream, downstream of the region where this separates from the margin near Cape Hatteras, and minima in SSH occur in the region between the Gulf Stream and the continental slope east of Cape Hatteras. The northward depression in SSH across the Gulf Stream is of the order of 1 m and occurs on an horizontal scale of O(100 km). The pattern of sea surface elevation simulated by the model is broadly consistent with the observed pattern, although the magnitude of the SSHs and the gradients of SSH across the Gulf Stream as observed by altimeters are generally underestimated by the model. The relatively small SSH gradients in the simulation implies that the strength of the Gulf Stream as predicted by the model may be lower than observed, an inference consistent with a comparison with velocity data along line W (see next section).

The standard deviations of SSH values derived by satellite altimetry are compared with the standard deviations of sea surface elevation calculated by the model (Fig. 6).

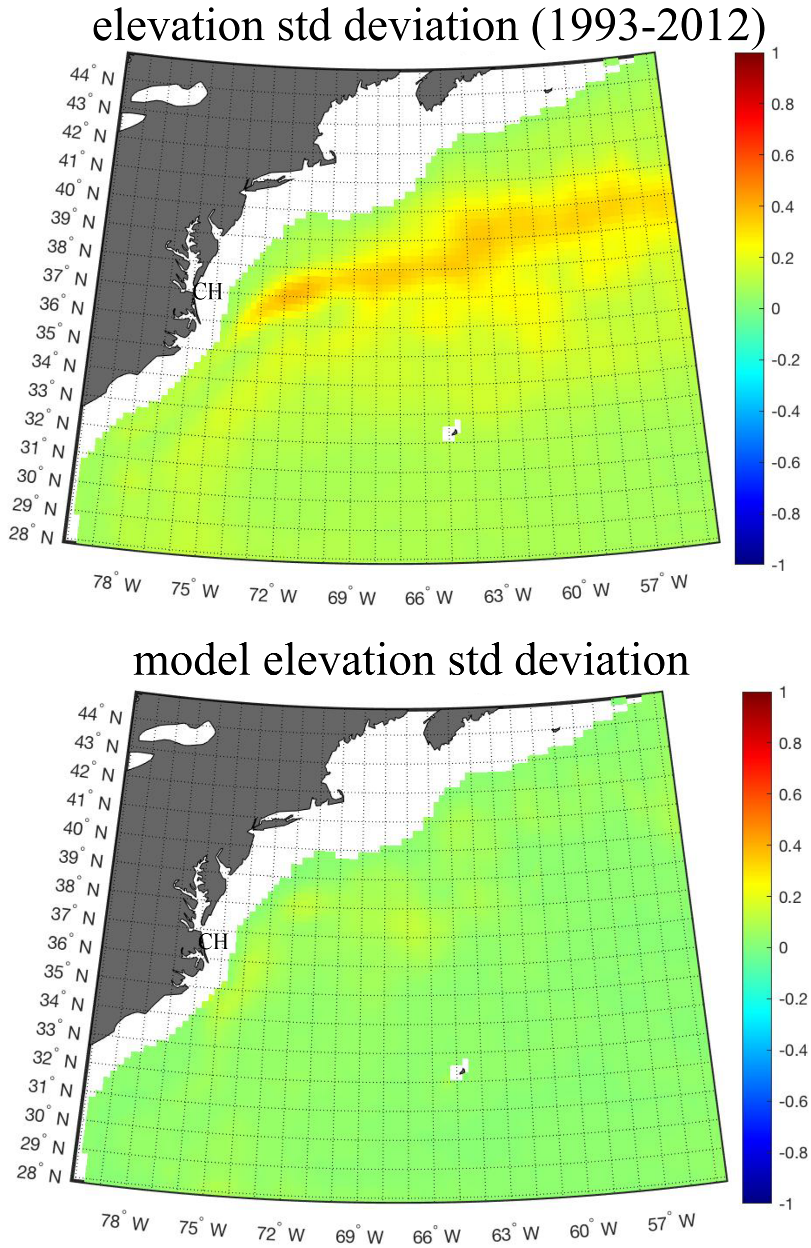

Fig. 6. Standard deviation of sea surface height (m) as observed from satellite altimeter data during the period 1993-2012 (top) and as simulated in the reference solution (bottom). The average pathway of the Gulf Stream coincides with the yellow band (upper panel) and "CH" stands for Cape Hatteras.

As expected, the standard deviations observed by altimeters show the largest values along the average pathway of the Gulf Stream, which reflects the meandering and eddy activity of the Gulf Stream. Maxima in standard deviations are also predicted in the vicinity of the Gulf Stream by the model, although the standard deviations from the model are in general strongly underestimated compared to those observed. Eddy variability is thus underpredicted by the model. Model-data differences in SSH (mean and standard deviation) could be ascribed to various factors, such as insufficient spatial resolution of the model, the restoring of surface (T, S) to climatologic fields, and the fact that model averages (6 yr) and data averages (20 yrs) are not calculated over the same time span.

2) Horizontal Velocity

The horizontal velocities simulated by the model in the surface layer and at a depth of 3500 m are displayed in Figure 7.

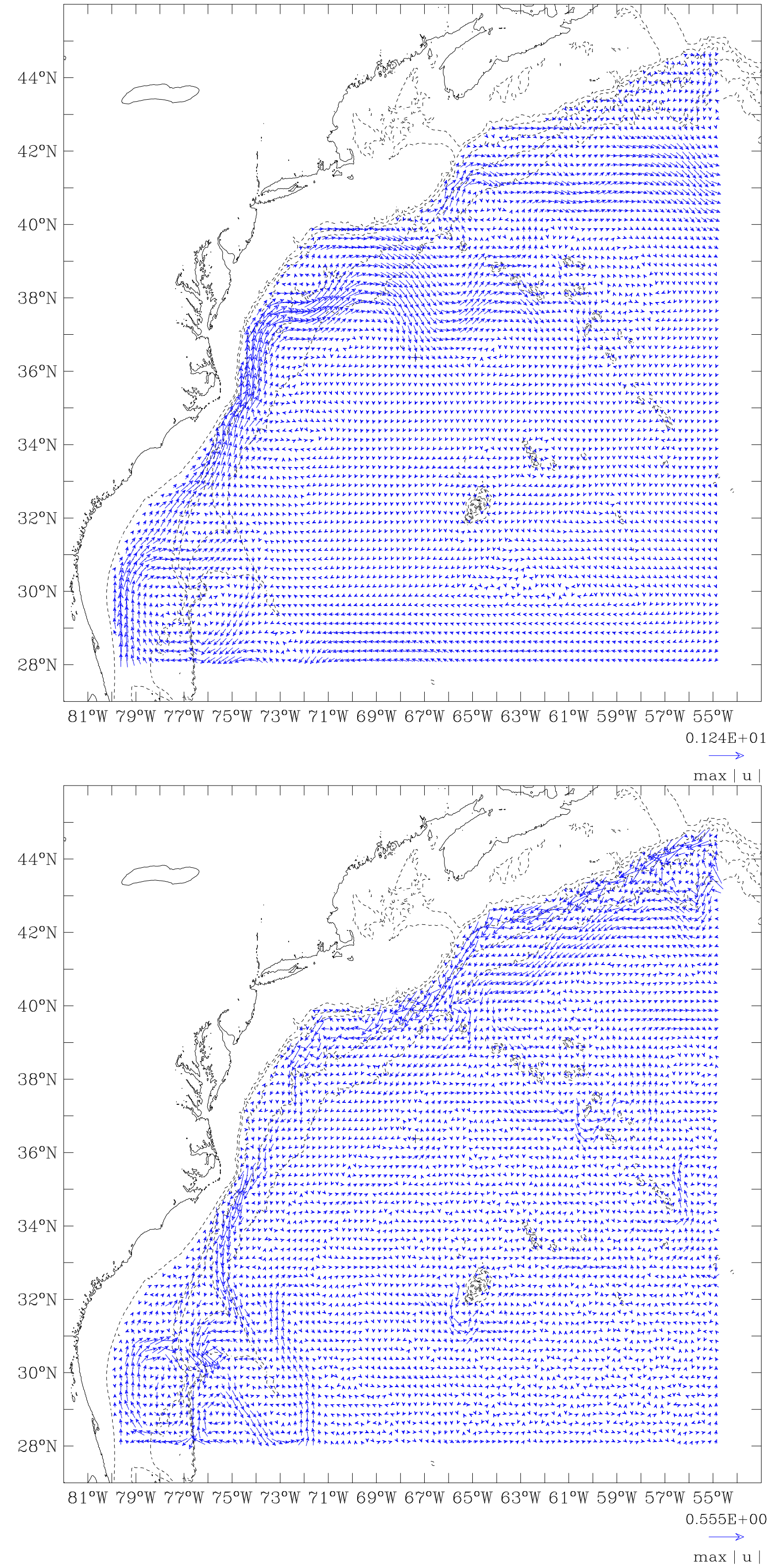

Fig. 7. Field of horizontal velocity in the surface layer (top) and at a depth of 3500 m (bottom) simulated in the reference solution. The horizontal arrow at the lower right outside each panel is the maximum speed

in units of m s^{-1} in the corresponding field.

In the surface layer, the model simulates a strong current – the Gulf Stream – which flows northward along the margin. The simulated current detaches from the margin north of Cape Hatteras, i.e., too far to the north compared to the observations (Fig. 5), and then flows to the northeast as a meandering structure. Inaccurate Gulf Stream separation has been a long-standing problem with many models, although simulations generally improve when high resolution is used (e.g., Ezer (2016b); and references therein). The largest speeds in the modeled Gulf Stream reach O(1 m s^{-1}), which is consistent with observations from extensive field programs (e.g., Meinen and Luther (2016)). At a depth of 3500 m, the model predicts a relatively strong current flowing to the southwest along the boundary – the Deep Western Boundary Current. The modeled DWBC presents distinct cores at some locations but remains generally noticeable all along the western boundary.

The simulated horizontal velocities between the New England continental shelf and Bermuda are compared to the velocities observed during the line W program (Fig. 8).

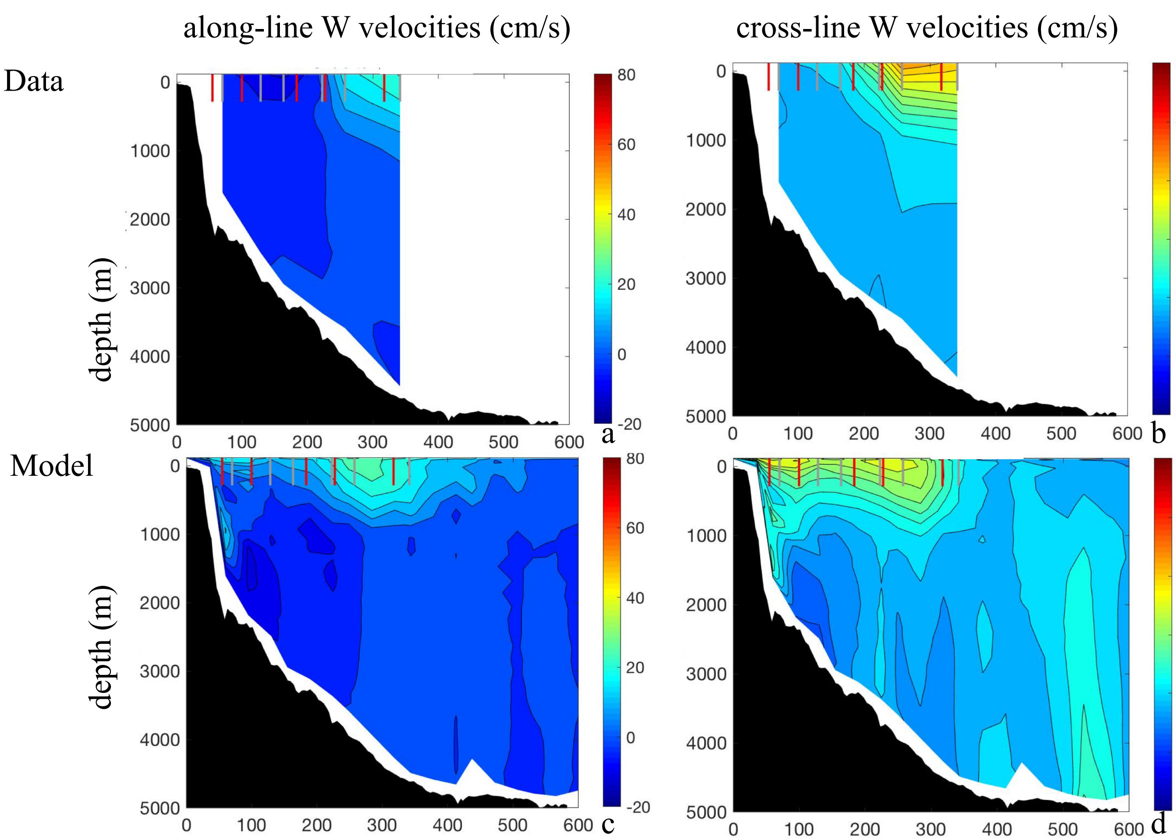

Fig. 8. Distribution of horizontal velocity components between the New England continental shelf and Bermuda as measured during the line W program (top) and as simulated in the reference solution (bottom). At the top of each panel, red vertical lines show the position of GA03 stations GT11-01 to GT11-06, and grey vertical lines show the position of mooring locations. Coordinates along the horizontal

axis are distances from 40.125°N,70.125°W (line W data from Toole et al. (2017)).

The observed velocity components both parallel and perpendicular to line W show the largest magnitudes in the vicinity of the Gulf Stream, i.e., at a distance of $\geq$ 200 km from the shelf break. The Gulf Stream is the most conspicuous feature along the section, showing flow to the northeast with velocity maxima in the upper $\sim$ 1000 m. Below the Gulf Stream and along the continental rise is the Deep Western Boundary Current, which flows to the southwest and is characterized by much lower vertical shears and speeds compared to the Gulf Stream. In accordance with these observations, the model simulates strong currents in the upper $\sim$ 1000 m and along the western boundary. Whereas the simulated speeds in the Gulf Stream and DWBC have the observed orders of magnitude, the horizontal velocities in the Gulf Stream (DWBC) are underestimated (overestimated) by the model compared to the observations. Moreover, both currents in the model simulation occur north of their respective observed locations. Again, model errors such as due to too coarse spatial resolution and surface thermodynamical forcing may contribute to the differences between the simulation and the observations.

b. Radionuclide Activities

We compare in this section the distributions of $^{230}\mathrm{Th}_{d,p}$ and $^{231}\mathrm{Pa}_{d,p}$ calculated in the reference solution to those observed from pre-GEOTRACES campaigns and along the western segment of GA03. Model results are compared with both (i) station-averaged profiles of $^{230}\mathrm{Th}_{d,p}$ and $^{231}\mathrm{Pa}_{d,p}$ computed by linearly interpolating all radionuclide data at the same vertical levels and averaging the interpolated data along each vertical level, and (ii) measured radionuclide profiles at individual stations. The rationale for considering both (i) and (ii) is that a model driven by climatologic forcing may better reproduce station-averaged profiles than profiles measured at specific locations and specific times. Notice that in the comparison between measured and simulated radionuclide activities, the extreme $^{230}\mathrm{Th}_p$ and $^{231}\mathrm{Pa}_p$ values measured on two samples at stations GT11-04 and GT11-08 (Figs. A3 and A6) are excluded.

The station-averaged profiles of $^{230}\mathrm{Th}_d$ and $^{231}\mathrm{Pa}_d$ display a reversal in activity gradients at mid-depth (Figs. 9 and 10), as expected from the inspection of the profiles measured at the individual stations (Figs. A1-A2 and Figs. A4-A5). Note also the relatively high $^{230}\mathrm{Th}_d$ and $^{231}\mathrm{Pa}_d$ averages at the three deepest levels, below 4500 m. These averages are based on data from a relatively small number of stations and are strongly influenced by data from station GT11-12, situated at > 500 km to the southeast of Bermuda (Fig. 3). Notably, the $^{230}\mathrm{Th}_d$ activities measured below $\sim$ 4500 m at station GT11-12 exceed 0.8 dpm m^{-3}, which is larger by a least a factor of two than the $^{230}\mathrm{Th}_d$ activities measured below $\sim$ 4500 m at the other deep stations of GA03 (Fig. A2). The deepest value of $^{230}\mathrm{Th}_d$ shown in figure 9 comes from station GT11-12 only, whilst the two values directly above are averages of data from GT11-12 as well as a few other stations. As a result, the deepest value $^{230}\mathrm{Th}_d$ is high, and the other two values are also relatively high and characterized by large standard errors (Fig. 9). Speculatively, the much higher $^{230}\mathrm{Th}_d$ and $^{231}\mathrm{Pa}_d$ activities measured near the bottom at GT11-12 compared to other stations of GA03 stem from the much weaker BNL at GT11-12, as revealed by the sections of the beam attenuation coefficient for particles (Fig. 3 of Hayes et al. (2015a)) and of the bulk particle concentration (Fig. 5 of Lam et al. (2015)).

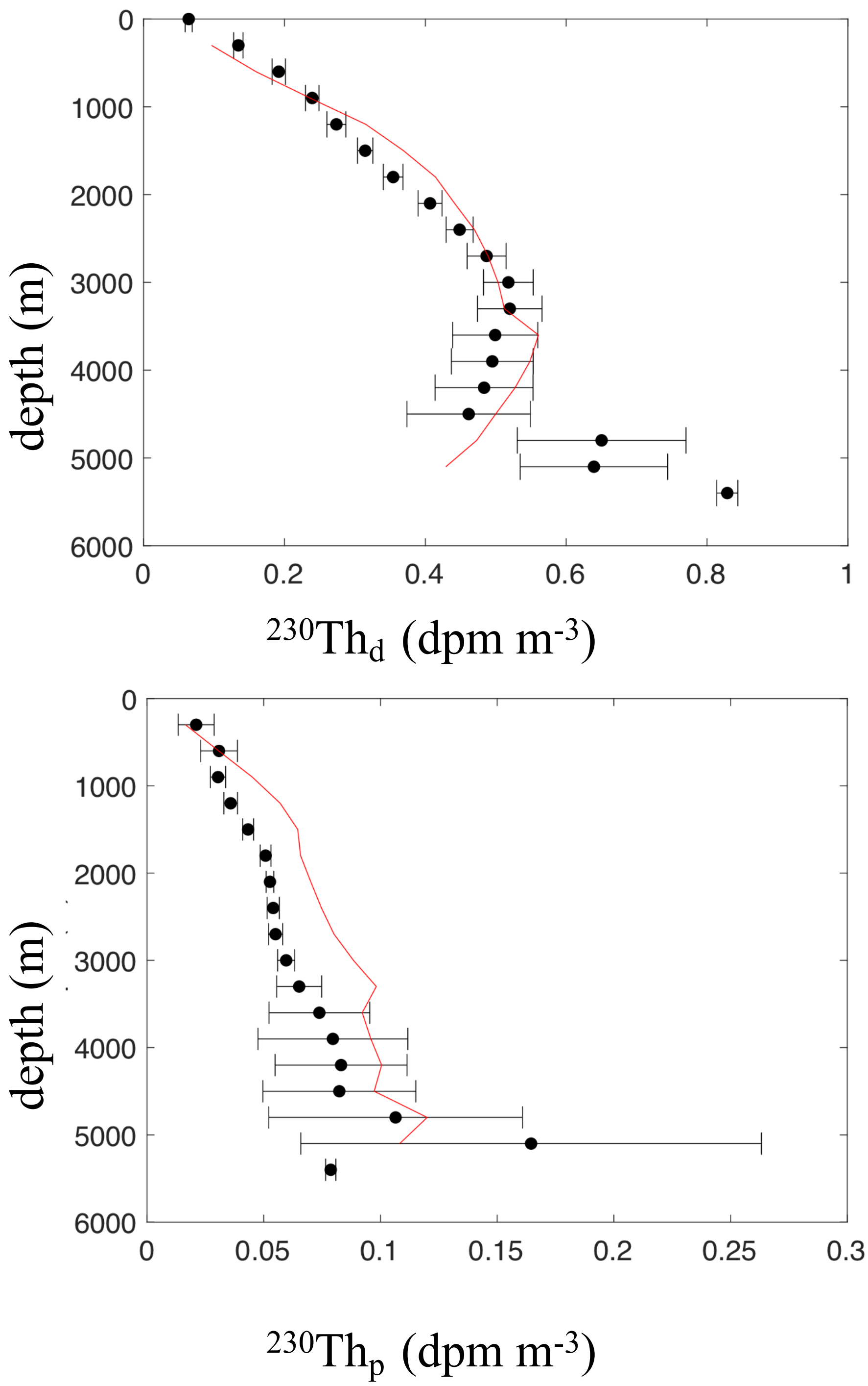

Fig. 9. Profile of station-averaged ^{230}Th$_d$ (top) and ^{230}Th$_p$ (bottom) as calculated from pre-GEOTRACES and GA03 measurements (black circles) and as simulated in the reference solution (red line). The circles show averages of measurements from several stations with the following exceptions: for ^{230}Th$_d$ the shallowest circle is a measurement from a single station (OC278-5), and for ^{230}Th$_{d,p}$ the deepest circle is a measurement from a single station (GT11-12). The horizontal bars show the standard errors of the

averages (measurement error for the shallowest $^{230}\mathrm{Th}_d$ measurement and the deepest $^{230}\mathrm{Th}_{d,p}$ measurements; Table 1). The extreme values of $^{230}\mathrm{Th}_p$ near the bottom of stations GT11-04 and GT11-08 are excluded from the station-averaged profile of the measurements.

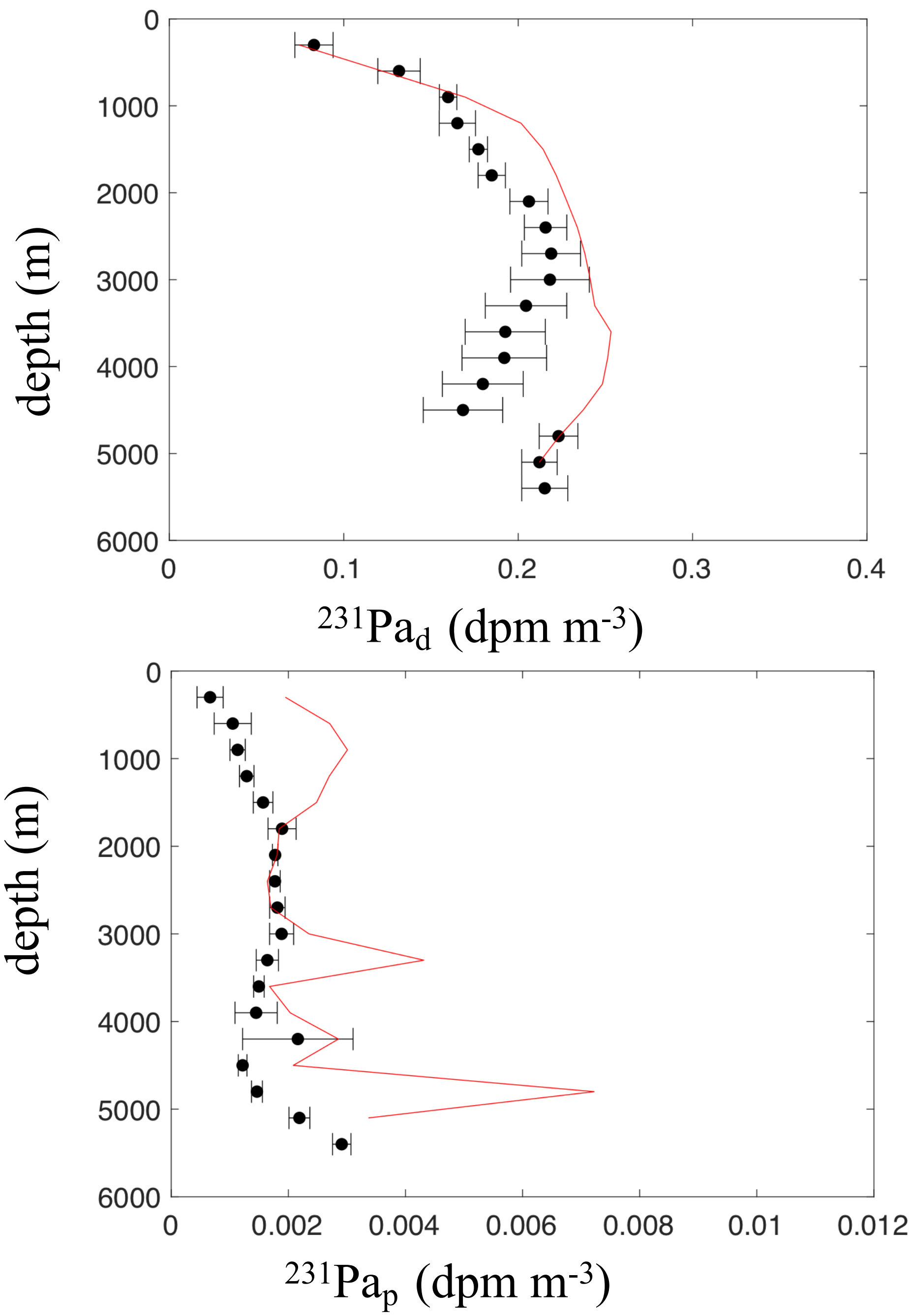

Fig. 10. Profile of station-averaged $^{231}\mathrm{Pa}_d$ (top) and $^{231}\mathrm{Pa}_p$ (bottom) as calculated from pre-GEOTRACES and GA03 measurements (black circles) and as simulated in the reference solution (red line). The circles show averages of measurements from several stations with the following exceptions: for

^{231}Pa$_d$ (^{231}Pa$_p$), the three (four) deepest circles show measurements from a single station (GT11-12). The horizontal bars show the standard errors of the averages (measurement error for the three (four) deepest measurements of ^{231}Pa$_d$ (^{231}Pa$_p$); Table 1). The extreme values of ^{231}Pa$_p$ near the bottom of stations GT11-04 and GT11-08 are excluded from the station-averaged profile of the measurements.

1) Distribution of ^{230}Th

The vertical profile of ^{230}Th$_d$ obtained by averaging the available data in the study area is reproduced rather closely in the reference solution (Fig. 9). The solution shows both the ^{230}Th$_d$ increase with depth in the upper $\sim$ 3000 m and the ^{230}Th$_d$ decrease below. The good agreement of the model with the data holds over most of the water column, except for the three deepest observations. In contrast to ^{230}Th$_d$, and consistent with the observed averages, the station-averaged ^{230}Th$_p$ simulated by the model increases generally downwards over the entire ocean depth, although the observed ^{230}Th$_p$ are generally overestimated by the model (Fig. 9).

Similarly to the station averages, the simulated ^{230}Th$_d$ and ^{230}Th$_p$ profiles compare in general favourably with the observed profiles at individual stations (Figs. A8 and A10). Noticeable differences with the observations occur at pre-GEOTRACES station S1 (Guo et al. 1995) where ^{230}Th$_p$ data in the upper 1000 m of the water column are underestimated (Fig. A8), and at station GT11-12 where ^{230}Th$_d$ data below $\sim$ 3000 m are also underpredicted (Fig. A9). The reference solution generally overestimates ^{230}Th$_p$ at GA03 stations, particularly (i) below $\sim$ 2000 m at stations GT11-03, GT11-04, GT11-06, and GT11-08 and (ii) over most of the water column at the deeper stations GT11-10 and GT11-12 (Fig. A10). Thus, whereas the reference solution captures reasonably well the station-averaged profiles of ^{230}Th$_{d,p}$ in the western North Atlantic, it is less successful at explaining the observations made at individual stations.

For future reference, we provide measures of the (dis)agreement of the reference solution with activity measurements from pre-GEOTRACES campaigns and the western segment of GA03 (Fig. 11).

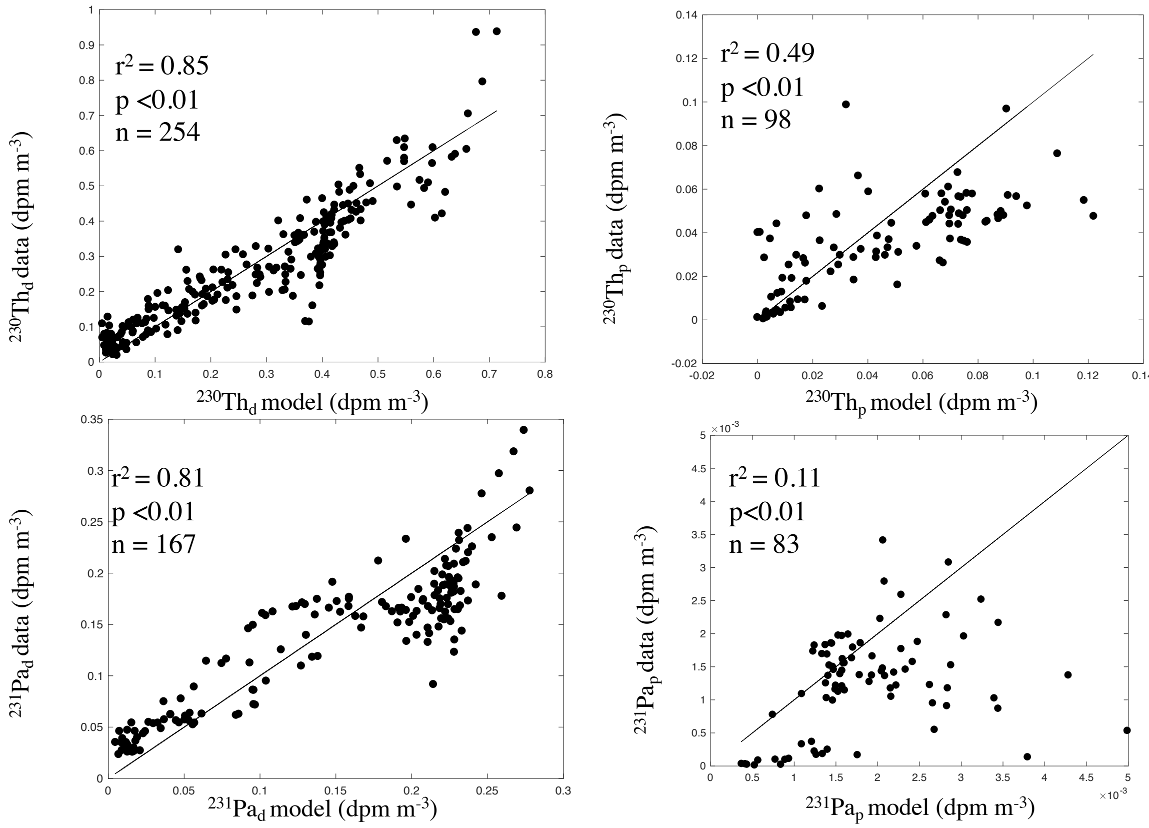

Fig. 11. Scatter plots of measured radionuclide activities versus simulated radionuclide activities in the reference solution. Shown in each panel are the squared Pearson correlation coefficient (r^2), the p value of the correlation, and the number of measurements (n). In each panel, the black line is the line of perfect agreement. For panel (b) and (d), the extreme measured values of $^{230}\mathrm{Th}_p$ and $^{231}\mathrm{Pa}_p$ near the bottom of stations GT11-04 and GT11-08, along with the corresponding model values, are excluded from the scatter plot.

We find that the reference solution accounts for 85% of the variance in the $^{230}\mathrm{Th}_d$ measurements ($n = 254$) and for 49% of the variance in the $^{230}\mathrm{Th}_p$ measurements ($n = 98$). The correlation between measured and simulated activities is very significant for both the dissolved phase and the particulate phase ($p < 0.01$). The root mean square difference between the measured and simulated activities amounts to 0.078 dpm m^{-3} for $^{230}\mathrm{Th}_d$ and to 0.028 dpm m^{-3} for $^{230}\mathrm{Th}_p$ (Table 4).

Table 4. Root Mean Square Difference Between Observed & Simulated Activities^a

	$^{230}Th_d$	$^{230}Th_p$	$^{231}Pa_d$	$^{231}Pa_p$
n	238	100	161	84
reference solution	0.078	0.028	0.039	0.001
k_1' / 2	0.086	0.025	0.041	0.001
$k_1' \times 2$	0.086	0.037	0.037	0.003
DWBC inflow = 10 Sv	0.081	0.030	0.040	0.002
DWBC inflow = 40 Sv	0.076	0.029	0.037	0.002
$A_{d,p}$(DWBC inflow) / 2	0.078	0.025	0.033	0.001
$A_{d,p}$(DWBC inflow) $\times$ 2	0.165	0.041	0.110	0.002
uniform $k_1(Th)$ & $k_1(Pa)$	0.075	0.043	0.041	0.002
$A_{d,p}$(DWBC inflow) / 2, DWBC inflow = 10 Sv	0.093	0.027	0.041	0.002

^{a} All values in dpm m^{-3}

2) Distribution of ^{231}Pa

The station-averaged $^{231}Pa_d$ for (pre-)GEOTRACES data are broadly reproduced in the reference solution in the upper 3000 m of the water column, but they are overpredicted at greater depths except near 5000 m (Fig. 10). The reversal in the vertical $^{231}Pa_d$ gradient occurs deeper in the model simulation (at $\sim$ 4000 m) than in the observations ($\sim$ 3000 m). As for $^{231}Pa_d$, the station-averaged $^{231}Pa_p$ computed from GA03 data tend to be overestimated at most levels in the reference solution, except between about 2000–3000 m where the simulation agrees closely with the observational averages. Note that the station-averaged profiles of $^{231}Pa_{d,p}$ are largely unaltered if w_p for $^{231}Pa_p$ is decreased from its reference value of 2400 m yr^{-1} to 1800 m yr^{-1}, the value used for $^{230}Th_p$ (not shown). The simulated $^{231}Pa_d$ profiles show in general the closest agreement with the measured $^{231}Pa_d$ profiles at individual stations in the upper $\sim$ 3000 m of the water column (Figs. A11 and A12). Below this depth, the model overestimates the $^{231}\mathrm{Pa}_d$ measurements, with the notable exception of station GT11-12, where the observed $^{231}\mathrm{Pa}_d$ are rather closely reproduced below 3000 m and underestimated between about 2000–3000 m. Inspection of $^{231}\mathrm{Pa}_p$ profiles at individual stations shows that the largest differences between the simulated and observed $^{231}\mathrm{Pa}_p$ occur near the seafloor at stations GT11-03 to GT11-08 and in the upper $\sim$ 2000 m at station GT11-10 (Fig. A13).

As for $^{230}\mathrm{Th}_{d,p}$, we quantify the (dis)agreement of the reference solution with (pre-)GEOTRACES measurements of $^{231}\mathrm{Pa}_{d,p}$ activities (Fig. 11). The reference solution "explains" 81% of the variance in the $^{231}\mathrm{Pa}_d$ measurements ($n = 167$) and only 11% of the variance in the $^{231}\mathrm{Pa}_p$ measurements ($n = 83$). The correlation between measured and simulated activities is very significant, even for the particulate phase ($p < 0.01$). The root mean square difference between the simulated and observed activities amounts to 0.039 dpm m^{-3} for $^{231}\mathrm{Pa}_d$ and to 0.001 dpm m^{-3} for $^{231}\mathrm{Pa}_p$ (Table 4).

3) Comparison to Sediment ^{231}Pa/^{230}Th

The enhanced deposition of particle-reactive substances in ocean-margin sediments is often referred to as 'boundary scavenging' (Spencer et al. 1981). Anderson et al. (1994) found that deposition rates of ^{230}Th and ^{231}Pa measured during the SEEP-I and SEEP-II programs in the Middle Atlantic Bight exceed their local rates of supply, consistent with boundary scavenging. However, they also found that the ^{231}Pa/^{230}Th activity ratios of surface sediments are consistently less than the ^{231}Pa/^{230}Th production ratio of 0.093, which is at odds with the notion that ^{231}Pa should be preferentially deposited over ^{230}Th in marginal sediments (^{231}Pa is generally less prone to particle scavenging than ^{230}Th and thus more likely to be transported away from its production site). The authors postulated that the anomalous boundary scavenging of ^{230}Th and ^{231}Pa in the Middle Atlantic Bight could be explained by the export from the region of fine-grained Mn-rich particles that would scavenge greater portions of $^{231}\mathrm{Pa}_d$ than of $^{230}\mathrm{Th}_d$.

In this section, the distribution of $^{231}\mathrm{Pa}_p/^{230}\mathrm{Th}_p$ near the bottom (deepest grid point) which is simulated in the reference solution is compared to surface sediment ^{231}Pa/^{230}Th data which are available in the western North Atlantic (Table 5).

Table 5. Surface sediment ^{231}Pa/^{230}Th data in the western North Atlantic.

core	latitude	longitude	depth (m)	^{231}Pa/^{230}Th	reference
OCE152-BC1	39.49°N	70.57°W	1126	0.082	Anderson et al. (1994)
OCE152-BC8	32.47°N	70.58°W	1596	0.071	Anderson et al. (1994)
OCE152-BC9	39.42°N	70.55°W	1981	0.091	Anderson et al. (1994)
OCE152-BC5	39.08°N	70.56°W	2691	0.063	Anderson et al. (1994)
EN123-BC4	39.48°N	70.56°W	1280	0.076	Anderson et al. (1994)
EN123-BC6	39.49°N	70.55°W	1643	0.066	Anderson et al. (1994)
EN123-BC3	39.35°N	70.55°W	2344	0.061	Anderson et al. (1994)
EN123-BC1	39.08°N	70.55°W	2736	0.053	Anderson et al. (1994)
EN179-BC5	37.38°N	74.13°W	384	0.127	Anderson et al. (1994)
EN179-BC2	37.37°N	74.10°W	892	0.050	Anderson et al. (1994)
EN179-BC3	37.38°N	74.09°W	1031	0.075	Anderson et al. (1994)
EN179-BC4	37.32°N	74.02°W	1318	0.071	Anderson et al. (1994)
EN179-BC7	37.25°N	73.49°W	1989	0.051	Anderson et al. (1994)
EN187-BC4	37.37°N	74.13°W	512	0.063	Anderson et al. (1994)
EN187-BC10	36.52°N	74.37°W	580	0.089	Anderson et al. (1994)
EN187-BC8	36.52°N	74.34°W	1020	0.053	Anderson et al. (1994)
EN187-BC5	37.37°N	74.10°W	1045	0.069	Anderson et al. (1994)
EN187-BC11	37.02°N	74.34°W	1125	0.062	Anderson et al. (1994)
EN187-BC9	36.52°N	74.34°W	1165	0.075	Anderson et al. (1994)
EN187-BC6	37.24°N	73.5°W	2000	0.055	Anderson et al. (1994)
OCE325-GGC5	33.7°N	57.6°W	4550	0.054	McManus et al. (2004)
VM26-176	32.76°N	70.78°W	1126	0.065	Yu (1994)

The sediment ^{231}Pa/^{230}Th data used for this comparison originate from the compilation reported by Henry et al. (2016) and come for the most part from the SEEP-I and SEEP-II programs (Anderson et al. 1994).

It is seen that the near-bottom ^{231}Pa$_p$/^{230}Th$_p$ ratio in our reference solution show relative minima between 1000–3000 m in the Middle Atlantic Bight; east of the 3000-m isobath, the simulated ^{231}Pa$_p$/^{230}Th$_p$ present maxima in multiple regions predominately located in the northern part of the domain (Fig. 12).

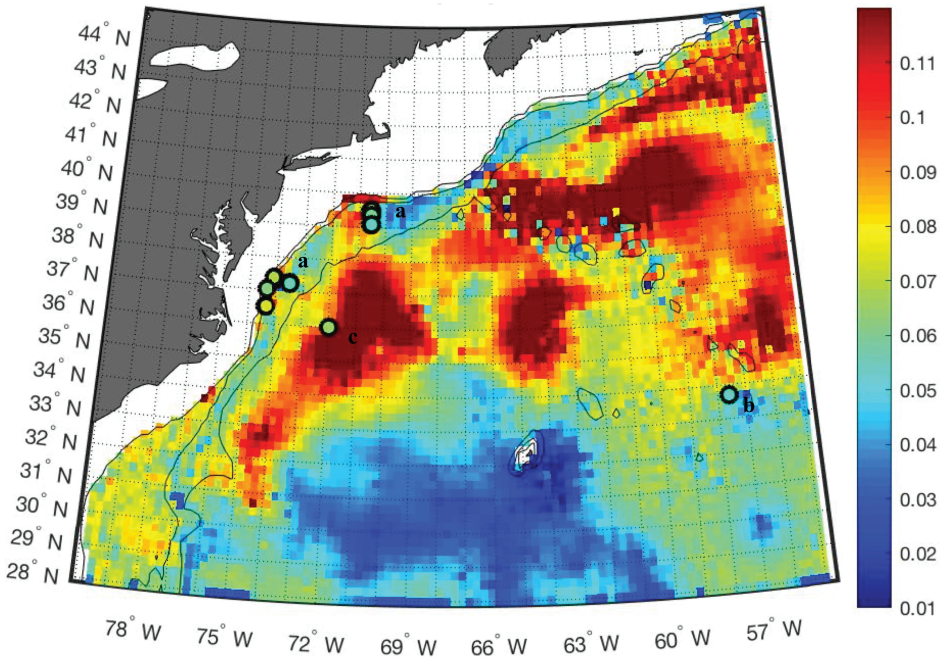

Fig. 12. Distribution of near-bottom $^{231}Pa_p/^{230}Th_p$ in the reference experiment. The filled circles are surface sediment data (Table 5), and the solid black lines are the 200 m, 1000 m, and 3000 m isobath, respectively.

The simulation of $^{231}Pa_p/^{230}Th_p$ ratios below the production ratio of 0.093 along the margin is consistent with measurements of surface sediment $^{231}Pa/^{230}Th$ in the Middle Atlantic Bight, suggesting that the export of fine-grained Mn-rich particles (Anderson et al. 1994) may not be necessary to explain the anomalous boundary scavenging observed in the Bight. In other words, sediment $^{231}Pa_p/^{230}Th_p$ ratios below the production ratio may also arise from the joint effects of ocean circulation and particle scavenging as represented in our model. The dissolved and particulate $^{231}Pa/^{230}Th$ ratios at the DWBC inflow are set to, respectively, $0.22/0.40 = 0.55$ and $0.003/0.03 = 0.10$ (Appendix C), i.e., to values that exceed the $^{231}Pa/^{230}Th$ production ratio. Consequently, the near-bottom $^{231}Pa_p/^{230}Th_p$ ratios below the production ratio which are simulated in the Middle Atlantic Bight do not reflect the $^{230}Th_{d,p}$ and $^{231}Pa_{d,p}$ values set at the boundary but should rather result from processes operating within the model domain. On the other hand, the sediment $^{231}Pa/^{230}Th$ show a positive but insignificant relationship with the simulated $^{231}Pa_p/^{230}Th_p$ (Fig. 13), indicating that the ability of the model to explain the variability of sediment $^{231}Pa/^{230}Th$ within the Bight is very limited. Various factors could explain the small correlation between the simulated near-bottom $^{231}Pa_p/^{230}Th_p$ and the measured sediment $^{231}Pa/^{230}Th$, such as (i) model errors, including errors due to the omission of the process postulated by Anderson et al. (1994), (ii) bioturbation within the sediment column, and (iii) sediment lateral redistribution (e.g., Kretschmer et al. (2010, 2011)).

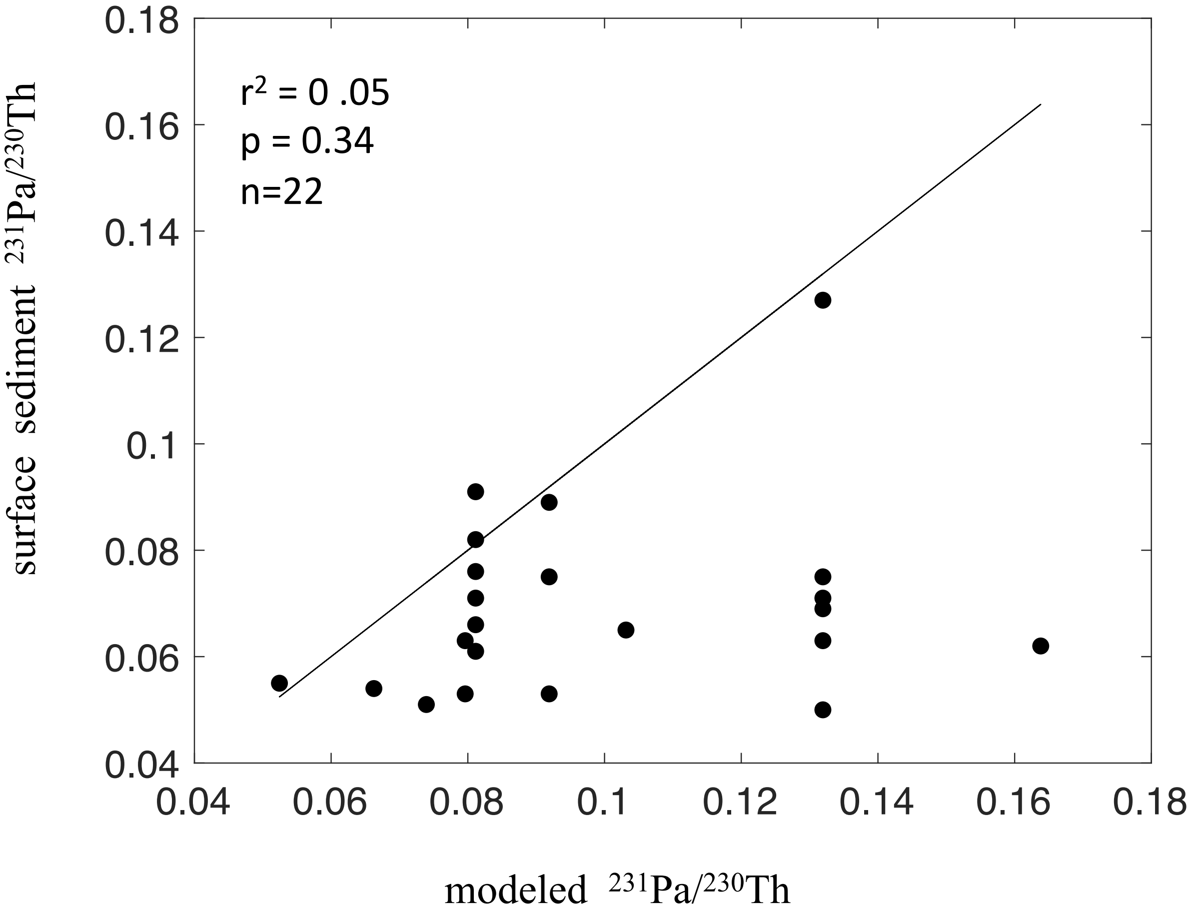

Fig. 13. Scatter plot of surface sediment ^{231}Pa/^{230}Th data versus the near-bottom $^{231}\mathrm{Pa}_p/^{230}\mathrm{Th}_p$ simulated near the corresponding data location in the reference experiment. The regression coefficient (slope) is 0.35 ± 0.36 (one standard error) and the Pearson correlation coefficient is 0.21 ($n = 22$). The black line is the line of perfect agreement.

5. Sensitivity Experiments

In this section, we explore the sensitivity of the $^{230}\mathrm{Th}_{d,p}$ and $^{231}\mathrm{Pa}_{d,p}$ distributions simulated by the circulation-geochemical model to the intensity of particle scavenging and to properties of the DWBC. Specifically, numerical experiments are conducted with varying values of (i) the sensitivity of the adsorption rate constant k_1 to particle concentration (k_1'), (ii) the volume transport of the Deep Western Boundary Current at its inflow location, or (iii) the $^{230}\mathrm{Th}_{d,p}$ and $^{231}\mathrm{Pa}_{d,p}$ activities of the DWBC at its inflow location. For each experiment, the other model parameters and boundary conditions are the same as those for the reference solution (section 4).

a. Particle Scavenging Intensity

We consider two numerical experiments where the sensitivity of k_1 to P is either halved or doubled relatively to the values of k_1' assumed for Th and Pa in the reference solution (Table 3). Consider first the effect of changing k_1' for Th, k_1'(Th), from its reference value of 0.04 $\mathrm{yr^{-1}\ mg^{-1}\ m^3}$ to either 0.02 or 0.08 $\mathrm{yr^{-1}\ mg^{-1}\ m^3}$. A larger value of k_1' means that a larger influence of PM concentration and hence of BNLs on chemical scavenging is incorporated into the model. As expected, $^{230}\mathrm{Th}_d$ is found to decrease and $^{230}\mathrm{Th}_p$ is found to increase as k_1'(Th) is enhanced (top panels of Fig. 14).

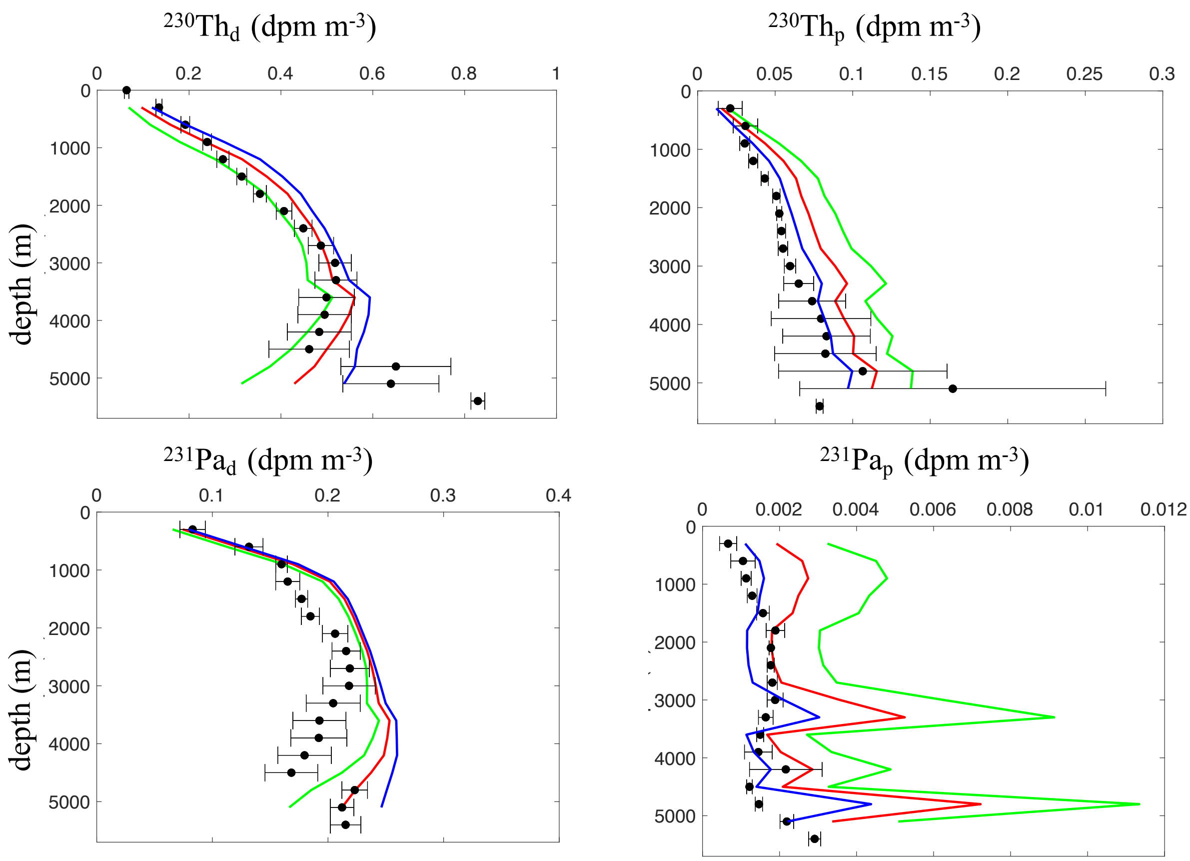

Fig. 14. Profile of station-averaged $^{230}\mathrm{Th}_{d,p}$ (top) and $^{231}\mathrm{Pa}_{d,p}$ (bottom) as calculated from (pre-)GEOTRACES measurements (black circles) and as simulated for $k_1'(\mathrm{Th}) = 0.02\ \mathrm{yr^{-1}\ mg^{-1}\ m^3}$ and $k_1'(\mathrm{Pa}) = 0.01\ \mathrm{yr^{-1}\ mg^{-1}\ m^3}$ (blue lines), $k_1'(\mathrm{Th}) = 0.04\ \mathrm{yr^{-1}\ mg^{-1}\ m^3}$ and $k_1'(\mathrm{Pa}) = 0.02\ \mathrm{yr^{-1}\ mg^{-1}\ m^3}$ (red, reference solution), and $k_1'(\mathrm{Th}) = 0.08\ \mathrm{yr^{-1}\ mg^{-1}\ m^3}$ and $k_1'(\mathrm{Pa}) = 0.04\ \mathrm{yr^{-1}\ mg^{-1}\ m^3}$ (green). The circles show averages of measurements from several stations, with the exceptions listed in Figure 9 for $^{230}\mathrm{Th}_{d,p}$ and in Figure 10 for $^{231}\mathrm{Pa}_{d,p}$. The horizontal bars show the standard errors of the averages (measurement error for the shallowest $^{230}\mathrm{Th}_d$ measurement, the deepest $^{230}\mathrm{Th}_{d,p}$ measurements, and the three (four) deepest measurements of $^{231}\mathrm{Pa}_d$ ($^{231}\mathrm{Pa}_p$); Table 1). The extreme values of $^{230}\mathrm{Th}_p$ (Fig. 3) and

^{231}Pa$_p$ (Fig. 6) near the bottom of stations GT11-04 and GT11-08 are excluded from the station-averaged profile of the measurements.

The agreement with ^{230}Th$_d$ measured at (pre-)GEOTRACES stations, however, is only weakly modified compared to the reference solution: the root mean square difference between the observed and simulated ^{230}Th$_d$, rmsd(^{230}Th$_d$), amounts to 0.086 dpm m^{-3} for both k_1'(Th) = 0.02 and 0.08 yr^{-1} mg^{-1} m^3 (Table 4). The solution with k_1'(Th) = 0.02 yr^{-1} better describes the observed ^{230}Th$_p$ averages than the reference solution, although the agreement with the observed ^{230}Th$_d$ averages deteriorates (Fig. 14) and rmsd(^{230}Th$_p$) is only slightly reduced compared to the reference solution (Table 4). The solution with k_1'(Th) = 0.08 yr^{-1} mg^{-1} m^3 strongly overestimates the observed ^{230}Th$_p$ averages over most of the water column, except near the surface and the bottom of the profile (Fig. 14), with rmsd(^{230}Th$_p$) reaching 0.037 dpm m^{-3} (Table 4).

Consider then the effect of altering k_1'(Pa) from its reference value of 0.02 yr^{-1} mg^{-1} m^3 to either 0.01 or 0.04 yr^{-1} mg^{-1} m^3 (bottom panels of Fig. 14). Similarly to ^{230}Th$_{d,p}$, the station-averaged ^{231}Pa$_d$ (^{231}Pa$_p$) decrease (increase) as k_1'(Pa) is enhanced. Interestingly, the ^{231}Pa$_d$ averages simulated by the model show a small sensitivity to k_1'(Pa) in the upper $\sim$ 3000 m, which suggests that particle scavenging is in general a small term in the budget of ^{231}Pa$_d$ in this part of the water column. Compared to the reference solution, the low ^{231}Pa$_d$ averages observed below 3000 m are better reproduced by the model if Pa adsorption onto particles is assumed to be more sensitive to particle concentration, although rmsd(^{231}Pa$_d$) is reduced only slightly (Table 4). However, in this case, the model strongly overestimates the ^{231}Pa$_p$ averages observed over the entire column (Fig. 14), which illustrates a difficulty to explain simultaneously the observed ^{231}Pa in dissolved and particulate forms. As shown above, a similar difficulty arises for ^{230}Th, although the reference solution appears to better reproduce the observed ^{230}Th$_{d,p}$ averages than the observed ^{231}Pa$_{d,p}$ averages (Fig. 14).

b. *Strength of the DWBC Inflow*

We now examine how the strength of the Deep Western Boundary Current at its inflow location (between 42.5–44.875°N along 55°W; Appendix C) affects the distributions of ^{230}Th and ^{231}Pa in both dissolved and particulate forms in the western North Atlantic domain. Observations along the continental slope and rise in the western North Atlantic suggest considerable temporal variations in the volume transport of the DWBC. Four repeat hydrographic sections across the DWBC at 55°W were occupied in order to investigate the inter-annual variability of the deep flow (Pickart and Smethie 1998). The volume transport was estimated from geostrophic velocities in four density layers corresponding to Upper Labrador Sea Water (ULSW), Classical Labrador Sea Water (CLSW), Iceland-Scotland Overflow Water (ISOW), and Denmark Strait Overflow

Water (DSOW). The 4-layer summed transport during occupations in 1991, 1994, and 1995 was estimated to range from 12.6 to 25.2 Sv, with an average of 18.8±6.3 Sv. More recently, current meter observations collected along line W from May 2004 to April 2008 showed that the 5-d averaged transport summed in the ULSW, CLSW, ISOW, and DSOW layers ranged from 3.5 Sv to 79.9 Sv, with a record mean of 25.1 Sv and standard deviation of 12.5 Sv (Toole et al. 2011). Bias adjustment to account for the finite width of the mooring array increased the mean transport estimate to 28.7 Sv (Toole et al. 2011).

Here two numerical experiments are considered, where the volume transport of the DWBC inflow is changed from its value of 20 Sv in the reference solution to either 10 Sv or 40 Sv. These experiments are not intended to be realistic; their sole purpose is to document the sensitivity of the radionuclide distributions to sizeable variations in the strength of the DWBC inflow in the model. It is seen that the station-averaged profiles of $^{230}\mathrm{Th}_{d,p}$ and $^{231}\mathrm{Pa}_{d,p}$ experience only modest changes if the DWBC inflow is strengthened from 10 to 40 Sv (Fig. 15).

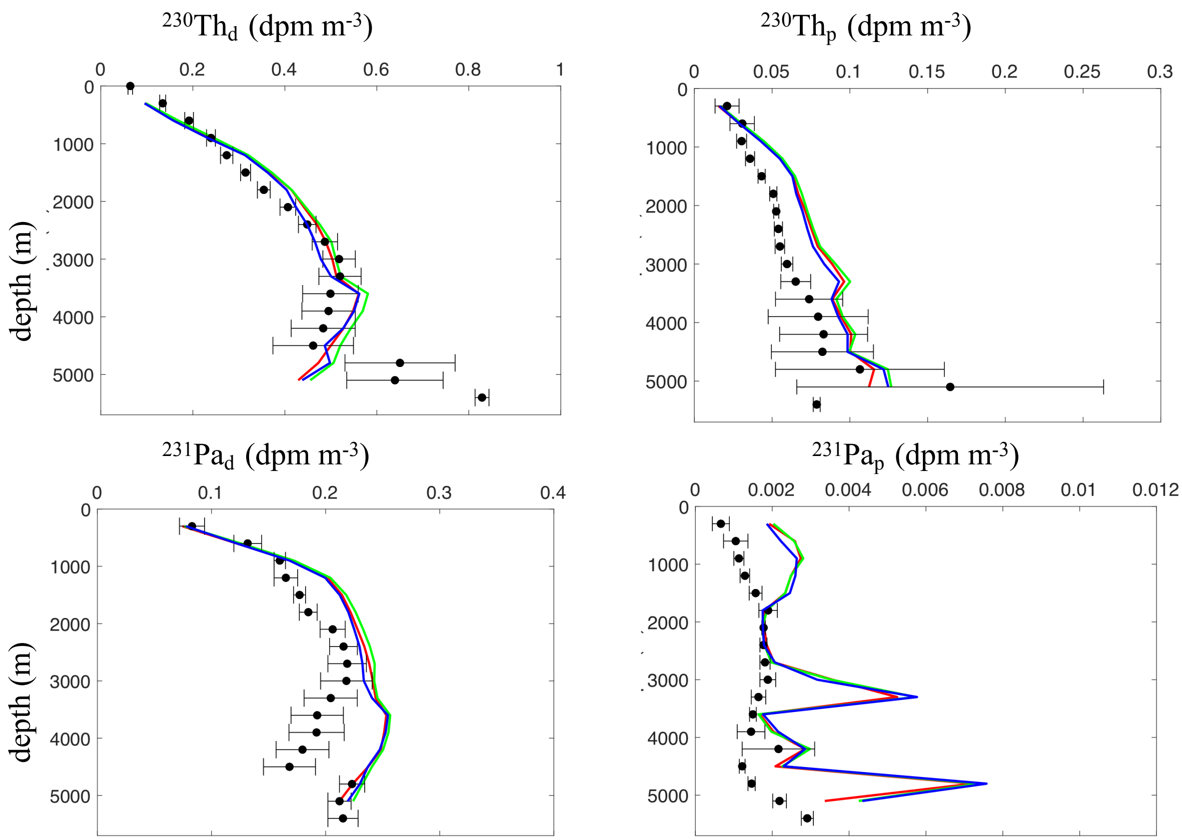

Fig. 15. Profile of station-averaged $^{230}\mathrm{Th}_{d,p}$ (top) and $^{231}\mathrm{Pa}_{d,p}$ (bottom) as calculated from (pre-)GEOTRACES measurements (black circles) and as simulated when the strength of the DWBC at its inflow location is set to 10 Sv (green lines), 20 Sv (red, reference solution), and 40 Sv (blue). The circles show averages of measurements from several stations, with the exceptions listed in Figure 9 for $^{230}\mathrm{Th}_{d,p}$

and in Figure 10 for $^{231}\mathrm{Pa}_{d,p}$. The horizontal bars show the standard errors of the averages (measurement error for the shallowest $^{230}\mathrm{Th}_d$ measurement, the deepest $^{230}\mathrm{Th}_{d,p}$ measurements, and the three (four) deepest measurements of $^{231}\mathrm{Pa}_d$ ($^{231}\mathrm{Pa}_p$); Table 1). The extreme values of $^{230}\mathrm{Th}_p$ (Fig. 3) and $^{231}\mathrm{Pa}_p$ (Fig. 6) near the bottom of stations GT11-04 and GT11-08 are excluded from the station-averaged profile of the measurements.

The differences between the simulated radionuclide activities and the measured radionuclide activities from (pre-)GEOTRACES cruises are not greatly altered by changes in the DWBC inflow: as the DWBC inflow is increased from 10 to 40 Sv, rmsd($^{230}\mathrm{Th}_d$) changes from 0.081 to 0.076 dpm m^{-3}, rmsd($^{230}\mathrm{Th}_p$) from 0.030 to 0.029 dpm m^{-3}, and rmsd($^{231}\mathrm{Pa}_d$) from 0.040 to 0.037 dpm m^{-3}, whereas rmsd($^{231}\mathrm{Pa}_p$) amounts to the same value of 0.002 dpm m^{-3} (Table 4).

Notice that the small variations of the station-averaged profiles with DWBC inflow do not imply that the DWBC inflow has also a modest influence on local radionuclide profiles. A change in DWBC inflow from 10 to 40 Sv does produce appreciable changes at some locations, particularly in the vicinity of the inflow and near the depth of the current core (not shown).

c. *Radionuclide Activities in the DWBC Inflow*

Finally, we explore the sensitivity of the $^{230}\mathrm{Th}_{d,p}$ and $^{231}\mathrm{Pa}_{d,p}$ distributions to the radionuclide activities which are assumed at the location of the DWBC inflow. Although ^{230}Th and ^{231}Pa measurements are not available to constrain the variability of the two radionuclides near this location, hydrographic observations indicate that water properties of the DWBC can exhibit significant inter-annual variations. In their analysis of repeat sections along 55°W, Pickart and Smethie (1998) reported that the largest property variability between 1983–1995 occurred in the CLSW, which in the 1990s became markeldy colder, fresher, and richer in dissolved oxygen and CFCs, all suggestive of 'new ventilation'. Observations along line W from 1995 to 2014 revealed water mass changes that are consistent with changes in source water properties upstream in the Labrador Sea (Le Bras et al. 2017). Particularly evident was the cold, dense, and deep class of Labrador Sea Water (dLSW) that was presumably created by recurring convection events during severe winters in 1987–1994. From 2010 to 2014, the density of DSOW within the DWBC along line W was found to decrease as a result of warming overcompensating a slight salinity increase (Andres et al. 2016).

Here we consider two numerical experiments where the $^{230}\mathrm{Th}_{d,p}$ and $^{231}\mathrm{Pa}_{d,p}$ activities at the DWBC inflow location are halved or doubled, compared to their respective values in the reference solution (Appendix C). It is seen that the station-averaged $^{230}\mathrm{Th}_{d,p}$ and $^{231}\mathrm{Pa}_{d,p}$ vary markedly at most depths in response to variations in radionuclide activities at the DWBC inflow (Fig. 16).

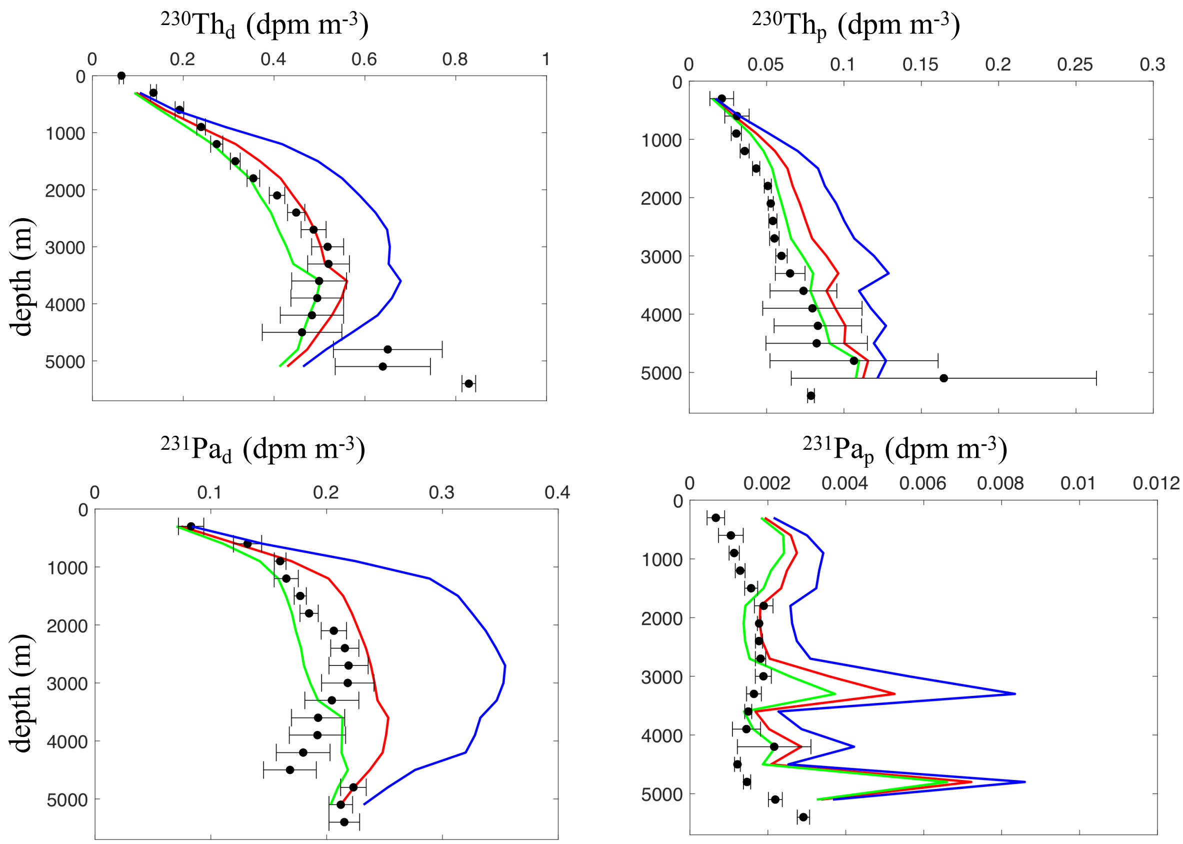

Fig. 16. Profile of station-averaged $^{230}\mathrm{Th}_{d,p}$ (top) and $^{231}\mathrm{Pa}_{d,p}$ (bottom) as calculated from (pre-)GEOTRACES measurements (black circles) and as simulated when the radionuclide activities at the DWBC inflow are halved (green lines) or doubled (blue) compared to their values in the reference solution (red). The circles show averages of measurements from several stations, with the exceptions listed in Figure 9 for $^{230}\mathrm{Th}_{d,p}$ and in Figure 10 for $^{231}\mathrm{Pa}_{d,p}$. The horizontal bars show the standard errors of the averages (measurement error for the shallowest $^{230}\mathrm{Th}_d$ measurement, the deepest $^{230}\mathrm{Th}_{d,p}$ measurements, and the three (four) deepest measurements of $^{231}\mathrm{Pa}_d$ ($^{231}\mathrm{Pa}_p$); Table 1). The extreme values of $^{230}\mathrm{Th}_p$ (Fig. 3) and $^{231}\mathrm{Pa}_p$ (Fig. 6) near the bottom of stations GT11-04 and GT11-08 are excluded from the station-averaged profile of the measurements.

As a result, the agreement with observational averages is noticeably modified: as $^{230}\mathrm{Th}_{d,p}$ and $^{231}\mathrm{Pa}_{d,p}$ at the DWBC inflow are changed from half to twice their reference values, rmsd($^{230}\mathrm{Th}_d$) (rmsd($^{230}\mathrm{Th}_p$)) varies from 0.078 and 0.165 dpm m^{-3} (0.025 to 0.041 dpm m^{-3}), whereas rmsd($^{231}\mathrm{Pa}_d$) (rmsd($^{231}\mathrm{Pa}_p$)) varies from 0.033 and 0.110 dpm m^{-3} (0.001 to 0.002 dpm m^{-3}) (Table 4). Thus, in the model, the radionuclide contents of the DWBC inflow more strongly influence the station-averaged profiles than the strength of the DWBC inflow.

6. Discussion

The results presented in section 4 show that the circulation-geochemical model considered in this study can capture most (> 80%) of the variance in the measurements of ^{230}Th and ^{231}Pa in the dissolved phase obtained from (pre-)GEOTRACES cruises in the western North Atlantic. Notably, the reversal in the ^{230}Th$_d$ and ^{231}Pa$_d$ gradients observed at mid-depth can be reproduced by the model, though too deeply by ~ 1000 m on average for ^{231}Pa$_d$. Results from sensitivity experiments (section 5) show that measurements of ^{230}Th and ^{231}Pa in the particulate phase could also be broadly reproduced, although a model simulation could not be found that closely replicates radionuclide measurements in the two phases simultaneously. Conceivably, a combination of model parameters and (or) boundary conditions different than the ones that have been tested could lead to a significantly better fit of model results with radionuclide measurements in the two phases. Such a combination, however, is probably best sought by using an inverse procedure, which is beyond the scope of this study.

Despite the difficulty experienced to closely replicate ^{230}Th and ^{231}Pa data in both the dissolved phase and the particulate phase, the present model does seem to be appropriate for investigating important questions about the observed distributions of ^{230}Th and ^{231}Pa in the western North Atlantic. Of particular significance are the observed reversals in the vertical ^{230}Th$_d$ and ^{231}Pa$_d$ gradients at mid-depth, leading to radionuclides activities in deep waters that are markedly lower near the western margin than far from the margin (Fig. 1). The model experiments illustrated in section 5 suggest that the elevated particle concentrations in benthic nepheloid layers could enhance chemical scavenging and hence produce the low ^{230}Th$_d$ and ^{231}Pa$_d$ activities which have been measured in these waters (Fig. 14).

In the remainder of this section, we first examine in more detail the importance of particle scavenging relatively to DWBC inflow in setting the radionuclide distributions in the western North Atlantic. Our results are then compared to those obtained in previous model studies. The potential of BNLs as sites of intensified scavenging and the possibility of significant temporal variations in chemical scavenging in the deep western North Atlantic are subsequently discussed. Finally, we clarify the implications of our results for the use of ^{230}Th as a ventilation tracer (e.g., Moran et al. (1997); Vogler et al. (1998); Moran et al. (2002)).

a. *Importance of Particle Scavenging*

We consider another experiment that further illustrates the potential role of spatial variations in particle scavenging, and of BNLs in particular, in setting the distributions of ^{230}Th and ^{231}Pa in the western North Atlantic. In this experiment, the apparent rate constants for Th and Pa adsorption are uniform and equal to the domain-averaged values of k_1(Th) and k_1(Pa) in the reference solution. This treatment ensures that the differences in the radionuclide distributions between this experiment and the reference experiment are due to different assumptions about spatial variations in k_1 (uniform versus non-uniform), and not due to different domain-averaged k_1 values.

We find that, with uniform k_1(Th) and k_1(Pa), $^{230}\mathrm{Th}_d$ and $^{231}\mathrm{Pa}_d$ averages increase monotonically with depth, in contrast to the reference solution (and the observations), which shows inversions in $^{230}\mathrm{Th}_d$ and $^{231}\mathrm{Pa}_d$ profiles at mid-depth (Fig. 17).

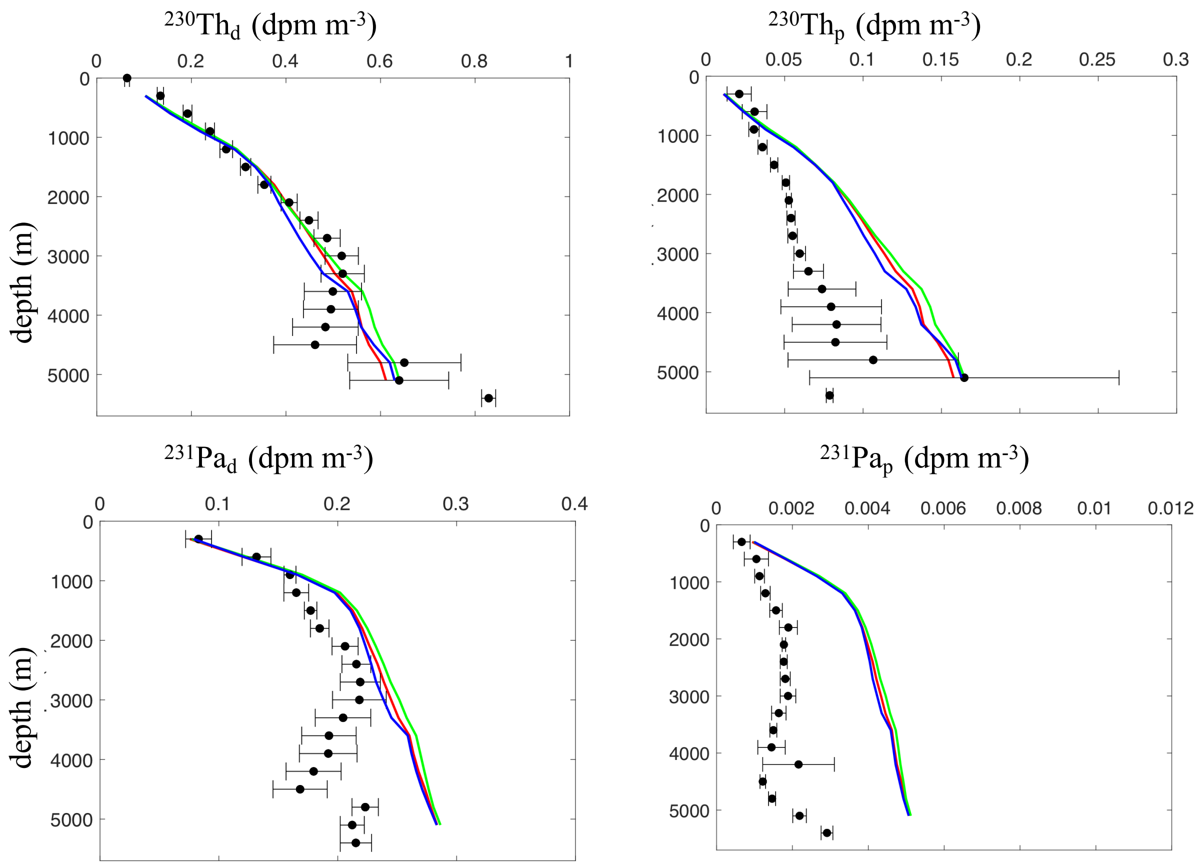

Fig. 17. Profile of station-averaged $^{230}\mathrm{Th}_{d,p}$ (top) and $^{231}\mathrm{Pa}_{d,p}$ (bottom) as calculated from (pre-)GEOTRACES measurements (black circles) and as simulated for uniform k_1(Th) and k_1(Pa) when the strength of the DWBC at its inflow location is set to 10 Sv (green lines), 20 Sv (red), and 40 Sv (blue). The circles show averages of measurements from several stations, with the exceptions listed in Figure 9 for $^{230}\mathrm{Th}_{d,p}$ and in Figure 10 for $^{231}\mathrm{Pa}_{d,p}$. The horizontal bars show the standard errors of the averages (measurement error for the shallowest $^{230}\mathrm{Th}_d$ measurement, the deepest $^{230}\mathrm{Th}_{d,p}$ measurements, and the three (four) deepest measurements of $^{231}\mathrm{Pa}_d$ ($^{231}\mathrm{Pa}_p$); Table 1). The extreme values of $^{230}\mathrm{Th}_p$ (Fig. 3) and $^{231}\mathrm{Pa}_p$ (Fig. 6) near the bottom of stations GT11-04 and GT11-08 are excluded from the station-averaged profile of the measurements.

As a result, the low $^{230}\mathrm{Th}_d$ and $^{231}\mathrm{Pa}_d$ activities observed in deep waters are not reproduced by the model. The root mean square differences for $^{230}\mathrm{Th}_{d,p}$ and $^{231}\mathrm{Pa}_{d,p}$ for uniform $k_1(\mathrm{Th})$ and $k_1(\mathrm{Pa})$ are comparable or higher than those for variable $k_1(\mathrm{Th})$ and $k_1(\mathrm{Pa})$ (Table 4). Experiments with a DWBC inflow of 10, 20, or 40 Sv all show a monotonic increase of $^{230}\mathrm{Th}_d$ and $^{231}\mathrm{Pa}_d$ with depth if $k_1(\mathrm{Th})$ and $k_1(\mathrm{Pa})$ are uniform (Fig. 17). Overall, these results suggest that the low $^{230}\mathrm{Th}_d$ and $^{231}\mathrm{Pa}_d$ activities observed near the western margin are more likely due to enhanced scavenging in the deep water column than to ventilation by $^{230}\mathrm{Th}_d$- and $^{231}\mathrm{Pa}_d$-poor waters from the western boundary.

The small sensitivity to changes in DWBC inflow (section 5b) may be a consequence of our choice of lateral boundary conditions. To test this possibility, we consider an experiment where two modifications to the reference experiment are brought simultaneously: (i) the DWBC inflow is increased from 20 Sv to 40 Sv and (ii) the radionuclide activities at the DWBC inflow location are halved compared to the reference values. The resulting values of the rmsd between observed and simulated activities are listed in Table 4. It is seen that these values are generally larger than those for the reference experiment and for the experiment where the activities at the DWBC inflow are halved but the strength of the DWBC inflow is kept equal to 20 Sv. Compared to these two experiments, strengthening the DWBC inflow and lowering the activities at the DWBC inflow noticeably lowers the average $^{230}\mathrm{Th}_{d,p}$ and $^{231}\mathrm{Pa}_{d,p}$ in the upper water column above $\sim$ 3500 m (Fig. 18). However, the dissolved and particulate activities below $\sim$ 3500 m remain largely unaltered in the experiment where (i) and (ii) are both implemented, suggesting that the small sensitivity of radionuclide activities in deep waters to changes in DWBC inflow is a robust result of the model.

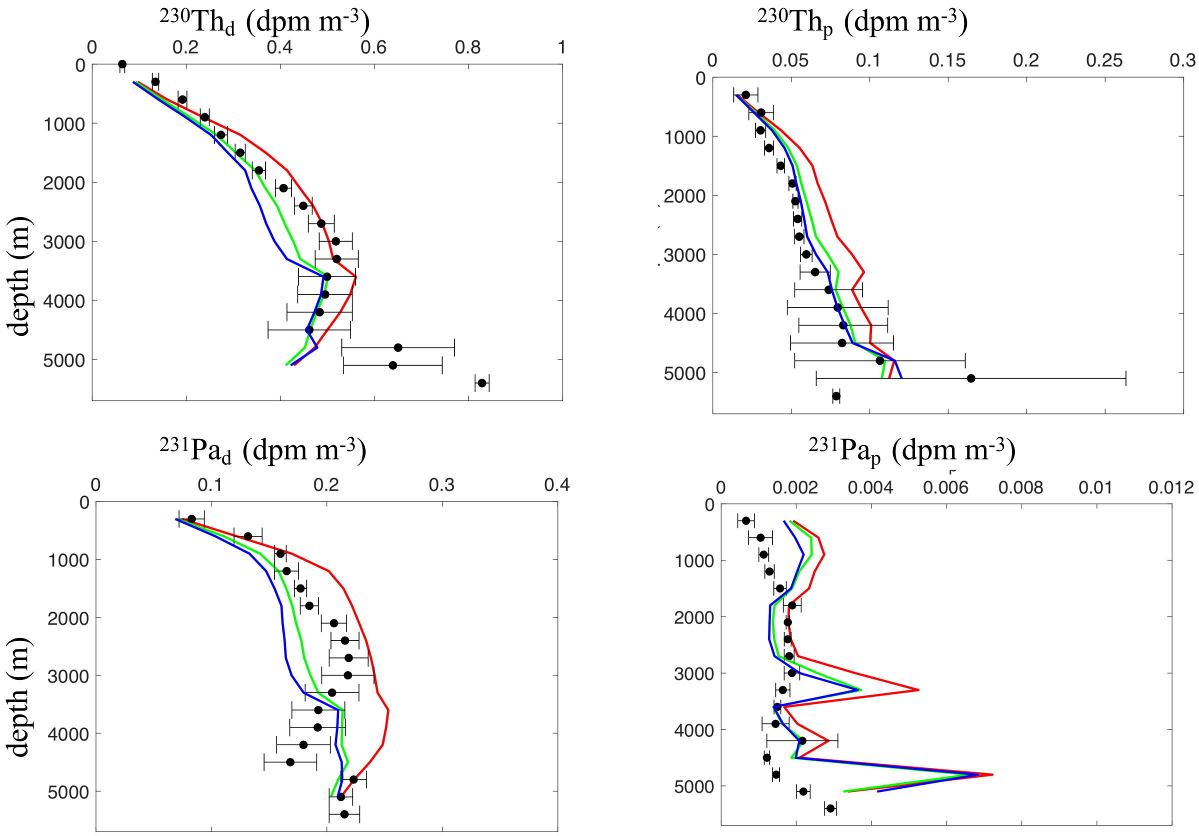

Fig. 18. Profile of station-averaged $^{230}\mathrm{Th}_{d,p}$ (top) and $^{231}\mathrm{Pa}_{d,p}$ (bottom) as calculated from (pre-)GEOTRACES measurements (black circles) and as simulated for the reference experiment (red), when the radionuclide activities at the DWBC inflow locations are halved (green), and when the radionuclide activities at the DWBC inflow locations are halved, and the DWBC at its inflow is 40 Sv (blue). The circles show averages of measurements from several stations, with the exceptions listed in Figure 9 for $^{230}\mathrm{Th}_{d,p}$ and in Figure 10 for $^{231}\mathrm{Pa}_{d,p}$. The horizontal bars show the standard errors of the averages (measurement error for the shallowest $^{230}\mathrm{Th}_d$ measurement, the deepest $^{230}\mathrm{Th}_{d,p}$ measurements, and the three (four) deepest measurements of $^{231}\mathrm{Pa}_d$ ($^{231}\mathrm{Pa}_p$); Table 1). The extreme values of $^{230}\mathrm{Th}_p$ (Fig. 3) and $^{231}\mathrm{Pa}_p$ (Fig. 6) near the bottom of stations GT11-04 and GT11-08 are excluded from the station-averaged profile of the measurements.

b. Comparison to Previous Model Studies

In this section, we briefly put our results in the context of three recent model studies on the distribution $^{231}\mathrm{Pa}$ and $^{230}\mathrm{Th}$ in the global ocean (Rempfer et al. 2017; Gu and Liu 2017; van Hulten et al. 2018). Some of the key differences between these previous models and the one considered in this study are worth mentioning. In these previous models, particle scavenging is determined from the distribution of different particle types simulated by the models, in contrast to our model which includes a single particle field directly based on observations. Moreover, the models of Gu and Liu (2017) and van Hulten et al. (2018) simulate total activities, not dissolved and particulate activities separately. This approach has the benefits that the radionuclide distributions can be calculated by solving a single equation and that sorption reactions need not be treated explictly, although it does require assumptions about solid-solution partitioning. Perhaps more important, none of these previous models represent the large particle concentrations that characterize benthic (and intermediate) nepheloid layers.

Interestingly, the difficulty to produce simulations that agree simultaneously with ^{230}Th and ^{231}Pa measurements in dissolved and particulate forms is a common result of all three models (Rempfer et al. 2017; Gu and Liu 2017; van Hulten et al. 2018). Rempfer et al. (2017) acknowledged the difficulty to produce a simulation that simultaneously accords with ^{230}Th and ^{231}Pa data in the two phases, and found that a better agreement is obtained by representing in their model additional sinks at the sea floor ('bottom scavenging') and at continental boundaries ('boundary scavenging'). van Hulten et al. (2018) reported that the $^{230}\mathrm{Th}_d$ and $^{231}\mathrm{Pa}_d$ distributions simulated by their model compare 'well' with GEOTRACES data in many parts of the ocean, but that $^{230}\mathrm{Th}_p$ and $^{231}\mathrm{Pa}_p$ activities are underpredicted because of missing particles from nepheloid layers. Finally, Gu and Liu (2017) stated that their model can simulate $^{230}\mathrm{Th}_d$ and $^{231}\mathrm{Pa}_d$ distributions that are in 'good agreement' with observations but that $^{230}\mathrm{Th}_p$ and $^{231}\mathrm{Pa}_p$ are generally smaller than observed in the deep ocean (and generally larger than observed in the surface ocean).

The difficulty to reproduce in the same simulation the observed radionuclide distributions in the two phases is also encountered in this work, although it is perhaps less severe owing to the consideration of BNLs and of the associated enhancement in particle scavenging in deep water. Rempfer et al. (2017) included simplified representations of 'bottom scavenging' and 'boundary scavenging' in their computationally efficient model with coarse horizontal resolution (36×36 grid cells). 'Bottom scavenging' was represented by applying a globally uniform concentration of resuspended particles to grid cells adjacent to the bottom, and 'boundary scavenging' was represented by increasing by a uniform factor the adsorption rate constant for ^{231}Pa in grid cells adjacent to continents. The simulation representing both forms of scavenging and illustrated in their paper (Rempfer et al. (2017); their Fig. 2) shows that the deep water $^{230}\mathrm{Th}_d$ and $^{231}\mathrm{Pa}_d$ activities are reduced compared to a simulation where 'bottom scavenging' and 'boundary scavenging' are absent. However, in this simulation, both $^{230}\mathrm{Th}_d$ and $^{231}\mathrm{Pa}_d$ appear to increase monotonically with depth, i.e., they did not seem to present the $^{230}\mathrm{Th}_d$ and $^{231}\mathrm{Pa}_d$ inversions at mid-depth as shown in observations and in our model. The apparent lack of $^{230}\mathrm{Th}_d$ and $^{231}\mathrm{Pa}_d$ inversions in the simulation illustrated by Rempfer et al. (2017) could be due to the fact that 'bottom scavenging' was represented only in the deepest grid cells of their model, whereas we allow for enhanced k_1 over the entire thickness of BNLs as estimated from the optically-derived particle field.

c. *BNLs as Sites of Intensified Scavenging*

Whereas boundary scavenging is expected to affect all particle-reactive species with long residence times, the processes leading to enhanced deposition of these species in marginal sediments are not completely understood. One process, however, could operate at many margins: the intensified scavenging in particle-rich nepheloid layers (benthic and intermediate) that may be found near continental slopes (for reviews see McCave (1986); Gardner et al. (2018a)). Benthic nepheloid layers near the western North American margin are characterized by particle concentrations that are much higher than, and particle compositions that are distinct from, those in surrounding waters (e.g., Lam et al. (2015); Gardner et al. (2017)). Particles sampled from BNLs near the western margin along GA03 presented concentration levels of up to 1648 mg m^{-3} and were dominated by lithogenic material (Lam et al. 2015). If the adsorption rates of particle-reactive metals increase with particle abundance, as postulated on theoretical grounds (e.g., Honeyman et al. (1988)) and supported by observational evidence (e.g., Honeyman et al. (1988); Lerner et al. (2017)), then these layers would be characterized by relatively large removal rates of Th and Pa from solution. Less obvious, however, is the effect of the chemical composition of resuspended sediment on Th and Pa scavenging in the water column. Lithogenic material was not found to strongly contribute to k_1 variance at GA03 stations east of Bermuda (Lerner et al. 2017), although this analysis focused on data collected outside BNLs. More generally, particles resuspended from the seabed would lead to scavenging rates that are different from those in surrounding waters if their chemical composition differs from that of the primary settling material from surface waters. Various factors could produce such differences: (i) temporal variations in the composition of the primary flux, (ii) diagenetic changes in the sediment (later resuspended), (iii) differential resuspension of particles by type and size, and (iv) different original sources for the resuspended material and the primary material (Gardner et al. 1985b).

Among the water samples from GA03 considered in this study, those collected near the bottom at stations GT11-04 and GT11-08 present particularly large anomalies in radionuclide activities. Measurements on near-bottom samples at these stations display relatively low values of dissolved ^{230}Th and ^{231}Pa (Figs. A2 and A5) and exceptionally high values of particulate ^{230}Th and ^{231}Pa (Figs. A3 and A6). Inspection of profiles of transmissometer data (voltage or particle beam attenuation coefficient) at GT11-04 and GT11-08 published in previous studies shows that these samples were collected in benthic nepheloid layers (e.g., Fig. 13 of Lam et al. (2015); Fig. 3 of Hayes et al. (2015a)). Here profiles of PM concentration at stations GT11-04 and GT11-08 are derived from measurements of the beam attenuation coefficient (BAC) obtained from transmissometry (WETLabs C-star 25-cm pathlength transmissometer with serial number CST-491DR; transmissometer data from Schlitzer et al. (2018)), using the empirical relationship between PM and BAC due to particles as reported by Gardner et al. (2018b). It is seen that both stations feature a well-defined BNL in the lower part of the water column (Fig. 19).

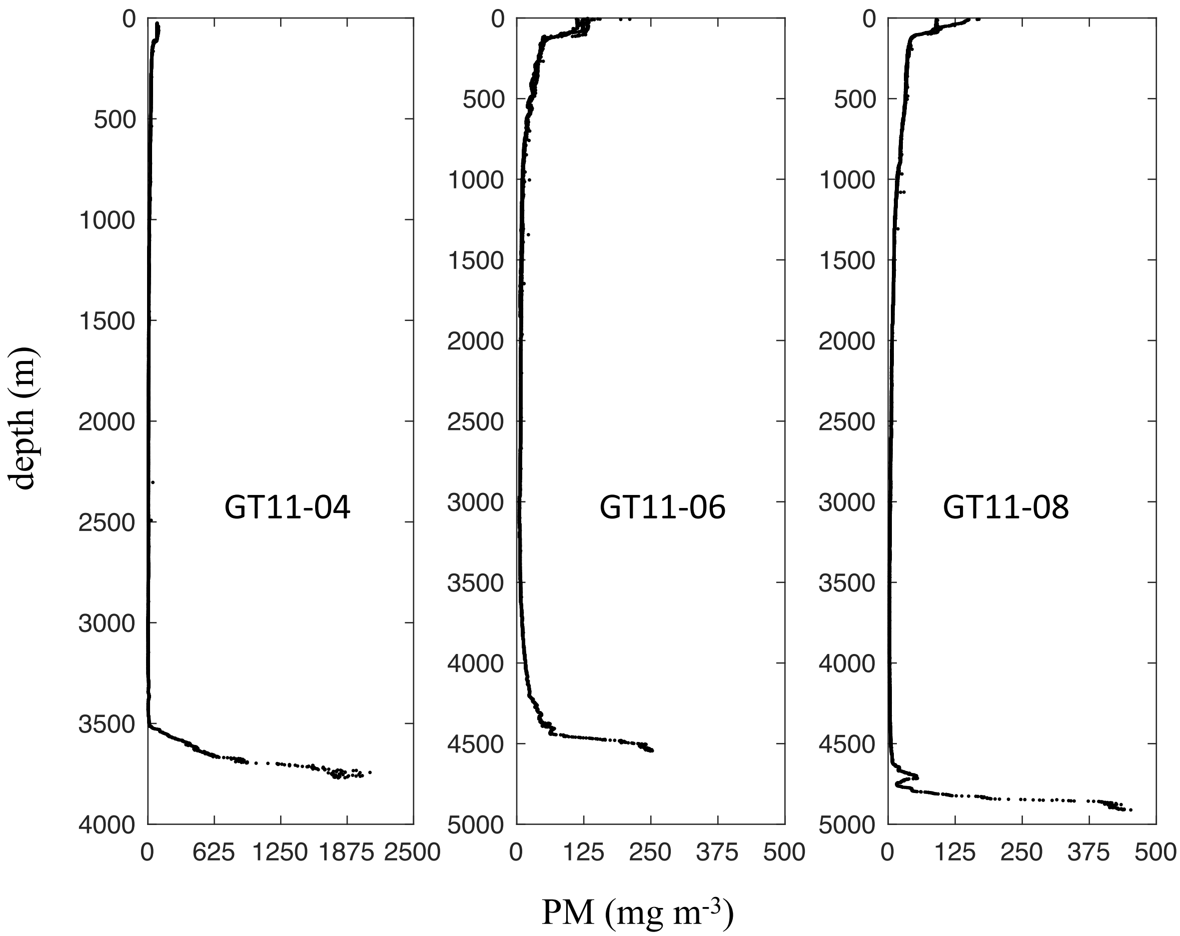

Fig. 19. Vertical profiles of optically derived particulate matter concentration at stations GT11-04, GT11-06, and GT11-08 between the New England continental shelf and Bermuda. Particulate matter concentration is estimated from beam attenuation coefficient measurements available in the GEOTRACES Intermediate Data Product (Schlitzer et al. 2018) using the empirical relationship between PM concentration and BAC due to particles as reported by Gardner et al. (2018b).

The concentration maxima amount to about 2100 and 450 mg m^{-3} near the bottom at GT11-04 and GT11-08, respectively, and exceed those in the surface waters at each station. The upper boundary of the BNL occurs at a water depth of about 3500 m at GT11-04 and about 4500 m at GT11-08, showing that samples presenting relatively low $^{230}Th_d$ and $^{231}Pa_d$ activities and exceptionally high $^{230}Th_p$ and $^{231}Pa_p$ activities at these stations (Figs. A3 and A6) originated from a strong BNL. Deep water samples collected at other stations along the western segment of GA03 and showing large radionuclide anomalies also originated from a BNL. At station GT11-06, for example, $^{230}Th_d$ and $^{231}Pa_d$ activities show minima below 4000 m (Figs. A2 and A5), where a BNL is also found (Fig. 19).

The foregoing observations lead to the hypothesis that intensified scavenging of ^{230}Th and ^{231}Pa may occur in BNLs. The hypothesis is further suggested by a comparison of the horizontal distributions of PM concentration, ^{230}Th$_d$, and ^{231}Pa$_d$ in our reference solution. Particle concentrations show maxima in three main regions (Fig. 20): (i) along most of the continental slope and rise, (ii) the Sohm Abyssal Plain (Fig. 3), and (iii) the region between the New England Seamounts and Bermuda (Fig. 3).

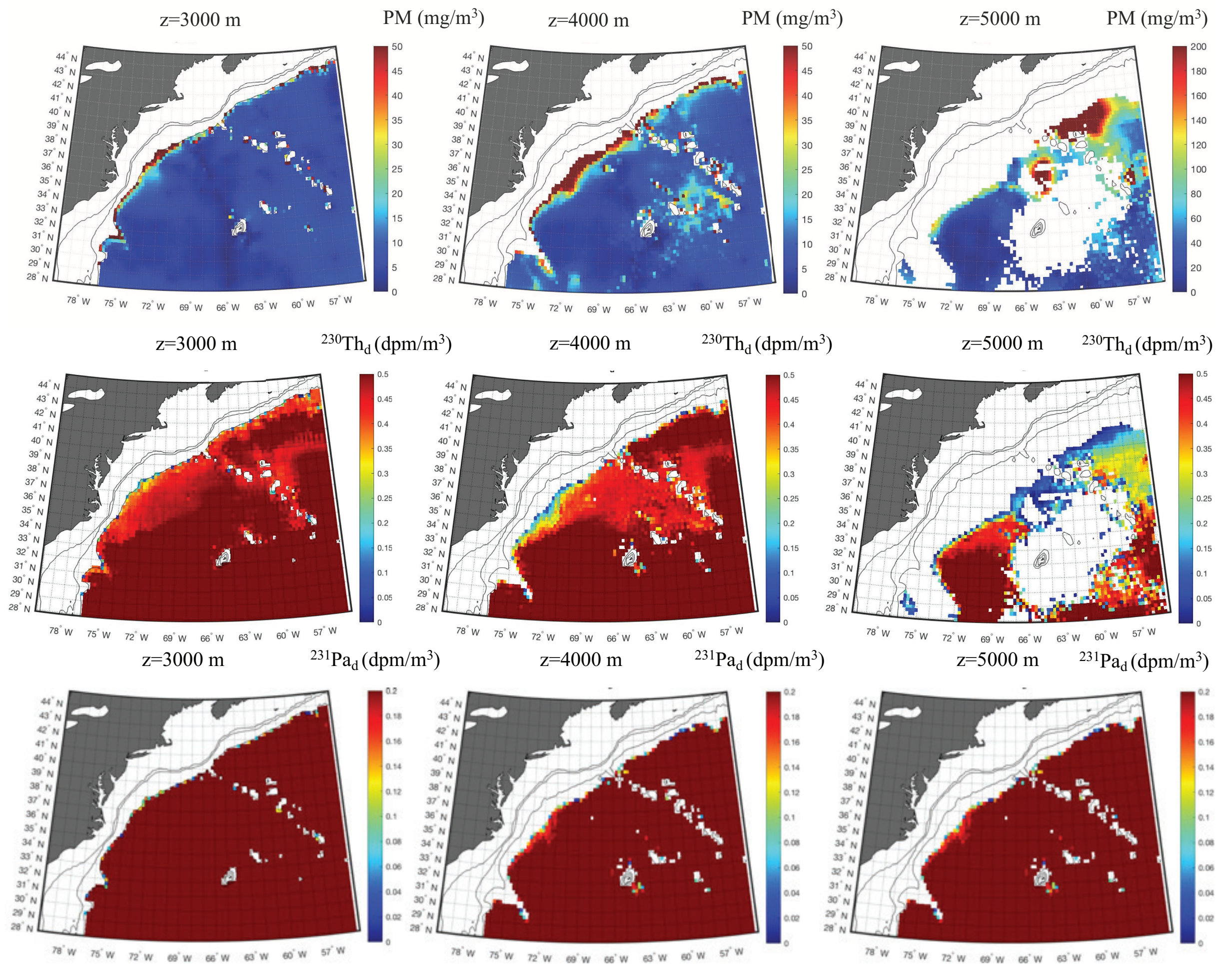

Fig. 20. Distributions of particulate matter concentration as estimated from optical measurements compiled by Gardner et al. (2017) (top three panels), ^{230}Th$_d$ activity as simulated in the reference solution (middle panels), and ^{231}Pa$_d$ activity as simulated in the reference solution (bottom panels). The left, middle, and right panels show distributions at a depth of, respectively, 3000 m, 4000 m, and 5000 m.

The simulated distributions of ^{230}Th$_d$ and ^{231}Pa$_d$ show minima in each of these regions (Fig. 20), suggesting that the pattern of particle scavenging at least partly influences the distribution of both radionuclides. Notice that regions of PM maxima and regions of (^{230}Th$_d$,^{231}Pa$_d$) minima do not strictly coincide. For example, ^{230}Th and ^{231}Pa could be removed from solution in a region where PM levels are high and the resulting (^{230}Th$_d$,^{231}Pa$_d$) anomalies could be advected into a region where PM levels are lower, leading to ^{230}Th$_d$ and ^{231}Pa$_d$ minima there.

Evidence for an influence of BNLs on the cycling of particle-reactive elements in the deep water column has been reported in a number of studies, namely through the observed disequilibrium of ^{234}Th (half-life of 24.1 days) with its radioactive parent, ^{238}U (e.g., Bacon and Rutgers van der Loeff (1989); Turnewitsch and Springer (2001); Rutgers van der Loeff et al. (2002)). Using a model that describes the vertical distribution of ^{234}Th near the seabed, Rutgers van der Loeff and Boudreau (1997) showed that the depletion of ^{234}Th in bottom waters can be linked to the distribution of excess ^{234}Th in surface sediments and on resuspended particles. Recently, BNLs have been mapped using 6,392 full-depth profiles made during 64 cruises using transmissometers mounted on CTD in several programs including WOCE, SAVE, JGOFS, CLIVAR-Repeat Hydrography, and GO-SHIP over the last four decades (Gardner et al. 2018a). In addition to the western North Atlantic, areas of intense BNLs have been found in the Argentine Basin, the Southern Ocean, and the oceanic region around South Africa (see also Gardner et al. (2018b)). Future studies will need to establish the global significance of BNLs for the ocean biogeochemical cycles of ^{230}Th and ^{231}Pa and of adsorption-prone elements in general.

d. Temporal Variations of Particle Scavenging in the Deep Sea

The possibility that ^{230}Th and ^{231}Pa removal from solution can be enhanced in BNLs suggests that the scavenging of both nuclides may show significant temporal variations in the deep water column. Benthic nepheloid layers generally have a basal uniform region corresponding closely to the bottom mixed layer (typically 20–100 m thick) and an overlying region (typically 500–2000 m thick) where light scattering (or attenuation) falls off more or less logarithmically up to a clear water minimum (McCave 1986). The particulate material in each region is thought to originate from sediment resuspension followed by some combination of vertical turbulent mixing and lateral transport (McCave 1986). None of these processes are expected to be time-invariant, suggesting that the amount and distribution of particles within BNLs may both be variable.

Dramatic evidence for the transient nature of BNLs in the western North Atlantic has been provided by a number of studies, most notably through the HEBBLE experiment on the Nova Scotian continental rise (HEBBLE 1988). Previous studies had established that intense BNLs in the western North Atlantic tend to form during episodes of strong abyssal currents and sediment resuspension, which have been pictorially referred to as 'benthic storms' (Gardner and Sullivan 1981). Results from HEBBLE showed that fast currents, high concentrations of suspended sediment, and grooved mud beds are associated with erosion in frequent benthic storms (Hollister and McCave 1984). More recently, measurements of deep-sea currents, nephelometer-based particle concentration, and seafloor photographs gathered during science programs that spanned two decades in the western North Atlantic have been synthesized (Gardner et al. 2017). These authors concluded that benthic storms occurred in areas with high surface eddy kinetic energy, most frequently beneath the meandering Gulf Stream and its associated rings.

Different mechanisms have been proposed to explain benthic storms, including (i) synoptic atmospheric events such as nor'easters, tropical storms, or hurricanes (Gardner and Sullivan 1981); and (ii) oceanic features generated from the Gulf Stream such as deep cyclones and topographic Rossby waves (Gardner et al. 2017). In this regard, it is instructive to consult the cruise report for the second leg of GA03 for information about weather conditions encountered during the leg (GA03 Shipboard Team 2016). After station GT11-04, where a very strong BNL was found (Fig. 19), weather conditions deteriorated, with a hurricane passing between the ship's position and Bermuda, followed by three more days of sustained winds > 25 knots. At station GT11-06, a very strong BNL was observed, detectable below 4200 m but most strongly expressed below 4400 m (GA03 Shipboard Team (2016); Fig. 19). The BNL at GT11-08 was even stronger (Fig. 19). Speculatively, the difficulty to simulate accurately radionuclide profiles at individual stations whilst the station-averaged profiles can be better reproduced (section 4.b) may be due to pronounced temporal variations in PM load and scavenging intensity at abyssal depths. Further work is needed to assess whether the strong BNLs observed at stations occupied along the western segment of GA03 and showing large radionuclide anomalies near the bottom were related to the adverse weather conditions experienced during the cruise.

e. Use of ^{230}Th as a Ventilation Tracer

A few studies suggested that the low ^{230}Th and ^{231}Pa observed in the deep Atlantic compared to values expected from reversible exchange could be explained by deep ventilation through lateral advection and mixing (Moran et al. 1997; Vogler et al. 1998; Moran et al. 2002). These studies applied a model originally developed to interpret ^{230}Th data from the Weddell Sea in terms of upwelling of lower Circumpolar Deep Water (Rutgers van der Loeff and Berger 1993). In this 'mixing-scavenging' model, the equations for reversible exchange are extended to include a term that is intended to represent the additional influence of a source water,

$$w_p \frac{\partial A_p}{\partial z} = \lambda A_\pi + \frac{A_* - A_{tot}}{\tau}, \tag{6}$$

where $A_{tot} = A_d + A_p$ is the total activity, A_* is the total activity of the source water, and τ is a time scale for water renewal. An analytical solution of (6) can be easily derived for uniform w_p, A_*, and τ, and fit to activity data to obtain an estimate of τ. From this approach, water renewal times from 3 to 140 yr have been reported, where the range reflects (i) estimates from different locations in the Atlantic Ocean and (ii) uncertainties associated with the variability of activity data from a single station (Moran et al. 1997; Vogler et al. 1998; Moran et al. 2002).

Albeit instructive, the model (6) is not free of limitations. The effect of advection is represented in a crude manner and solutions obtained with uniform A_* and τ assume that A_{tot} is influenced by the same source water introduced at the same rate throughout the water column. More recently, an attempt to extract information about deep North Atlantic circulation from ^{230}Th data has been undertaken using an inverse finite-difference geostrophic model (Marchal et al. 2007). These authors found that the addition of ^{230}Th data to density and transport observations in the inversion leads to zonally integrated meridional transports below 1000 m which have larger amplitudes (by 2–9 Sv), where the range reflects the uncertainties in the large-scale ^{230}Th distribution and in the ^{230}Th balance equation.

The results reported in this paper, however, suggest that caution should be exercised when interpreting ^{230}Th and ^{231}Pa measurements from the western North Atlantic in terms of deep water ventilation, at least in terms of ventilation from the DWBC. According to these results, the distributions of ^{230}Th and ^{231}Pa in the western North Atlantic show on average only modest variations in response to a change by a factor of four in the strength of the DWBC (10 to 40 Sv) along 55°W (Fig. 15). Other factors, such as particle scavenging and the ^{230}Th and ^{231}Pa activities in the inflowing waters, are shown here to have a larger influence on the radionuclide distributions west of the MAR. This latter finding is consistent with a recent study by Deng et al. (2018), who found, using the 'mixing-scavenging model', that the ^{230}Th and ^{231}Pa activities of the water entering a deep basin significantly influence the ^{230}Th and ^{231}Pa activities within the basin.

It is instructive to compare, for the reference solution, the residence time of the water in the domain with respect to the DWBC inflow with the residence of both radionuclides with respect to scavenging. The water residence time is computed from

$$\tau_{wat} = \frac{\iiint \, dx\,dy\,dz}{\iint u_n(x_{\mathrm{DWBC}}, y, z) dy\,dz}, \tag{7}$$

where $u_n(x_{\mathrm{DWBC}}, y, z)$ is the zonal (westward) velocity at the DWBC inflow location. The triple integral in the numerator is over the entire volume of the domain and the double integral in the denumenator is over the surface area of the DWBC inflow.

We find a value $\tau_{wat} = 21.0$ yr, of the same order of magnitude as the water renewal times estimated from tritium and excess He-3 data (Doney and Jenkins 1994) and from CFC data (Rhein et al. 2015). On the other hand, we consider three different definitions of residence time for scavenging. First, we calculate the scavenging residence time as

$$\tau_{scav,1} = \frac{\iiint A_{tot}(x,y,z)\,dx\,dy\,dz}{\iint \lambda A_\pi \,dx\,dy\,dz}, \tag{8}$$

where A_{tot} is the total activity defined above. We find that $\tau_{scav,1} = 19$ yr for ^{230}Th and 91 yr for ^{231}Pa, consistent with the estimates for the whole Atlantic Ocean of, respectively, 26 yr and 111 yr, based on the same definition and reported by Yu et al. (1996). Although the above definition of residence time is convenient, it does rely on the assumption that the radionuclide balance in the water column is dominated by radioactive production and particle scavenging (Broecker and Peng 1982). We thus consider another definition,

$$\tau_{scav,2} = \frac{\iiint A_{tot}(x,y,z)\, dx\, dy\, dz}{\iint w_p A_{p,bot}\, dx\, dy}, \tag{9}$$

where $A_{p,bot}$ is the activity of the radionuclide in the particulate phase just above the seafloor. The time scale as defined above could be regarded as a residence time with respect to the flux of particulate radionuclide to the seabed. We find that $\tau_{scav,2}$ amounts to 8 yr for ^{230}Th and 32 yr for ^{231}Pa, consistent with the notion that Th is more sensitive to particles than Pa but noticeably smaller than the values of $\tau_{scav,1}$. Finally, we consider a third definition,

$$\tau_{scav,3} = \frac{\iiint A_d(x,y,z)\, dx\, dy\, dz}{\iiint k_1(x,y,z) A_d(x,y,z)\, dx\, dy\, dz}, \tag{10}$$

where A_d is the radionuclide activity in the dissolved phase and k_1 is the adsorption rate constant as defined in section 2.3. This other time scale could be viewed as a residence time with respect to adsorption. Unlike $\tau_{scav,1}$ but similarly to $\tau_{scav,2}$, it has the virtue that a specific removal process is identified in its definition. We find that $\tau_{scav,3}$ amounts to 2 yr for ^{230}Th and 4 yr for ^{231}Pa, again consistent with the greater particle sensitivity of Th but even smaller than the values of $\tau_{scav,1}$.

A comparison of the values of τ_{wat} with those of ($\tau_{scav,2}$,$\tau_{scav,3}$) shows that ^{230}Th is in general more rapidly removed by adsorption onto particles and by particle settling to the seafloor than it is transported by the DWBC. On the other hand, τ_{wat} is smaller than $\tau_{scav,2}$ for ^{231}Pa, suggesting that the transport of ^{231}Pa is at least as important as its removal to sediments.

7. Summary and Perspectives

In this study, we have first examined the extent to which a regional ocean circulation model with 1/4° resolution and including a description of particle scavenging based on optically-derived particle concentration data can reproduce the circulation and the distributions of ^{230}Th and ^{231}Pa in the western North Atlantic. We found that some, though not all, elements of the general circulation and of the radionuclide distributions which are observed in the area can be reproduced. The model simulates a Gulf Stream displaying some degree of variability (e.g., meandering), a Deep Western Boundary Current along the continental slope and rise, and key features in the $^{230}\mathrm{Th}_{d,p}$ and $^{231}\mathrm{Pa}_{d,p}$ distributions observed during (pre-)GEOTRACES cruises, such as a reversal of the vertical $^{230}\mathrm{Th}_d$ and $^{231}\mathrm{Pa}_d$ gradients at mid-depth. On the other hand, the simulations presented in this paper differ in several respects from observations, e.g., the Gulf Stream separates from the western margin farther north than observed, the velocity maxima in the Gulf Stream (DWBC) are underestimated (overestimated) and occur too far to the northwest along line W, and the low $^{231}\mathrm{Pa}_d$ activities observed in deep water are overpredicted.

The model has then been applied to investigate the influences of particle scavenging and of DWBC inflow properties (strength and radionuclide contents) on the ^{230}Th and ^{231}Pa distributions in the western North Atlantic. We found that the vertical distributions of $^{230}\mathrm{Th}_{d,p}$ and $^{231}\mathrm{Pa}_{d,p}$ averaged for all (pre-)GEOTRACES stations are more sensitive to particle scavenging than they are to the strength of the DWBC inflow. This result suggests that the distribution of particulate matter concentration, with (relative) maxima in benthic nepheloid layers, is more important than the strength of deep water ventilation in setting the basin-mean vertical distributions of both radionuclides in the study area. We also found that changes in the radionuclide activities of the DWBC inflow are more likely to produce variations in these distributions than changes in the strength of the DWBC inflow. A model solution with uniform rate constants of Th and Pa adsorption, with no enhancement in deep water, was unable to explain the observed inversion in $^{230}\mathrm{Th}_d$ and $^{231}\mathrm{Pa}_d$ profiles at mid-depth. Overall, these results suggest that the relatively low $^{230}\mathrm{Th}_d$ and $^{231}\mathrm{Pa}_d$ activities observed in deep waters in the western North Atlantic stem from intensified scavenging in thick, active benthic nepheloid layers rather than from ventilation by $^{230}\mathrm{Th}_d$- and $^{231}\mathrm{Pa}_d$-poor waters from the western boundary.

We clarify below what we perceive as being the main limitations of this study. Needless to say, the results reported in this paper are only as reliable as the model on which they are based. A number of factors could be responsible for the differences between model results and physical observations from satellite altimetry and repeat cruises along line W. These include, for instance, an inadequate horizontal resolution of the model, the surface forcing based on climatological fields of winds, temperature, and salinity, and the omission of shelf circulation. The factors responsible for the differences between the observed and modeled distributions of $^{230}\mathrm{Th}_{d,p}$ and $^{231}\mathrm{Pa}_{d,p}$ could be due to errors in both the physical and geochemical components of the model. Although the present model represents explicitly the kinetics of sorption reactions through a separate equation for the dissolved and particulate phases, the treatment of ^{230}Th and ^{231}Pa cycling in the ocean remains relatively crude. While optical measurements provide important constraints on particle distribution, temporal variations in particle concentration, which can be dramatic near the bottom (e.g., HEBBLE (1988)), are neglected in this study. While several light scattering time series from long-term nephelometer deployments indicate a strong positive correlation between the temporal standard deviation in near-bottom particle concentration and the eddy kinetic energy as derived from satellite altimetry, the temporal variability of particle concentration in the northwest Atlantic remains largely unknown.

Given the above caveats, a number of perspectives for future modeling efforts can be outlined. First, a model with higher resolution would be desirable in order to simulate the western North Atlantic circulation in more detail. With a horizontal resolution of $1/4°$, baroclinic eddies are allowed to grow but are only marginally resolved; to simulate the full dynamical and life cycle of baroclinic eddies, an 'eddy-resolving' model, perhaps with a horizontal resolution approaching $1/10°$, would be needed (Tréguier et al. 2014). Use of higher spatial resolution might also help (i) to better represent the separation of the Gulf Stream from the coast (Chassignet and Marshall 2008; Ezer 2016b) and (ii) to reduce the error in the evaluation of the horizontal pressure gradient (PG) in s-coordinate models. The error in the evaluation of the horizontal PG in s-coordinate models has been discussed at length in the literature (e.g., Shchepetkin and McWilliams (2003) and references therein; Ciappa (2008)). In POM, the initial density field area-averaged on z-levels and then transferred to s-coordinates is subtracted from the density field at each time step in an effort to reduce the truncation error associated with the calculation of the horizontal baroclinic PG (Mellor 2002). Theoretical analysis and numerical solutions obtained with POM have shown that velocity errors arising from the calculation of the horizontal PG vanish due to advection of the density field (Mellor et al. 1994), or do not vanish prognostically but are small, especially if a horizontally averaged density field is subtracted before computing the horizontal baroclinic PG (Mellor et al. 1998) as done in POM. Although these results appear encouraging, subtraction of a horizontally averaged density field may not yield particularly good results in a domain characterized by strong horizontal density gradients, such as the western North Atlantic, and represented with a coarse grid. Second, the model domain should be extended to include the continental shelf from Cape Hatteras to Nova Scotia. Consideration of the continental shelf would allow one to study the potential role of shelf-ocean exchange in the radionuclide distributions in the slope region where some of the ^{230}Th and ^{231}Pa data used in this study originate. Finally, a more detailed description of particle scavenging would permit more credible simulations of ^{230}Th and ^{231}Pa in the study area. The model could incorporate an explicit representation of sediment resuspension, transport, and deposition, and of the influence of the resuspended sediment on the removal of both radionuclides from the deep water column (e.g., Rutgers van der Loeff and Boudreau (1997)). The model could be extended to include (i) the effect of particle composition on the removal of both radioisotopes (e.g., Hayes et al. (2015a)), and (ii) more than one particle class so as to account for the processes of particle (dis)aggregation, particularly in BNLs (e.g., McCave (1985); Hill and Nowell (1990)).

Acknowledgments.

We are grateful to John Toole for sharing velocity data from line W, and to both him and Magdalena Andres for useful discussions. We thank Jerry McManus for directing us to a recent compilation of surface sediment $^{231}Pa/^{230}Th$ data. Detailed and constructive comments by two anonymous reviewers have allowed us to improve significantly the manuscript. This study could not have been possible without the dedication of researchers who collected samples at sea and generated the (pre-)GEOTRACES data analyzed in this study. This work has been supported by grant OCE-1556400 from the U.S. National Science Foundation.

APPENDIX A: Mapping of Particle Matter Concentration

This appendix describes the procedure used to map the distribution of particulate matter (PM) concentration from optical data in the western North Atlantic. For convenience, the particle concentration derived from optical data and vertically interpolated on a model level is called c_d below. The distributions of c_d along the different s-surfaces of the model (31 surfaces) are mapped individually. The mean of c_d for a given s-surface ($\bar{c}_d$ below) is computed and subtracted from the c_d values along the surface to yield PM anomalies, c'_d. The PM concentrations at the model grid points along the surface are then estimated from (i) the PM anomalies at the locations where optical data are available ('data locations' below) and (ii) the mean $\bar{c}_d$,

$$\hat{\mathbf{c}} = \mathbf{A}\mathbf{c}'_d + \mathbf{I}\bar{c}_d. \tag{A1}$$

Here $\hat{\mathbf{c}}$ is a vector including the PM estimates at the model grid points ($\mathbf{c}$ would include the true PM values at these points), $\mathbf{c}'_d$ is a vector including the PM anomalies at the data locations, and $\mathbf{I}$ is the identity matrix with order equal to the dimension of $\hat{\mathbf{c}}$. The matrix $\mathbf{A}$ is derived such that the PM estimates at the model grid points have minimum variance (e.g., Wunsch (2006)),

$$\mathbf{A} = \mathbf{R}_{cc_d}\left(\mathbf{R}_{c_dc_d} + \mathbf{R}_{ee}\right)^{-1}, \tag{A2}$$

where $\mathbf{R}_{cc_d}$ and $\mathbf{R}_{c_dc_d}$ are second-moment matrices for the PM field and $\mathbf{R}_{ee}$ is a second-moment matrix for the errors in the elements of $\mathbf{c}'_d$.

Consider first $\mathbf{R}_{cc_d}$ and $\mathbf{R}_{c_dc_d}$. These matrices are specifically defined as $\mathbf{R}_{cc_d} = E[\mathbf{c}\mathbf{c}_d^T]$ and $\mathbf{R}_{c_dc_d} = E[\mathbf{c}_d\mathbf{c}_d^T]$, where $E[\cdot]$ designates the expected value (mean) and ^{T} designates the transpose. The (i,j) element of $\mathbf{R}_{cc_d}$, noted $[\mathbf{R}_{cc_d}]_{i,j}$, is the covariance between the PM concentrations at model grid point location $\hat{\mathbf{r}}_i$ and data location $\mathbf{r}_j$. Similarly, the (i,j) element of $\mathbf{R}_{c_dc_d}$, noted $[\mathbf{R}_{c_dc_d}]_{i,j}$, is the covariance between the PM concentrations at data locations $\mathbf{r}_i$ and $\mathbf{r}_j$. The following assumptions are made about the spatial covariances of PM concentration,

$$[\mathbf{R}_{cc_d}]_{i,j} = \sigma^2 \exp\left(-\frac{|\hat{\mathbf{r}}_i - \mathbf{r}_j|}{L}\right) \qquad \text{and} \qquad [\mathbf{R}_{c_dc_d}]_{i,j} = \sigma^2 \exp\left(-\frac{|\mathbf{r}_i - \mathbf{r}_j|}{L}\right), \tag{A3}$$

where σ^2 is a PM variance, L is a length scale, and $|\cdot|$ denotes the geodesic distance (taking the geodesic distance instead of the actual distance along the s-surface should incur only a small error given the smallness of bathymetric slopes). Equations (A3) entail that the covariance between the PM concentrations at two different locations decreases exponentionally with distance between these locations, dropping to $0.37\sigma^2$ for a distance equal to L.

Consider then $\mathbf{R}_{ee} = E[\mathbf{e}\mathbf{e}^T]$, where $\mathbf{e}$ is the vector of errors in the elements of $\mathbf{c}'_d$. The diagonal elements of $\mathbf{R}_{ee}$ are the variances of the errors in the PM anomalies in $\mathbf{c}'_d$, and the off-diagonal elements of $\mathbf{R}_{ee}$ are the covariances between these errors. Here $\mathbf{R}_{ee}$ is taken as diagonal (no error covariances) and its diagonal elements are set equal to $\sigma_e^2 = (8.5 \text{ mg m}^{-3})^2$. This error variance is intended to account for the fact that, for many of the stations where transmissometry measurements were made, samples for PM were not collected, so the particle concentration in the water where the beam attenuation coefficient was minimum could not be identified. In fact, the minimum beam attenuation coefficient for particles for each cast was set to the cruise-average minimum taken as 0 m $^{-1}$ (Gardner et al. 2018b), which results in PM value of 0 mg m^{-3} using the calibration equation. Thus, there is an error associated with the unknown concentration of particles at the clear water minima. Since these minima typically exhibit particle concentrations between 5–12 mg m^{-3} in the western North Atlantic (Brewer et al. 1976; Gardner et al. 1985a), we use the median value of 8.5 mg m^{-3} as the uncertainty associated with the particle concentration in clear waters.

The mapping as described above implies that the mapped PM field becomes smoother as the length scale L increases, and that mapped PM values at grid points that are very distant ($\gg L$) from data locations approach the mean value $\bar{c}_d$. In this study, we choose L = 100 km for all s-surfaces and $\sigma^2 = \sigma_s^2$, where σ_s^2 is the variance of the PM field along the s-surface. With this choice, the mapped PM values at the data locations are generally consistent with the PM estimates at these locations, i.e., more than 0.4% of the mapped PM values are within $2\sigma_e$ of the PM estimates at the data locations (not shown).

APPENDIX B: Horizontal Boundary Conditions

This appendix describes the conditions imposed at the surface and at the bottom of the domain. Kinematic conditions are specified on the flow at the surface and at the bottom,

$$w = \frac{\partial \eta}{\partial t} + \mathbf{u}_h \cdot \nabla \eta \qquad \text{at } z = \eta(x, y, t), \tag{B1a}$$

$$w = -\mathbf{u}_h \cdot \nabla h \qquad \text{at } z = -h(x, y), \tag{B1b}$$

where $\mathbf{u}_h = (u, v)$ is the horizontal velocity, $\eta(x, y, t)$ is the free surface elevation, and $h(x, y)$ is the water depth. Annual mean wind stresses from SCOW (Risien and Chelton 2008), $\boldsymbol{\tau}_{\text{SCOW}}$, are prescribed at the surface and a shear stress $\boldsymbol{\tau}_b$ is imposed at the bottom:

$$\rho_o \kappa_m \frac{\partial \mathbf{u}_h}{\partial z} = \boldsymbol{\tau}_{\text{SCOW}} \qquad \text{at } z = \eta(x, y, t), \tag{B2a}$$

$$\rho_o \kappa_m \frac{\partial \mathbf{u}_h}{\partial z} = \boldsymbol{\tau}_b \qquad \text{at } z = -h(x, y). \tag{B2b}$$

Here ρ_o = 1025 kg m^{-3} is a reference density and κ_m is the (variable) vertical turbulent viscosity. The bottom stress is given by

$$\boldsymbol{\tau}_b = \rho_o C_d |\mathbf{u}_{h,b}| \mathbf{u}_{h,b}. \tag{B3}$$

In this expression, $\mathbf{u}_{h,b}$ is the horizontal velocity at the bottom (the grid point nearest to the bottom) and C_d is a drag coefficient computed from

$$C_d = \left(\frac{\kappa}{\ln\left[(1+s_b)\,h/z_r\right]} \right)^2, \tag{B4}$$

where $\kappa = 0.4$ is the von Kármán constant, $z_r = 0.01$ m is a bottom roughness parameter, and s_b is the s coordinate of the deepest level above the bottom (Mellor 2002). The C_d values over the whole domain are tested such that $0.0025 \le C_d \le 1$.

The turbulence variables at the surface and at the bottom are set as follows (Blumberg and Mellor 1987; Mellor 2002),

$$\left(q^2, q^2 l\right) = \left(b_1^{2/3} u_*^2, 0\right), \tag{B5}$$

where $b_1 = 16.6$ is an empirical constant and u_* is the friction velocity associated with the surface stress or the bottom stress as denoted.

Finally, fluxes of temperature and salinity at the surface are represented through a restoring to climatologic annual mean values from the World Ocean Atlas (Locarnini et al. 2013; Zweng et al. 2013), respectively, T_{WOA} and S_{WOA},

$$\kappa_{\mathcal{T}} \frac{\partial T}{\partial z} = \frac{\delta}{\tau}\left(T_{\mathrm{WOA}} - T\right), \tag{B6a}$$

$$\kappa_{\mathcal{T}} \frac{\partial S}{\partial z} = \frac{\delta}{\tau}\left(S_{\mathrm{WOA}} - S\right). \tag{B6b}$$

Here δ is the thickness of the surface layer and $\tau = 14.4$ days is a restoring time scale. A no-flux condition is specified for (A_d, A_p) at the surface and for (T, S, A_d, A_p) at the bottom.

APPENDIX C: Lateral Boundary conditions

Conditions on Velocities

The appendix describes the conditions applied at the lateral boundaries of the model domain. Conditions on both the horizontal velocities (internal mode) and their vertical averages (external mode) are needed. For convenience, the velocity component normal (tangent) to a lateral boundary is designated with subscript n (t), and the velocity averaged from the bottom to the surface is represented with an overbar. Thus, for example, u_n is the velocity normal to the boundary at a given depth and $\bar{u}_n$ is the vertically averaged velocity normal to the boundary. Different types of conditions are imposed along different segments of the lateral boundaries.

Segments with Inflows and Outflows

Deep Western Boundary Current The inflow of the DWBC is specified at the eastern boundary (55°W) along the segment between 42.5°–44.875°N. Conditions on both the distribution and the vertical average of (u_n, u_t) across the segment are specified. The distribution of (u_n, u_t) across the segment is set as follows,

$$\begin{aligned} u_n &= u_{\mathrm{i,DWBC}} \exp\left(-\left[\frac{y - y_{\mathrm{i,DWBC}}}{l_{y,\mathrm{DWBC}}}\right]^2\right) \exp\left(-\left[\frac{z - z_{\mathrm{i,DWBC}}}{l_{z,\mathrm{DWBC}}}\right]^2\right). && \text{(C1a)} \\ u_t &= 0. && \text{(C1b)} \end{aligned}$$

Here $y_{\mathrm{i,DWBC}}$ ($z_{\mathrm{i,DWBC}}$) is the meridional (vertical) coordinate of the core of the current and $l_{y,\mathrm{DWBC}}$ ($l_{z,\mathrm{DWBC}}$) is a length scale for the meridional (vertical) extent of the current. We assume a value of $y_{\mathrm{i,DWBC}}$ such that the core of the current is situated 120 km south of the northern boundary at 55°W, a value of 3500 m for $z_{\mathrm{i,DWBC}}$, a value of 50 km for $l_{y,\mathrm{DWBC}}$, and a value of 500 m for $l_{z,\mathrm{DWBC}}$. The zonal velocity $u_{\mathrm{i,DWBC}}$ is calculated such that the integral of u_n over the surface area of the segment is equivalent to a volume transport of 20 Sv (1 Sv = 10^6 m^3 s^{-1}). The above values assumed for $(y_{\mathrm{i,DWBC}}, z_{\mathrm{i,DWBC}}, l_{y,\mathrm{DWBC}}, l_{z,\mathrm{DWBC}})$ and for the volume transport are broadly consistent with observations made in the area (Pickart and Smethie 1998). The vertical average of u_n is prescribed through a radiation condition (Flather 1976), whereas the vertical average of u_t is set to zero,

$$\bar{u}_n = \bar{u}_{n,*} + \sqrt{\frac{g}{h}}\,(\eta - \eta_*) \qquad \text{and} \qquad \bar{u}_t = 0. \tag{C2}$$

Here $\bar{u}_{n,*}$ is the vertical average of the right-hand side of (C1a), h is the local water depth, η is the local free surface elevation simulated by the model, and η_* is a value calculated geostrophically from $\bar{u}_{n,*}$.

The outflow of the DWBC is specified at the southern boundary (28°N) along the segment between 75.5°–76.5°W. The condition (C1a) for the normal velocity is replaced by a radiation condition, and the velocity tangent to the boundary is set to zero:

$$\frac{\partial u_n}{\partial t} - c_i \frac{\partial u_n}{\partial n} = 0 \qquad \text{and} \qquad u_t = 0. \tag{C3}$$

Here n is the coordinate normal to the boundary and $c_i > 0$ is a speed for the internal mode, derived from the water depth at the boundary and a maximum depth, $h_{\max}$ (Mellor 2002). The differential equation (C3) is discretized with an upstream scheme, which implies that meridional momentum is always advected southwards (out of the domain) at the boundary. The vertical averages of (u_n, u_t) are specified as follows. The distribution of u_n along the segment is first taken as

$$u_n = u_{\mathrm{o,DWBC}} \exp\left(-\left[\frac{z - z_{\mathrm{o,DWBC}}}{l_{z,\mathrm{DWBC}}}\right]^2\right). \tag{C4}$$

where $z_{\mathrm{o,DWBC}} = 3000$ m is the depth of the core of the current and $l_{z,\mathrm{DWBC}} = 500$ m. The meridional velocity $u_{\mathrm{o,DWBC}}$ is determined such that the integral of u_n over the surface area of the segment is equivalent to a volume transport of 20 Sv, which is the volume transport set at the inflow location. The vertical averages of (u_n, u_t) are then prescribed similarly to (C2),

$$\bar{u}_n = \bar{u}_{n,*} - \sqrt{\frac{g}{h}}\,(\eta - \eta_*) \qquad \text{and} \qquad \bar{u}_t = 0, \tag{C5}$$

where $\bar{u}_{n,*}$ is the vertical average of the right-hand side of (C4) and η_* is determined geostrophically from $\bar{u}_{n,*}$.

Gulf Stream The inflow of the Gulf Stream (GS), intended to represent the Florida Current, is applied at the southern boundary along the segment between 78°–80°W. In contrast to the DWBC inflow, only the vertical averages of (u_n, u_t) are specified. Conditions identical to (C3) are prescribed for (u_n, u_t). The vertical averages of (u_n, u_t) are prescribed as follows. The distribution of u_n along the segment is first taken as

$$u_n = u_{\mathrm{i,GS}} \exp\left(-\left[\frac{z}{l_{z,\mathrm{GS}}}\right]^2\right). \tag{C6}$$

where $l_{z,\mathrm{GS}} = 200$ m. The meridional velocity $u_{\mathrm{i,GS}}$ is calculated such that the integral of u_n over the surface area of the segment is equivalent to a volume transport of 30 Sv. This value is consistent with the long-term mean transport of the Florida Current of about 32 Sv measured from daily cable observations and shipboard sections across the Straits of Florida (Baringer and Larsen 2001; Meinen et al. 2010). The vertical averages of (u_n, u_t) are then prescribed using conditions identical to (C5).

The outflow of the GS is applied at the eastern boundary along the segment between 39°–41°N. A radiation condition is used for u_n whilst u_t is taken to vanish along the segment:

$$\frac{\partial u_n}{\partial t} + c_i \frac{\partial u_n}{\partial n} = 0 \qquad \text{and} \qquad u_t = 0. \tag{C7}$$

As for (C7), the differential equation (C7) is approximated with an upstream scheme, so that zonal momentum is always advected eastwards (out of the domain) at the boundary. The vertical averages of (u_n, u_t) are specified as follows. The distribution of u_n along the segment is first taken as

$$u_n = u_{\mathrm{o,GS}} \exp\left(-\left[\frac{z}{l_{z,\mathrm{GS}}}\right]^2\right), \tag{C8}$$

where again $l_{z,\mathrm{GS}} = 200$ m. The zonal velocity $u_{\mathrm{o,GS}}$ is computed such that the integral of u_n over the surface area of the segment is equivalent to a volume transport of 90 Sv, a value compatible with mooring-based estimates of the time-mean GS transport of 93 Sv at 55°W (Hogg 1992) and 88 Sv at 68°W (Johns et al. 1995). The vertical averages of (u_n, u_t) are then prescribed using conditions identical to (C2).

Sargasso Sea The inflow of Sargasso Sea water (SSW) is applied at the eastern boundary along the segment between 28°–39°N. In contrast to the DWBC inflow and similarly to the GS inflow, only the vertical averages of (u_n, u_t) are specified. Conditions identical to (C7) are prescribed. The vertical averages of (u_n, u_t) are specified as follows. The distribution of u_n across the segment is first taken as

$$u_n = u_{\mathrm{i,SSW}} \exp\left(-\left[\frac{z}{l_{z,\mathrm{SSW}}}\right]^2\right), \tag{C9}$$

where $l_{z,\mathrm{SSW}} = 1000$ m. The zonal velocity $u_{\mathrm{i,SSW}}$ is computed such that the integral of u_n over the surface area of the segment is equivalent to a volume transport of 60 Sv, which is the difference between the GS outflow (90 Sv) and GS inflow (30 Sv). Accordingly, the net inflow (or outflow) of water vanishes at the lateral boundaries of the domain. The vertical averages of (u_n, u_t) are then prescribed using conditions identical to (C2). No outflow condition is applied for SSW.

Other Segments

Along segments where no inflow or outflow is prescribed, conditions (C3) or (C7) are applied for (u_n, u_t) and conditions (C2) or (C5) are applied for $(\bar{u}_n, \bar{u}_t)$.

Conditions on $T, S, A_d, A_p, q^2/2, q^2 l$

The following radiation condition is imposed at all lateral boundaries,

$$\frac{\partial \mathcal{T}}{\partial t} \pm u_n \frac{\partial \mathcal{T}}{\partial n} = 0, \tag{C10}$$

where $\mathcal{T} \in \{T, S, A_d, A_p, q^2/2, q^2 l\}$. As for (C3) and (C7), the differential equation (C10) is discretized with an upstream scheme. The variable $\mathcal{T}$ is advected out of the domain if the boundary velocity (with normal component u_n) is directed outwards, and it is advected into the domain if the boundary velocity is directed inwards. Thus, boundary values of $\mathcal{T}$ must be prescribed for the case where the boundary velocity is directly inwards. Boundary values of (T, S) are derived from the World Ocean Atlas (Locarnini et al. 2013; Zweng et al. 2013) (section 2.a). The radionuclide activities (A_d, A_p) are set to different values at different locations along the open boundaries. At the location of DWBC inflow (between 42.5°–44.875°N along 55°W), $^{230}\mathrm{Th}_d$ ($^{230}\mathrm{Th}_p$) is set to 0.4 dpm m^{-3} (0.03 dpm m^{-3}) and $^{231}\mathrm{Pa}_d$ ($^{231}\mathrm{Pa}_p$) is set to 0.22 dpm m^{-3} (0.003 dpm m^{-3}). These values are the average activities below 1000 m in the Labrador Sea as reported by Moran et al. (2002)), except for $^{231}\mathrm{Pa}_d$ whose boundary value is set to double this average activity. We found that this increase in $^{231}\mathrm{Pa}_d$ at the DWBC inflow produces a better fit to the observed radionuclide activities in the western North Atlantic. At all other locations, values of (A_d, A_p) are set according to idealized profiles that broadly reproduce measured profiles at station GT11-14 (27.58°N, 49.63°W) situated to the east of the domain,

$$A_d = A_{d,o}\left(1 - e^{z/l_z}\right) \text{ and } A_p = A_{p,o}\left(1 - e^{z/l_z}\right), \tag{C11}$$

where the length scales $l_z = 1600$ m for ^{230}Th and $l_z = 1132$ m for ^{231}Pa. Note that $z \leq 0$ in this study, which implies that A_d and A_p as calculated from (C11) increase monotonically with depth (Fig. A7). Finally, the boundary values of $(q^2/2, q^2 l)$ are set to small values.

APPENDIX D: ^{230}Th and ^{231}Pa Profiles at Individual Stations

This appendix illustrates observed and simulated profiles of $^{230}\mathrm{Th}_{d,p}$ and $^{231}\mathrm{Pa}_{d,p}$ at individual (pre-)GEOTRACES stations (Figs. A1–A13).

REFERENCES

Anderson, R. F., M. P. Bacon, and P. G. Brewer, 1983a: Removal of ^{230}Th and ^{231}Pa at ocean margins. *Earth Planet. Sci. Lett.*, **66**, 73–90.

Anderson, R. F., M. P. Bacon, and P. G. Brewer, 1983b: Removal of ^{230}Th and ^{231}Pa from the open ocean. *Earth Planet. Sci. Lett.*, **62**, 7–23.

Anderson, R. F., M. Q. Fleisher, P. E. Biscaye, N. Kumar, B. Dittrich, P. Kubik, and M. Suter, 1994: Anomalous boundary scavenging in the Middle Atlantic Bight: Evidence from ^{230}Th, ^{231}Pa, ^{10}Be and ^{210}Pb. *Deep Sea Res.*, **41**, 537–561.

Andres, M., J. Toole, D. Torres, W. Smethie, T. Joyce, and R. Curry, 2016: Stirring by deep cyclones and the evolution of Denmark Strait Overflow Water observed at line W. *Deep Sea Res. I*, **109**, 10–26.

Armstrong, R. A., C. Lee, J. I. Hedges, S. Honjo., and S. G. Wakeham, 2001: A new, mechanistic model for organic carbon fluxes in the ocean based on the quantitative association of poc with ballast minerals. *Deep Sea Res. I*, **49**, 219–236.

Bacon, M. P., 1984: Glacial to interglacial changes in carbonate and clay sedimentation in the Atlantic Ocean estimated from ^{230}Th measurements. *Isotope Geoscience*, **2**, 97–111.

Bacon, M. P. and R. F. Anderson, 1982: Distribution of thorium isotopes between dissolved and particulate forms in the deep sea. *J. Geophys. Res.*, **87**, 2045–2056.

Bacon, M. P. and M. M. Rutgers van der Loeff, 1989: Removal of thorium-234 by scavenging in the bottom nepheloid layer of the ocean. *Earth Planet. Sci. Lett.*, **92**, 157–164.

Baringer, M. and J. Larsen, 2001: Sixteen years of Florida Current transport at 27°N. *Geophys. Res. Let.*, **28**, 3179–3182.

Biscaye, P. E. and S. L. Eittreim, 1977: Suspended particulate loads and transports in the nepheloid layers of the abyssal Atlantic Ocean. *Mar. Geol.*, **23**, 155–172.

Blumberg, A. and G. Mellor, 1987: A description of a three-dimensional coastal ocean circulation model. *Three-dimensional coastal ocean models*, N. Heaps, Ed., Am. Geophys. Union, Geophysical Monograph, Vol. 4, 1–16.

Boss, E., W. Slade, M. Behrenfeld, and G. Dall'Olmo, 2009: Acceptance angle effects on the beam attenuation in the ocean. *Optics Express*, **17**, 1535–1550.

Bower, A. S. and H. D. Hunt, 2000a: Lagrangian observations of the Deep Western Boundary Current in the North Atlantic Ocean. Part I: Large-scale pathways and spreading rates. *J. Phys. Oceanogr.*, **30**, 764–783.

Bower, A. S. and H. D. Hunt, 2000b: Lagrangian observations of the Deep Western Boundary Current in the North Atlantic Ocean. Part II: The Gulf Stream- Deep Western Boundary Current crossover. *J. Phys. Oceanogr.*, **30**, 784–804.

Brewer, P. G., D. W. Spencer, P. E. Biscaye, A. Hanley, P. L. Sachs, C. L. Smith, S. Kadar, and J. Fredericks, 1976: The distribution of particulate matter in the Atlantic Ocean. *Earth Planet. Sci. Lett.*, **32**, 393–402.

Broecker, W. S. and T.-H. Peng, 1982: *Tracers in the Sea*. Lahmont Doherty Earth Obsevatory, New York, 171 pp.

Burke, A., O. Marchal, L. I. Bradtmiller, J. F. McManus, and R. François, 2011: Application of an inverse method to interpret ^{231}Pa/^{230}Th observations from marine sediments. *Paleoceanography*, **26**, PA1212,doi:10.1029/2010PA002 022.

Chase, Z., R. F. Anderson, M. Q. Fleisher, and P. W. Kubik, 2002: The influence of particle composition and particle flux on the scavenging of Th, Pa and Be in the ocean. *Earth Planet. Sci. Lett.*, **204**, 215–229.

Chassignet, E. and D. Marshall, 2008: Gulf Stream separation in numerical ocean models. *Ocean Modeling in an Eddying Eegime*, M. Hecht and H. Hasumi, Eds., Am. Geophys. Union, Geophysical Monograph, Vol. 177, 39–61.

Cheng, H., et al., 2013: Improvements in ^{230}Th dating, ^{230}Th and ^{234}U half-life values, and U-Th isotopic measurements by multi-collector inductively coupled plasma mass spectrometry. *Earth Planet. Sci. Lett.*, **371-372**, 82–91.

Chuang, C.-Y., P. Santschi, Y.-F. Ho, M. Conte, L. Guo, D. Schumann, M. Ayranov, and Y.-H. Li, 2013: Role of biopolymers as major carrier phases of Th, Pa, Pb, Po, and Be radionuclides in settling particles from the Atlantic Ocean. *Mar. Chem.*, **157**, 131–143.

Churchill, J. and G. Gawarkiewicz, 2009: Shelfbreak frontal eddies over the continental slope north of Cape Hatteras. *J. Geophys. Res.*, **114**, C02 017, doi:10.1029/2007JC004 642.

Ciappa, A. C., 2008: A method for reducing pressure gradient errors improving the sigma coordinate stretching function: An idealized flow patterned after the Libyan near-shore region with the POM. *Ocean Modelling*, **23**, 59–72.

Cochran, J. K., H. D. Livingston, D. J. Hirschberg, and L. D. Surprenant, 1987: Natural and anthropogenic radionuclide distributions in the northwestern Atlantic Ocean. *Earth Planet. Sci. Lett.*, **84**, 135–152.

Deng, F., G. Henderson, M. Castrillejo, F. Perez, and R. Steinfeld, 2018: Evolution of ^{231}Pa and ^{230}Th in overflow waters of the North Atlantic. *Biogeosciences*, **15**, 7299–7313.

Doney, S. C. and W. J. Jenkins, 1994: Ventilation of the deep western boundary current and abyssal western North Atlantic: Estimates from tritium and ^{3}He distributions. *J. Phys. Oceanogr.*, **24**, 638–659.

Dutay, J.-C., F. Lacan, M. Roy-Barman, and L. Bopp, 2009: Influence of particle size and type on ^{231}Pa and ^{230}Th simulation with a global coupled biogeochemical-ocean general circulation model: A first approach. *Geochem. Geophys. Geosys.*, **10**, doi: 10.1029/2008GC002 291.

Eittreim, S., M. Ewing, and E. Thorndike, 1969: Suspended matter along the continental margin of the North American Basin. *Deep Sea Res.*, **16**, 613–624.

Eittreim, S., E. Thorndike, and L. Sullivan, 1976: Turbidity distribution in the Atlantic Ocean. *Deep Sea Res.*, **23**, 1115–1127.

ETOPO2v2, 2006: Two-minute gridded global relief data. National Centers for Environmental Information, NOAA.

Ezer, T., 2016a: Can the Gulf Stream induce coherent short-term fluctuations in sea level along the US east coast? A modelling study. *Ocean Dynamics*, **66**, 207–220.

Ezer, T., 2016b: Revisiting the problem of the Gulf Stream separation: On the representation of topography in ocean models with different types of vertical grids. *Ocean Modelling*, **104**, 15–27.

Flather, R., 1976: A tidal model of the northwest european continental shelf. *Mémoires de la Soc. Royale des Sciences de Liège*, **6**, 141–164.

GA03 Shipboard Team, 2016: Cruise report for Knorr 204-01 (november 6 - december 11, 2011). Th U.S. GEOTRACES North Atlantic Transect - 2011 Shipboard Team.

Gardner, W., P. Biscaye, J. Zaneveld, and M. J. Richardson, 1985a: Calibration and comparison of the LDGO nephelometer and the OSU transmissometer on the Nova Scotia Rise. *Mar. Geol.*, **66**, 323–344.

Gardner, W., M. J. Richardson, and A. Mishonov, 2018a: Global assessment of benthic nepheloid layers and linkage with upper ocean dynamics. *Earth Planet. Sci. Lett.*, **482**, 126–134.

Gardner, W., M. J. Richardson, A. Mishonov, and P. Biscaye, 2018b: Global comparison of benthic nepheloid layers based on 52 years of nephelometer and transmissometer measurements. *Prog. Oceanogr.*, **168**, 100–111.

Gardner, W., J. Southard, and C. Hollister, 1985b: Sedimentation, resuspension and chemistry of particles in the northwest Atlantic. *Mar. Geol.*, **65**, 199–242.

Gardner, W. and L. Sullivan, 1981: Benthic storms: Temporal variability in a deep-ocean nepheloid layer. *Science*, **213**, 329–331.

Gardner, W., B. Tucholke, M. J. Richardson, and P. Biscaye, 2017: Benthic storms, nepheloid layers, and linkage with upper ocean dynamics in the western North Atlantic. *Mar. Geol.*, **385**, 304–327.

Garvine, R., K.-C. Wong, G. Gawarkiewicz, R. McCarthy, R. Houghton, and F. Aikman, 1988: The morphology of shelfbreak eddies. *J. Geophys. Res.*, **93**, 15,593–15,607.

Gawarkiewicz, G., K. Brink, F. Bahr, R. Beardsley, M. Caruso, J. Lynch, and C.-S. Chiu, 2004: A large amplitude meander of the shelfbreak front during summer south of New England: Observations from the shelfbreak PRIMER experiment. *J. Geophys. Res.*, **doi:10.1029/2002JC001468**.

Geibert, W. and R. Usbeck, 2004: Adsorption of thorium and protactinium onto different particle types: Experimental findings. *Geochim. Cosmochim. Acta*, **68**, 1489–1501.

Gu, S. and Z. Liu, 2017: ^{231}Pa and ^{230}Th in the ocean model of the Community Earth System Model (CESM1.3). *Geosci. Model Dev.*, **10**, 4723–4742.

Guo, L., H. Santschi, and M. Baskaran, 1997: Interactions of thorium isotopes with colloidal organic matter in oceanic environments. *Colloids and Surfaces*, **120**, 255–271.

Guo, L., H. Santschi, M. Baskaran, and A. Zindler, 1995: Distribution of dissolved and particulate ^{230}Th and ^{232}Th in seawater from the Gulf of Mexico and off Cape Hatteras as measured by SIMS. *Earth Planet. Sci. Lett.*, **133**, 117–128.

Hayes, C., et al., 2015a: ^{230}Th and ^{231}Pa on GEOTRACES GA03, the US GEOTRACES North Atlantic transect, and implications for modern and paleoceanographic chemical fluxes. *Deep Sea Res. II*, **116**, 29–41.

Hayes, C., et al., 2015b: Intensity of Th and Pa scavenging partitioned by particle chemistry in the North Atlantic Ocean. *Mar. Chem.*, **170**, 49–60.

HEBBLE, 1988: *Deep Ocean Sediment Transport - High Energy Benthic Boundary Layer Experiment: Collected reprints of Office of Naval Research Funded Studies*, I. McCave, C. Hollister, and A. Nowell, Eds., Woods Hole Oceanographic Institution, 42 pp.

Henderson, G. M. and R. F. Anderson, 2003: The U-series toolbox for paleoceanography. *Rev. Mineral. Geochem.*, **52**, 493–531.

Henderson, G. M., C. Heinze, R. F. Anderson, and A. M. E. Winguth, 1999: Global distribution of the ^{230}Th flux to ocean sediments constrained by GCM modelling. *Deep Sea Res. I*, **46**, 1861–1893.

Henry, L. G., J. F. McManus, W. B. Curry, N. L. Roberts, A. M. Piotrowski, and L. D. Keigwin, 2016: North Atlantic ocean circulation and abrupt climate change during the last glaciation. *Science*, **353**, 470–474.

Hill, P. and A. Nowell, 1990: The potential role of large, fast-sinking particles in clearing nepheloid layers. *Phil. Trans. Roy. Soc., London A*, **331**, 103–107.

Hogg, N. G., 1992: On the transport of the Gulf Stream between Cape Hatteras and the Grand Banks. *Deep Sea Res.*, **39**, 1231–1246.

Hogg, N. G., R. S. Pickart, R. M. Hendry, and W. J. Smethie, 1986: The Northern Recirculation Gyre of the Gulf Stream. *Deep Sea Res.*, **33**, 1139–1165.

Hollister, C. and I. McCave, 1984: Sedimentation under deep-sea storms. *Nature*, **309**, 220–225.

Holzer, M., W. Smethie, and Y.-H. Ting, 2018: Ventilation of the subtropical North Atlantic: Locations and times of last ventilation estimated using tracer constraints from GEOTRACES section GA03. *J. Geophys. Res. Oceans*, **123**, doi: 10.1002/2017JC013 698.

Honeyman, B. D., L. S. Balistrieri, and J. W. Murray, 1988: Oceanic trace metal scavenging: The importance of particle concentration. *Deep Sea Res.*, **35**, 227–246.

Honeyman, B. D. and P. H. Santschi, 1989: A Brownian-pumping model for oceanic trace metal scavenging: Evidence from Th isotopes. *J. Marine Res.*, **47**, 951–992.

Jackett, D., T. McDougall, R. Feistel, D. Wright, and S. Griffies, 2004: Algorithms for density, potential temperature, conservative temperature, and the freezing temperature of seawater. *J. Atmos. Ocean. Technol.*, **23**, 1709–1728.

Johns, W., T. Shay, J. Bane, and D. Watts, 1995: Gulf Stream structure, transport, and recirculation near 68°W. *J. Geophys. Res.*, **100**, 817–838.

Klaas, C. and D. E. Archer, 2002: Association of sinking organic matter with various types of mineral ballast in the deep sea: Implications for the rain ratio. *Global Biogeochem. Cycles*, **16**, 1–14.

Kretschmer, S., W. Geibert, M. M. Rutgers van der Loeff, and G. Mollenhauer, 2010: Gran size effects on $^{230}\mathrm{Th}_{\mathrm{xs}}$ inventories in opal-rich and carbonate-rich marine sediments. *Earth Planet. Sci. Lett.*, **294**, 131–142.

Kretschmer, S., W. Geibert, M. M. Rutgers van der Loeff, C. Schnabel, S. Xu, and G. Mollenhauer, 2011: Fractionation of ^{230}Th, ^{231}Pa, and ^{10}Be induced by particle size and composition within an opal-rich sediment of the Atlantic Southern Ocean. *Geochim. Cosmochim. Acta*, **75**, 6971–6987.

Krishnaswami, S., D. Lal, B. L. K. Somayajulu, R. F. Weiss, and H. Craig, 1976: Larve volume in-situ filtration of deep Pacific waters: Mineralogical and radioisotope studies. *Earth Planet. Sci. Lett.*, **32**, 420–429.

Krishnaswami, S., M. M. Sarin, and B. L. K. Somayajulu, 1981: Chemical and radiochemical investigations of surface and deep particles of the Indian Ocean. *Earth Planet. Sci. Lett.*, **54**, 81–96.

Lam, P. J., D. C. Ohnemus, and M. E. Auro, 2015: Size-fractionated major particle composition and concentrations from the US GEOTRACES North Atlantic Zonal Transect. *Deep Sea Res. II*, **116**, 303–320.

Le Bras, I., S. Jayne, and J. Toole, 2018: The interaction of recirculation gyres and a deep boundary current. *J. Phys. Oceanogr.*, **48**, 573–590.

Le Bras, I., I. Yashayaev, and J. Toole, 2017: Tracking Labrador Sea Water signals along the Deep Western Boundary Current. *J. Geophys. Res. Oceans*, **122**, 5348–5366.

Lerner, P., O. Marchal, P. Lam, K. Buesseler, and M. Charette, 2017: Kinetics of thorium and particle cycling along the U.S. GEOTRACES North Atlantic Transect. *Deep Sea Res.*, **125**, 106–128.

Lerner, P., O. Marchal, P. Lam, and A. Solow, 2018: Effects of particle composition on thorium scavenging in the North Atlantic. *Geochim. Cosmochim. Acta*, **233**, 115–134.

Lin, P., L. Guo, and M. Chen, 2014: Adsorption and fractionation of thorium and protactinium on nanoparticles in seawater. *Mar. Chem.*, **162**, 50–59.

Locarnini, R., et al., 2013: World Ocean Atlas 2013, Volume 1: Temperature. NOAA Atlas NESDIS 73, Levitus, S (Ed.) and Mishonov, A. (Tech. Ed.), 40 pp.

Lozier, S. and G. Gawarkiewicz, 2001: Cross-frontal exchange in the Middle Atlantic Bight as evidenced by surface drifters. *J. Phys. Oceanogr.*, **31**, 2498–2510.

Luo, Y., R. François, and S. Allen, 2010: Sediment ^{231}Pa/^{230}Th as a recorder of the Atlantic meridional overturning circulation: Insights from a 2-D model. *Ocean Sci.*, **6**, 381–400.

Marchal, O., R. François, and J. Scholten, 2007: Contribution of ^{230}Th measurements to the estimation of the abyssal circulation. *Deep Sea Res.*, **54**, 557–585.

Marchal, O., R. François, T. F. Stocker, and F. Joos, 2000: Ocean thermohaline circulation and sedimentary ^{231}Pa/^{230}Th ratio. *Paleoceanography*, **15**, 625–641.

Marchal, O. and P. Lam, 2012: What can paired measurements of Th isotope activity and particle concentration can tell us about particle cycling in the ocean? *Geochim. Cosmochim. Acta*, **90**, 126–148.

McCave, I. N., 1985: Size spectra and aggregation of suspended particles in the deep sea. *Deep Sea Res.*, **31**, 329–352.

McCave, I. N., 1986: Local and global aspects of the bottom nepheloid layers in the world ocean. *Neth. J. Sea Res.*, **20**, 167–181.

McManus, J. F., R. François, J.-M. Gherardi, L. D. Keigwin, and S. Brown-Leger, 2004: Collapse and rapid resumption of Atlantic meridional circulation linked to deglacial climate changes. *Nature*, **428**, 834–837.

Meinen, C. S., M. O. Baringer, and R. F. Garcia, 2010: Florida Current transport variability: An analysis of annual and longer-period signals. *Deep Sea Res. I*, **57**, 835–846.

Meinen, C. S. and D. S. Luther, 2016: Structure, transport, and vertical coherence of the Gulf Stream from the Straits of Florida to the Southeast Newfoundland Ridge. *Deep Sea Res. I*, **112**, 137–154.

Mellor, G., 1991: An equation of state for numerical models of oceans and estuaries. *J. Atmos. Ocean. Technol.*, **8**, 609–611.

Mellor, G., 2002: Users guide for a three-dimensional, primitive equation, numerical ocean model. Program in Atmospheric and Oceanic Sciences, Princeton University, Princeton, NJ 08544-0710, 42 pp.

Mellor, G., T. Ezer, and L.-Y. Oey, 1994: The pressure gradient conundrum of sigma coordinate models. *J. Atmos. Ocean. Technol.*, **11**, 1126–1134.

Mellor, G., L.-Y. Oey, and T. Ezer, 1998: Sigma coordinate pressure gradient errors and the seamount problem. *J. Atmos. Ocean. Technol.*, **15**, 1122–1131.

Mellor, G. and T. Yamada, 1982: Development of a turbulent closure model for geophysical fluid problems. *Rev. Geophys.*, **20**, 851–875.

Moran, S. B., M. A. Charette, J. A. Hoff, R. L. Edwards, and W. M. Landing, 1997: Distribution of ^{230}Th in the Labrador Sea and its relation to ventilation. *Earth Planet. Sci. Lett.*, **150**, 151–160.

Moran, S. B., J. A. Hoff, K. O. Buesseler, and R. L. Edwards, 1995: High precision ^{230}Th and ^{232}Th in the Norwegian Sea and Denmark Strait by thermal ionization mass spectrometry. *Geophys. Res. Let.*, **22**, 2589–2592.

Moran, S. B., C.-C. Shen, H. N. Edmonds, S. E. Weinstein, J. N. Smith, and R. L. Edwards, 2002: Dissolved and particulate ^{231}Pa and ^{230}Th in the Atlantic Ocean: Constraints on intermediate/deep water age, boundary scavenging, and ^{231}Pa/^{230}Th fractionation. *Earth Planet. Sci. Lett.*, **203**, 999–1014.

Nozaki, Y., Y. Horibe, and H. Tsubota, 1981: The water column distributions of thorium isotopes in the western North Pacific. *Earth Planet. Sci. Lett.*, **54**, 203–216.

Nyffeler, U. P., Y.-H. Li, and P. H. Santschi, 1984: A kinetic approach to describe trace-element distribution between particles and solution in natural aquatic systems. *Geochim. Cosmochim. Acta*, **48**, 1513–1522.

Owens, S. A., K. O. Buesseler, and K. W. W. Sims, 2011: Re-evaluating the ^{238}U–salinity relationship in seawater: Implications for the ^{238}U–^{234}Th disequilibrium method. *Mar. Chem.*, **127**, 31–39.

Pavia, F., et al., 2018: Intense hydrothermal scavenging of ^{230}Th and ^{231}Pa in the deep Southeast Pacific. *Mar. Chem.*, **201**, 212–228.

Pickart, R. and N. Hogg, 1989: A tracer study of the deep Gulf Stream cyclonic recirculation. *Deep Sea Res.*, **36**, 935–956.

Pickart, R., S. M., and J. Lazier, 1997: Mid-depth ventilation in the western boundary current system of the sub-polar gyre. *Deep Sea Res. I*, **44**, 1025–1054.

Pickart, R. and W. Smethie, 1998: Temporal evolution of the deep western boundary current where it enters the sub-tropical domain. *Deep Sea Res. I*, **45**, 1053–1083.

Quigley, M., P. Santschi, L. Guo, and B. Honeyman, 2001: Sorption irreversibility and coagulation behavior of ^{234}Th with marine organic matter. *Mar. Chem.*, **76**, 27–45.

Quigley, M., P. Santschi, C.-C. Hung, L. Guo, and B. Honeyman, 2002: Importance of polysaccharides for ^{234}Th complexation to marine organic matter. *Limnol. Oceanogr.*, **47**, 367–377.

Rempfer, J., T. Stocker, F. Joos, and J. Lippold, 2017: New insights into cycling of ^{231}Pa and ^{230}Th in the Atlantic Ocean. *Earth Planet. Sci. Lett.*, **468**, 27–37.

Rhein, M., D. Kieke, and R. Steinfeld, 2015: Advection of North Atlantic Deep Water from the Labrador Sea to the southern hemisphere. *J. Geophys. Res. Oceans*, **120**, 2471–2487.

Risien, C. M. and D. B. Chelton, 2008: A global climatology of surface wind and wind stress fields from eight years of QuickSCAT scatterometer data. *J. Phys. Oceanogr.*, **38**, 2379–2413.

Robert, J., C. Miranda, and R. Muxart, 1969: Mesure de la période du protactinium-231 par microcalorimétrie. *Radiochim. Acta*, **11**, 104–108.

Roberts, K., C. Xu, C.-C. Hung, M. Conte, and P. Santschi, 2009: Scavenging and fractionation of thorium vs. protactinium in the ocean, as determined from particle-water partitioning experiments with sediment trap material from Gulf of Mexico and Sargasso Sea. *Earth Planet. Sci. Lett.*, **286**, 131–138.

Roy-Barman, M., C. Jeandel, M. Souhaut, M. Rutgers van der Loeff, I. Voege, N. LeBlond, and R. Freydier, 2005: The influence of particle composition on thorium scavenging in the NE Atlantic ocean (POMME experiment). *Earth Planet. Sci. Lett.*, **240**, 681–693.

Rutgers van der Loeff, M. M. and G. W. Berger, 1993: Scavenging of ^{230}Th and ^{231}Pa near the Antarctic Polar Front in the South Atlantic. *Deep Sea Res. I*, **40**, 339–357.

Rutgers van der Loeff, M. M. and B. P. Boudreau, 1997: The effect of resuspension on chemical exchanges at the sediment - water interface in the deep sea - A modelling and natural radiotracer approach. *J. Marine Sys.*, **11**, 305–342.

Rutgers van der Loeff, M. M., R. Meyer, B. Rudels, and E. Rachor, 2002: Resuspension and particle transport in the benthic nepheloid layer and near Fram Strait in relation to faunal abundances and ^{234}Th depletion. *Deep Sea Res. I*, **49**, 1941–1958.

Ryan, W., et al., 2009: Global multi-resolution topography synthesis. *Geochem. Geophys. Geosys.*, **10**, Q03 014, doi: 10.1029/2008GC002 332.

Santschi, P., U. Nyffeler, Y.-H. Li, and P. O'Hara, 1986: Radionuclide cycling in natural waters: Relevance of scavenging kinetics. *Sediments and Water interactions*, P. Syl, Ed., Springer-Verlag, Vol. 17.

Schlitzer, R., et al., 2018: The GEOTRACES Intermediate Data Product 2017. *Chem. Geol.*, **493**, 210–223.

Schmitz, W. J. and M. S. McCartney, 1993: On the North Atlantic circulation. *Rev. Geophys.*, **31**, 29–49.

Scholten, J. C., M. M. Rutgers van der Loeff, and A. Michel, 1995: Distribution of ^{230}Th and ^{231}Pa in the water column in relation to the ventilation of the deep Arctic basins. *Deep Sea Res. I*, **42**, 1519–1531.

Scholten, J. C., et al., 2005: Radionuclide fluxes in the Arabian Sea: The role of particle composition. *Earth Planet. Sci. Lett.*, **230**, 319–337.

Shchepetkin, A. and J. McWilliams, 2003: A method for computing horizontal pressure-gradient force in an oceanic model with non-aligned vertical coordinate. *J. Geophys. Res.*, **108**, doi:10.1029/2001JC001 047.

Siddall, M., G. Henderson, N. Edwards, M. Frank, S. Müller, T. Stocker, and F. Joos, 2005: ^{231}Pa/^{230}Th fractionation by ocean transport, biogenic particle flux and particle type. *Earth Planet. Sci. Lett.*, **237**, 135–155.

Smagorinsky, J., 1963: General circulation experiments with the primitive equations, I. The basic experiment. *Mon. Weather Rev.*, **91**, 99–164.

Spencer, D., M. Bacon, and P. Brewer, 1981: Models of the distribution of ^{210}Pb in a section across the north equatorial Atlantic Ocean. *J. Marine Res.*, **39**, 119–138.

Thompson, J. and W. Schmitz, 1984: A limited area of the Gulf Stream: Design, initial experiments, and model-data intercomparison. *J. Phys. Oceanogr.*, **19**, 791–814.

Toole, J., M. Andres, I. Le Bras, T. Joyce, and M. McCartney, 2017: Moored observations of the Deep Western Boundary Current in the NW Atlantic: 2004–2014. *J. Geophys. Res. Oceans*, **122**, 7488–7505.

Toole, J., R. Curry, T. Joyce, M. McCartney, and B. Peña Molino, 2011: Transport of the North Atlantic Deep Western Boundary Current about 39°n, 70°w: 2004–2008. *Deep Sea Res. II*, **58**, 1768–1780.

Tréguier, A.-M., C. W. Böning, F. Bryan, G. Danabosoglu, H. Drange, B. Taguchi, and A. Pirani, 2014: CLIVAR WGMD Workshop on high resolution ocean climate modelling: Outcomes and recommendations. CLIVAR Exchanges, Special Issue: High Resolution Ocean Climate Modelling, No. 65.

Tsunogai, S. and M. Minagawa, 1978: Settling model for the removal of insoluble chemical elements in seawater. *Geochim. J.*, **12**, 483–490.

Turnewitsch, R. and B. M. Springer, 2001: Do bottom mixed layers influence ^{234}Th dynamics in the abyssal near-bottom water column? *Deep Sea Res.*, **48**, 1279–1307.

van Hulten, M., J.-C. Dutay, and M. Roy-Barman, 2018: A global scavenging and circulation ocean model of thorium-230 and protactinium-231 with realistic particle dynamics (NEMO-ProThorP 0.1). *Geosci. Model Dev.*, **11**, 3537–3556.

Venchiarutti, C., C. Jeandel, and M. Roy-Barman, 2008: Particle dynamics study in the wake of Kerguelen Island using thorium isotopes. *Deep Sea Res. I*, **55**, 1343–1363.

Vogler, S., J. Scholten, M. Rutgers van der Loeff, and A. Mangini, 1998: ^{230}Th in the eastern North Atlantic: The importance of water mass ventilation in the balance of ^{230}Th. *Earth Planet. Sci. Lett.*, **156**, 61–74.

Wunsch, C., 2006: *Discrete inverse and state estimation problems*. Cambridge University Press, 371 pp.

Yu, E.-F., 1994: Variations in the particulate flux of ^{230}Th and ^{231}Pa and paleoceanographic applications of the ^{231}Pa/^{230}Th ratio. Ph.D. thesis, Woods Hole Oceanographic Institution, Woods Hole, MA, USA.

Yu, E.-F., R. François, and M. P. Bacon, 1996: Similar rates of modern and last-glacial ocean thermohaline circulation inferred from radiochemical data. *Nature*, **379**, 689–694.

Zweng, M., et al., 2013: World Ocean Atlas 2013, Volume 2: Salinity. NOAA Atlas NESDIS 74, Levitus, S (Ed.) and Mishonov, A. (Tech. Ed.), 39 pp.

List of Tables

Table 1: Thorium-230 and Protactinium-231 Data Used in this Study

station	latitude	longitude	#[a] ^{230}Th$_d$	# ^{230}Th$_p$	# ^{231}Pa$_d$	# ^{231}Pa$_p$	error[b]	reference
CMME-13	32.76°N	70.78°W	8	8	11	0	1σ	Cochran et al. (1987)
S1	36.05°N	74.43°W	11	10	19	0	2σ	Guo et al. (1995)
EN407-3	39.47°N	68.37°W	11	0	0	0	2σ	Luo et al. (2010)
EN407-4	38.6°N	68.89°W	19	0	0	0	2σ	Luo et al. (2010)
EN407-6	39.73°N	69.75°W	19	0	0	0	2σ	R. François (pers. com.)
BATS	32°N	64°W	19	0	0	0	2σ	R. François (pers. com.)
OC278-2	37°N	69°W	11	0	0	0	2σ	R. François (pers. com.)
OC278-3	33°N	69°W	11	0	0	0	2σ	R. François (pers. com.)
OC278-4	36°N	68°W	10	0	0	0	2σ	R. François (pers. com.)
OC278-5	38°N	70°W	11	0	0	0	2σ	R. François (pers. com.)
GT11-01	39.69°N	69.81°W	25	10	25	10	1σ	Hayes et al. (2015a)
GT11-02	39.35°N	69.54°W	17	12	17	12	1σ	Hayes et al. (2015a)
GT11-03	38.67°N	69.10°W	20	12	20	12	1σ	Hayes et al. (2015a)
GT11-04	38.09°N	68.70°W	16	12	16	12	1σ	Hayes et al. (2015a)
GT11-06	37.61°N	68.39°W	20	12	21	12	1σ	Hayes et al. (2015a)
GT11-08	35.42°N	66.52°W	17	12	17	12	1σ	Hayes et al. (2015a)
GT11-10	31.75°N	64.17°W	28	12	28	11	1σ	Hayes et al. (2015a)
GT11-12	29.70°N	56.82°W	18	12	18	12	1σ	Hayes et al. (2015a)
GT11-14	27.58°N	49.63°W	21	12	21	11	1σ	Hayes et al. (2015a)

[a] number of observations. [b] σ is the standard error for data from R. François (pers. com.) and the standard deviation for all other data.

Table 2: Parameters of the physical model component

Physical Parameters

		value	units
ρ_o	reference density	1025	kg m^{-3}
g	acceleration due to gravity	9.806	m s^{-2}
C	Smagorinsky coefficient	0.2	1
κ	von Kármán constant	0.4	1
$\kappa_{u,o}$	background vertical viscosity	0	m^2 s^{-1}
$\kappa_{T,o}$	background vertical diffusivity	0	m^2 s^{-1}
P_r	turbulent Prandtl number	5	1
z_r	bottom roughness parameter	0.01	m
τ	restoring time scale for SST and SSS	14.4	d

Numerical Parameters

		value	units
Δt_E	time step (external mode)	15	s
Δt_I	time step (internal mode)	450	s
Δs	step interval for advective terms[a]	5	1
$h_{\max}$	maximum depth in radiation condition	200	m
$u_{\max}$	maximum velocity for CFL violation	100	m s^{-1}
c	constant of Asselin filter	0.1	1
α	weight for surface slope term[b]	0	1

[a] Step interval during which advective terms of the external mode are not updated
[b] Weight used for surface slope terms in the external mode equations

Table 3: Parameters of the geochemical model component

		value	units
$\lambda_{\text{Th-230}}$	radioactive decay constant of ^{230}Th	9.17×10^{-6}	yr^{-1}
$\lambda_{\text{Pa-231}}$	radioactive decay constant of ^{231}Pa	2.12×10^{-5}	yr^{-1}
^{234}U	activity of ^{234}U	2750	dpm m^{-3}
^{235}U	activity of ^{235}U	108	dpm m^{-3}
k_1(Th)	adsorption rate constant for Th	variable	yr^{-1}
k_1(Pa)	adsorption rate constant for Pa	variable	yr^{-1}
$k_{1,b}$(Th)	background value of k_1(Th)	0.4	yr^{-1}
$k_{1,b}$(Pa)	background value of k_1(Pa)	0.04	yr^{-1}
k'_1(Th)	sensitivity of k_1(Th) to particle concentration	0.04	yr^{-1} mg^{-1} m^3
k'_1(Pa)	sensitivity of k_1(Pa) to particle concentration	0.02	yr^{-1} mg^{-1} m^3
k_{-1}(Th)	desorption rate constant for Th	3.69	yr^{-1}
k_{-1}(Pa)	desorption rate constant for Pa	18.45	yr^{-1}
w_p(Th)	settling speed of $^{230}\text{Th}_p$	1800	m yr^{-1}
w_p(Pa)	settling speed of $^{231}\text{Pa}_p$	2400	m yr^{-1}

Table 4: Root Mean Square Difference Between Observed & Simulated Activities†

	$^{230}Th_d$	$^{230}Th_p$	$^{231}Pa_d$	$^{231}Pa_p$
n	238	100	161	84
reference solution	0.078	0.028	0.039	0.001
k_1' / 2	0.086	0.025	0.041	0.001
$k_1' \times 2$	0.086	0.037	0.037	0.003
DWBC inflow = 10 Sv	0.081	0.030	0.040	0.002
DWBC inflow = 40 Sv	0.076	0.029	0.037	0.002
$A_{d,p}$(DWBC inflow) / 2	0.078	0.025	0.033	0.001
$A_{d,p}$(DWBC inflow) $\times 2$	0.165	0.041	0.110	0.002
uniform $k_1(Th)$ & $k_1(Pa)$	0.075	0.043	0.041	0.002
$A_{d,p}$(DWBC inflow) / 2, DWBC inflow = 10 Sv	0.093	0.027	0.041	0.002

†All values in dpm m^{-3}

Table 5: Thorium-230 and Protactinium-231 Data Used in this Study

core	latitude	longitude	depth (m)	$^{231}Pa/^{230}Th$	reference
OCE152-BC1	39.49°N	70.57°W	1126	0.082	Anderson et al. (1994)
OCE152-BC8	32.47°N	70.58°W	1596	0.071	Anderson et al. (1994)
OCE152-BC9	39.42°N	70.55°W	1981	0.091	Anderson et al. (1994)
OCE152-BC5	39.08°N	70.56°W	2691	0.063	Anderson et al. (1994)
EN123-BC4	39.48°N	70.56°W	1280	0.076	Anderson et al. (1994)
EN123-BC6	39.49°N	70.55°W	1643	0.066	Anderson et al. (1994)
EN123-BC3	39.35°N	70.55°W	2344	0.061	Anderson et al. (1994)
EN123-BC1	39.08°N	70.55°W	2736	0.053	Anderson et al. (1994)
EN179-BC5	37.38°N	74.13°W	384	0.127	Anderson et al. (1994)
EN179-BC2	37.37°N	74.10°W	892	0.050	Anderson et al. (1994)
EN179-BC3	37.38°N	74.09°W	1031	0.075	Anderson et al. (1994)
EN179-BC4	37.32°N	74.02°W	1318	0.071	Anderson et al. (1994)
EN179-BC7	37.25°N	73.49°W	1989	0.051	Anderson et al. (1994)
EN187-BC4	37.37°N	74.13°W	512	0.063	Anderson et al. (1994)
EN187-BC10	36.52°N	74.37°W	580	0.089	Anderson et al. (1994)
EN187-BC8	36.52°N	74.34°W	1020	0.053	Anderson et al. (1994)
EN187-BC5	37.37°N	74.10°W	1045	0.069	Anderson et al. (1994)
EN187-BC11	37.02°N	74.34°W	1125	0.062	Anderson et al. (1994)
EN187-BC9	36.52°N	74.34°W	1165	0.075	Anderson et al. (1994)
EN187-BC6	37.24°N	73.5°W	2000	0.055	Anderson et al. (1994)
OCE325-GGC5	33.7°N	57.6°W	4550	0.054	McManus et al. (2004)
VM26-176	32.76°N	70.78°W	1126	0.065	Yu (1994)

List of Figures

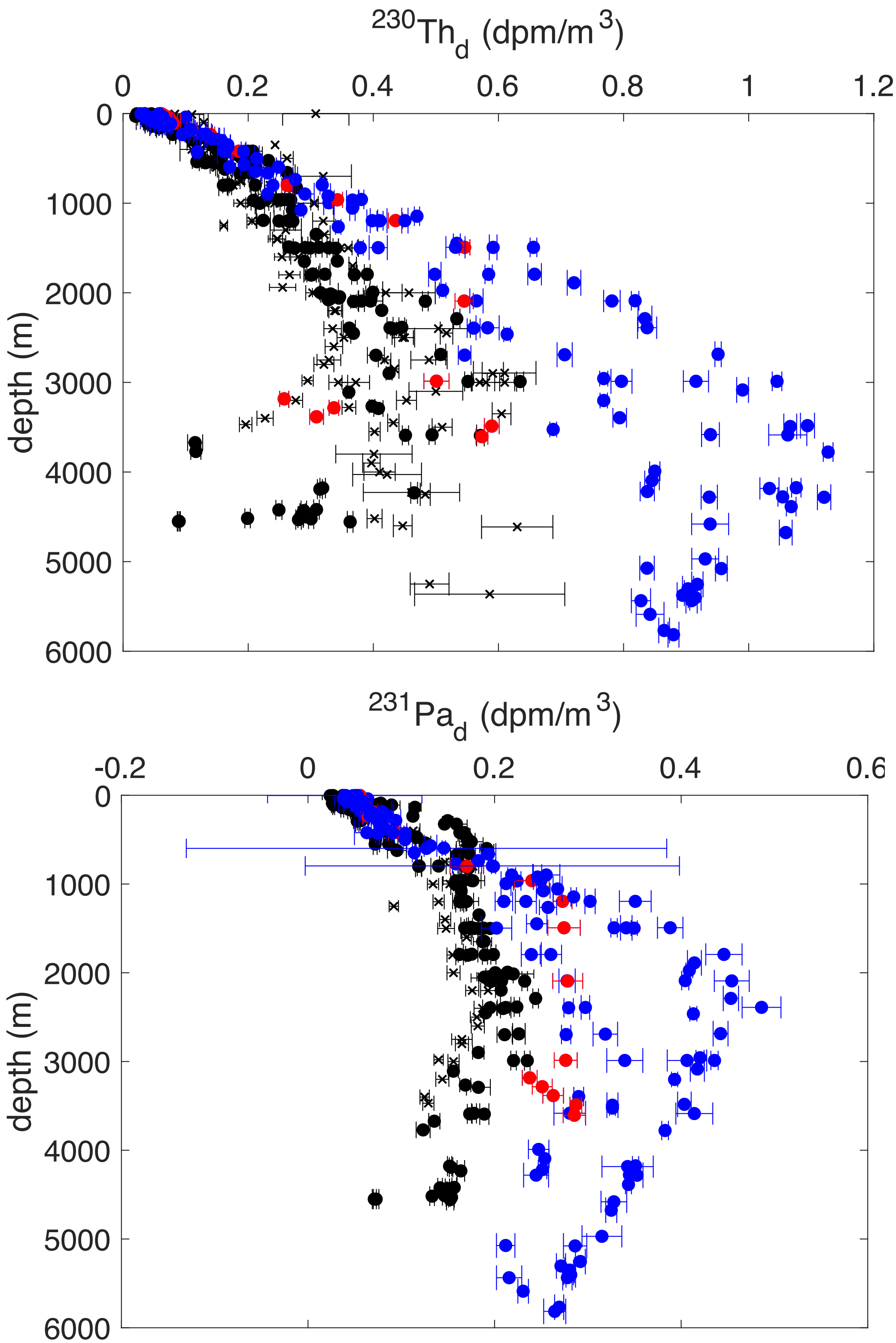

Fig. 1. Vertical profiles of dissolved ^{230}Th and ^{231}Pa activities in the North Atlantic. Data from stations west (east) of Bermuda are shown with black (blue) circles and data from station GT11-16, near the TAG hydrothermal vent, are shown with red circles. The horizontal bars show the measurement uncertainties (see Table 1 for data sources).

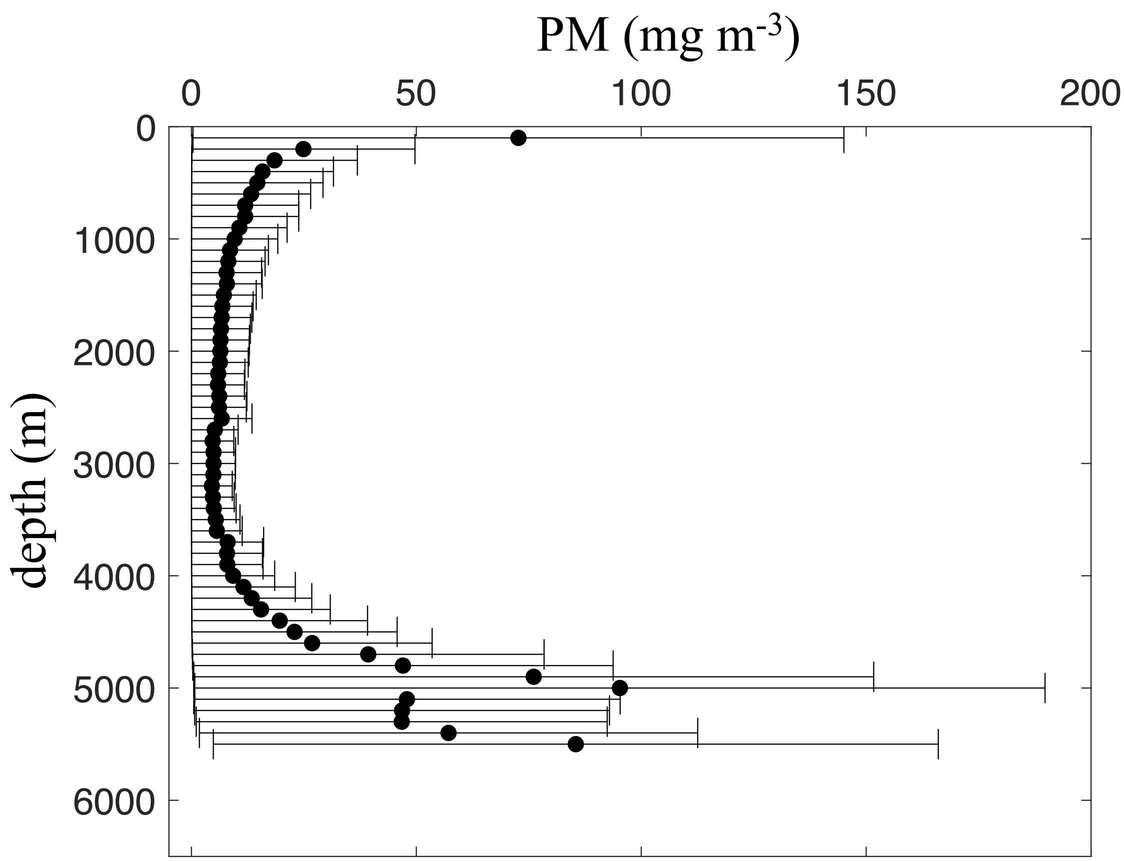

Fig. 2. Regionally averaged vertical profile of particulate matter (PM) concentration in the western North Atlantic. Each circle is an average based on (i) optical measurements converted empirically to PM concentration and (ii) a linear interpolation at the same vertical levels of the concentration estimates obtained from optical profiles at different stations. The horizontal bars show the standard errors of the averages (data compilation from Gardner et al. (2017)).

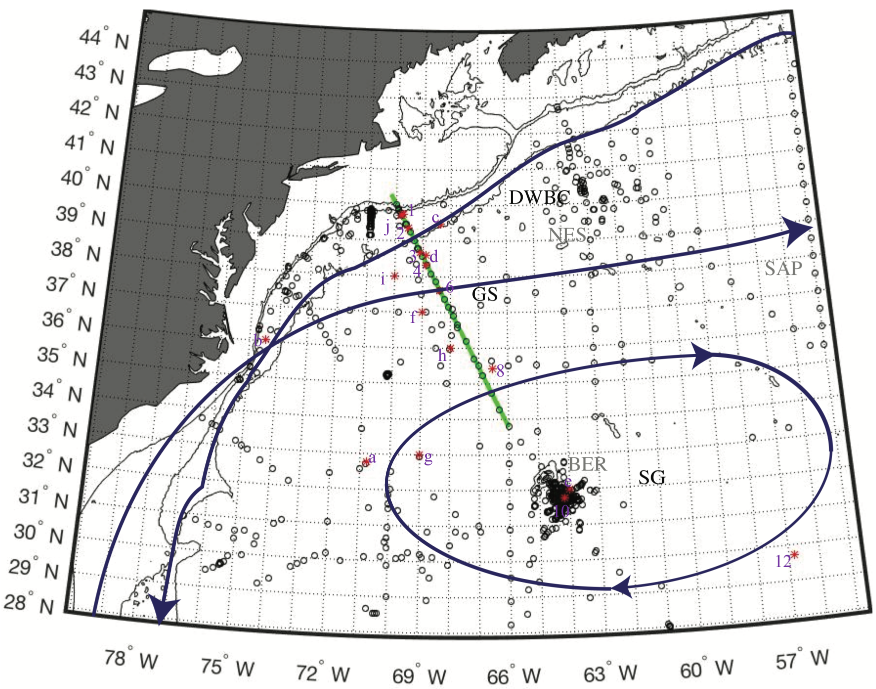

Fig. 3. Map of the study area showing the location of GEOTRACES stations (red stars with numerals), pre-GEOTRACES stations (red stars with letters), and nephelometer and transmissmeter stations (circles). Black lines are isobaths of 200, 1000, and 3000 m, and blue arrows show schematic pathways of the Gulf Stream (GS), Deep Western Boundary Current (DWBC), Northern Recirculation Gyre (NRG), and Subtropical Gyre (SG). Also shown are the approximate locations of Bermuda (BER), the New England Seamounts (NES), and the Sohm Abyssal Plain (SAP). The green line protruding from the continental shelf and slope south of New England is line W.

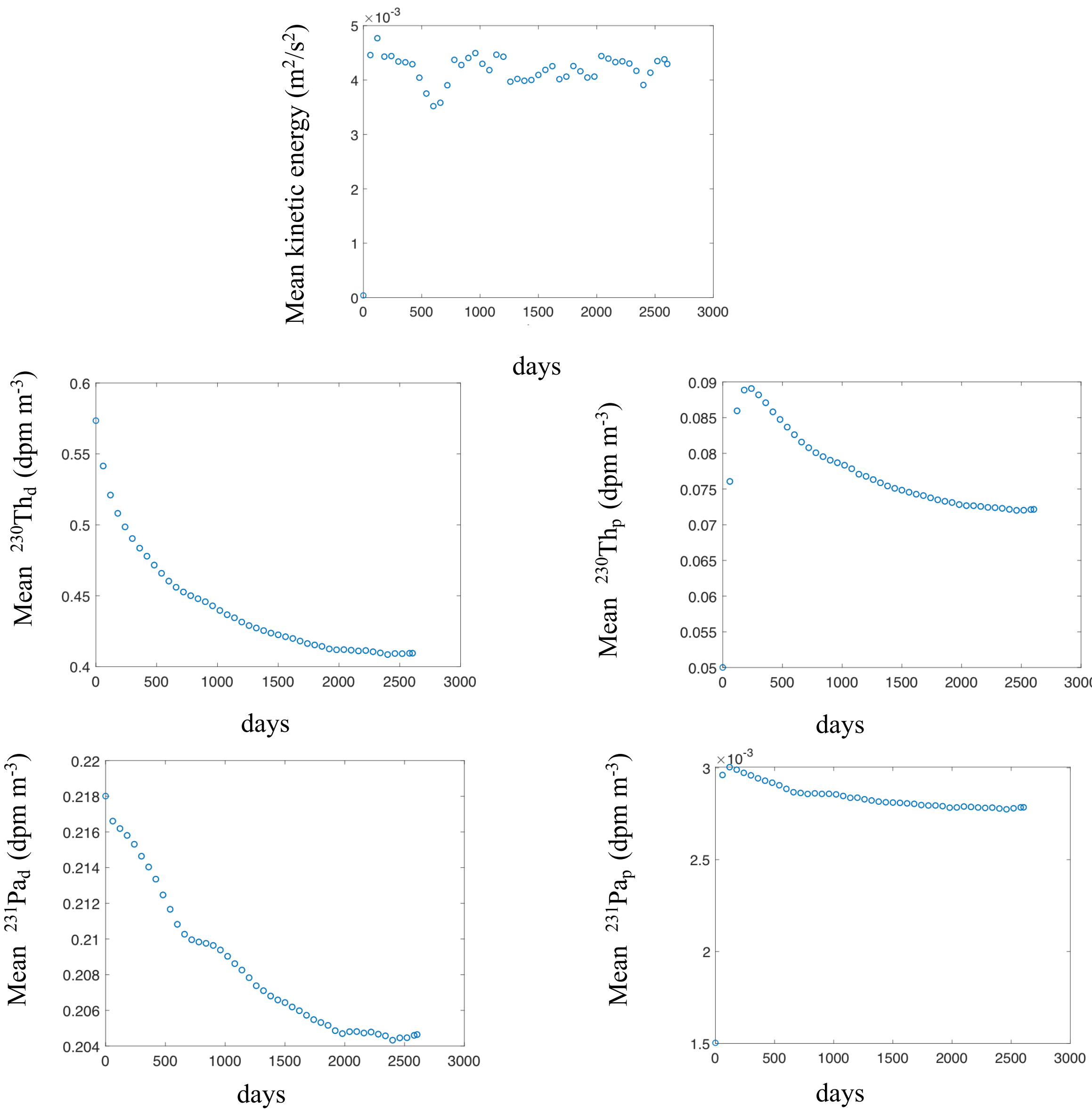

Fig. 4. Time series of the domain-averaged kinetic energy, $^{230}\mathrm{Th}_d$, $^{230}\mathrm{Th}_p$, $^{231}\mathrm{Pa}_d$, and $^{231}\mathrm{Pa}_p$ in the reference solution

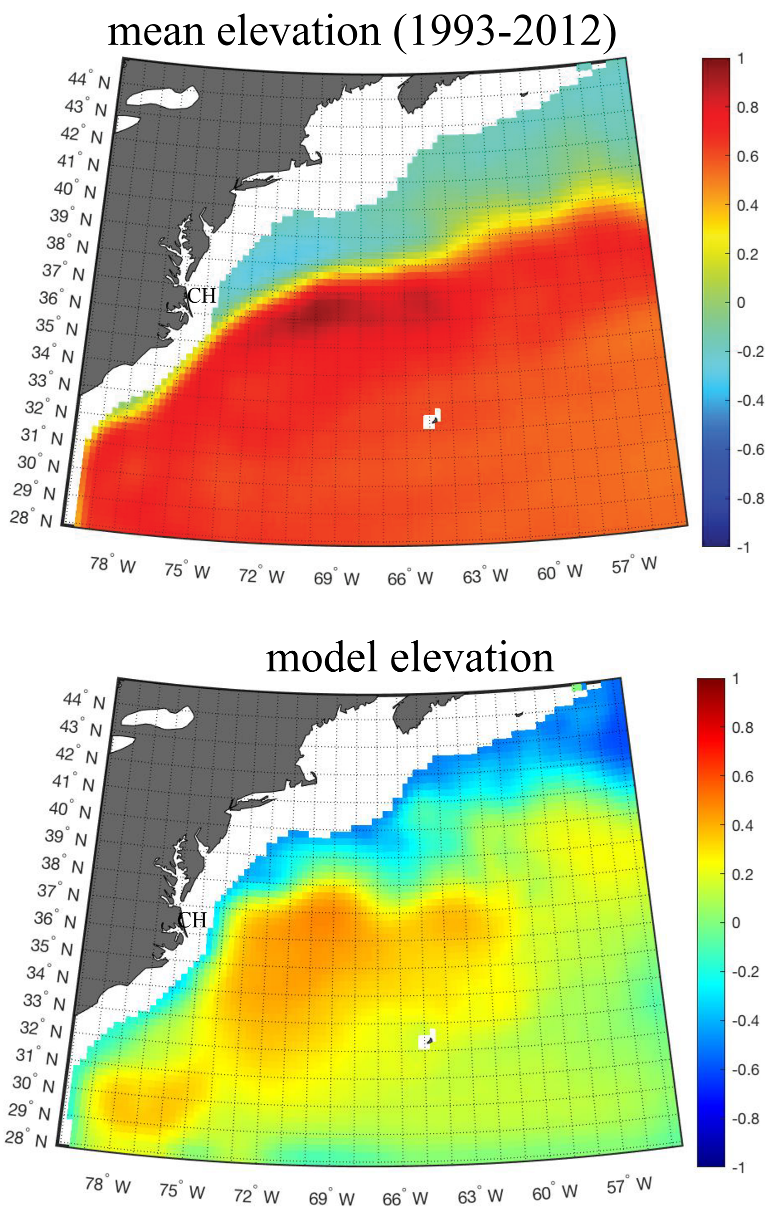

Fig. 5. Averages of sea surface height (m) as observed from satellite altimeter data during the period 1993-2012 (top) and as simulated in the reference solution (bottom). The average pathway of the Gulf Stream coincides with the yellow band (upper panel) and “CH” stands for Cape Hatteras.

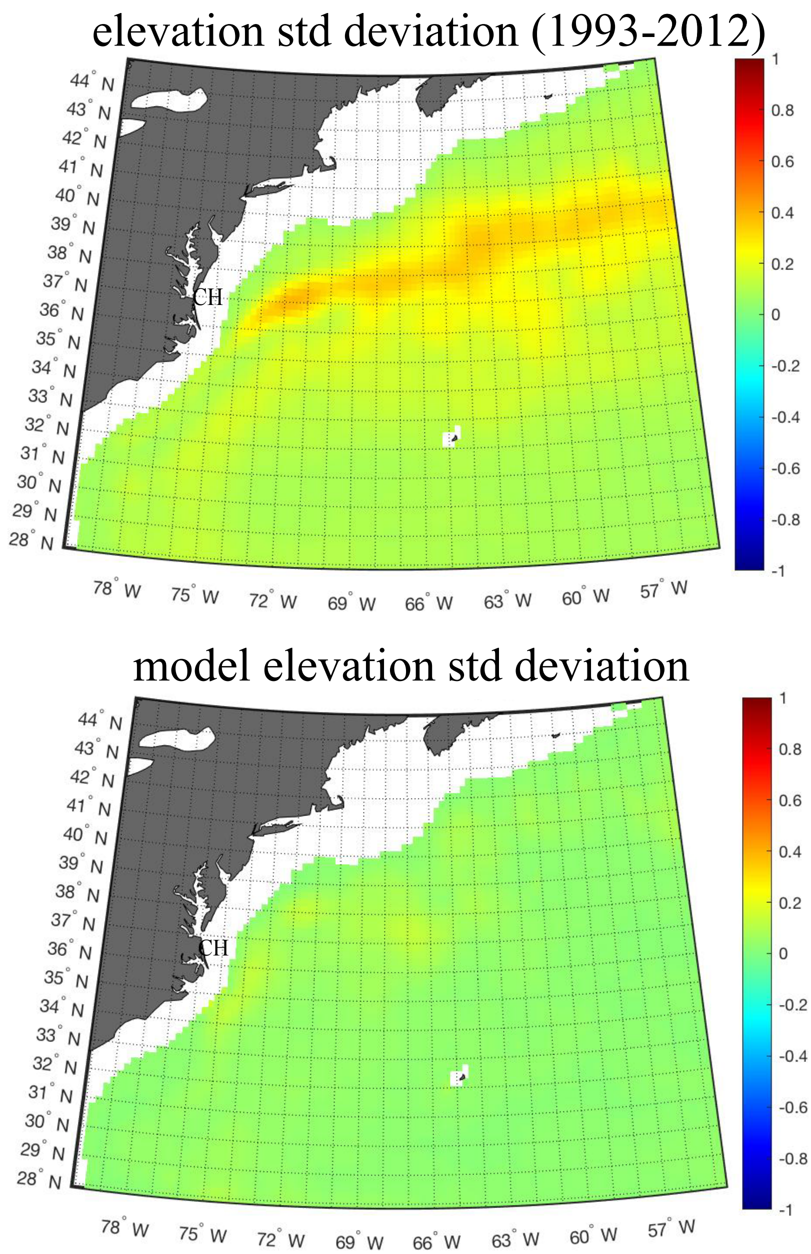

Fig. 6. Standard deviation of sea surface height (m) as observed from satellite altimeter data during the period 1993-2012 (top) and as simulated in the reference solution (bottom). The average pathway of the Gulf Stream coincides with the yellow band (upper panel) and “CH” stands for Cape Hatteras.

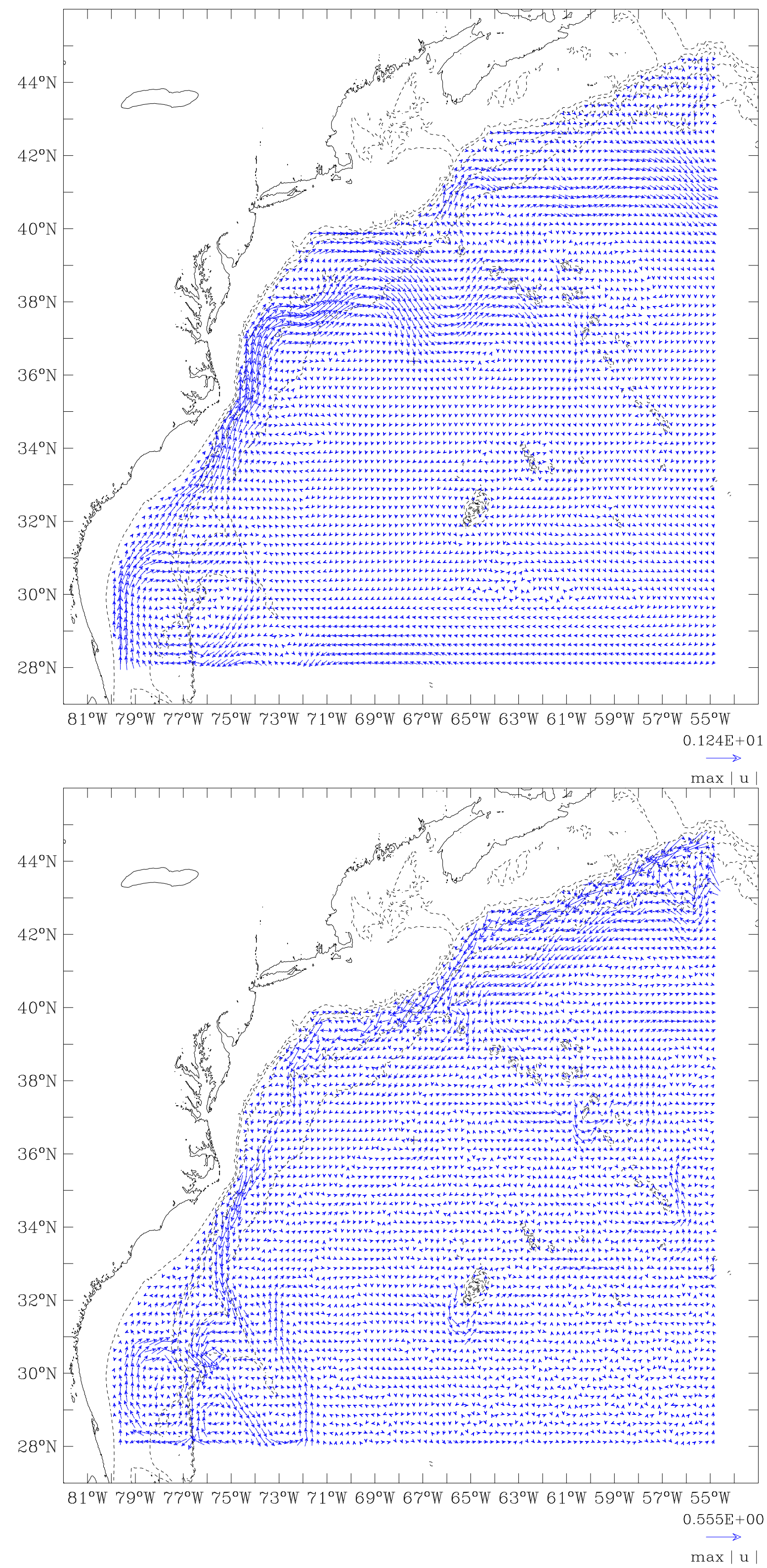

Fig. 7. Field of horizontal velocity in the surface layer (top) and at a depth of 3500 m (bottom) simulated in the reference solution. The horizontal arrow at the lower right outside each panel is the maximum speed in units of m s^{-1} in the corresponding field.

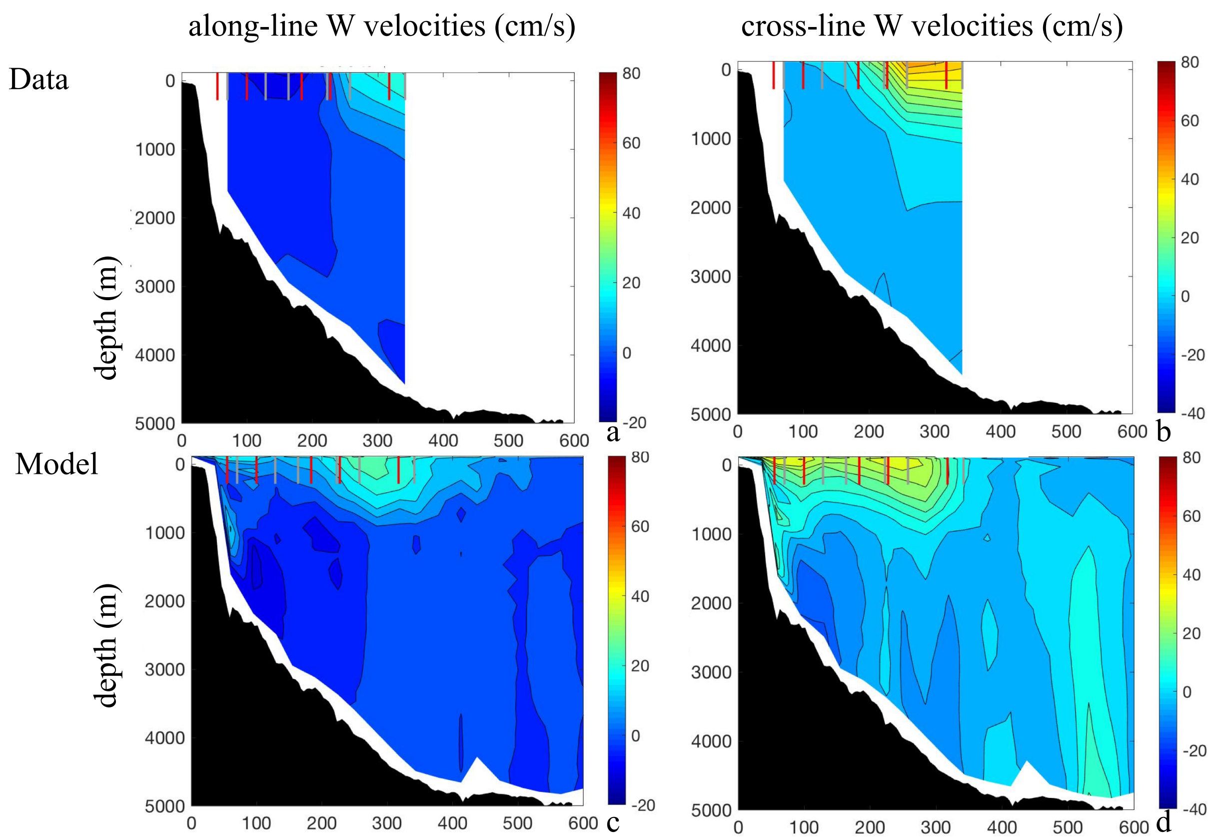

Fig. 8. Distribution of horizontal velocity components between the New England continental shelf and Bermuda as measured during the line W program (top) and as simulated in the reference solution (bottom). At the top of each panel, red vertical lines show the position of GA03 stations GT11-01 to GT11-06, and grey vertical lines show the position of mooring locations. Coordinates along the horizontal axis are distances from 40.125°N,70.125°W (line W data from Toole et al. (2017)).

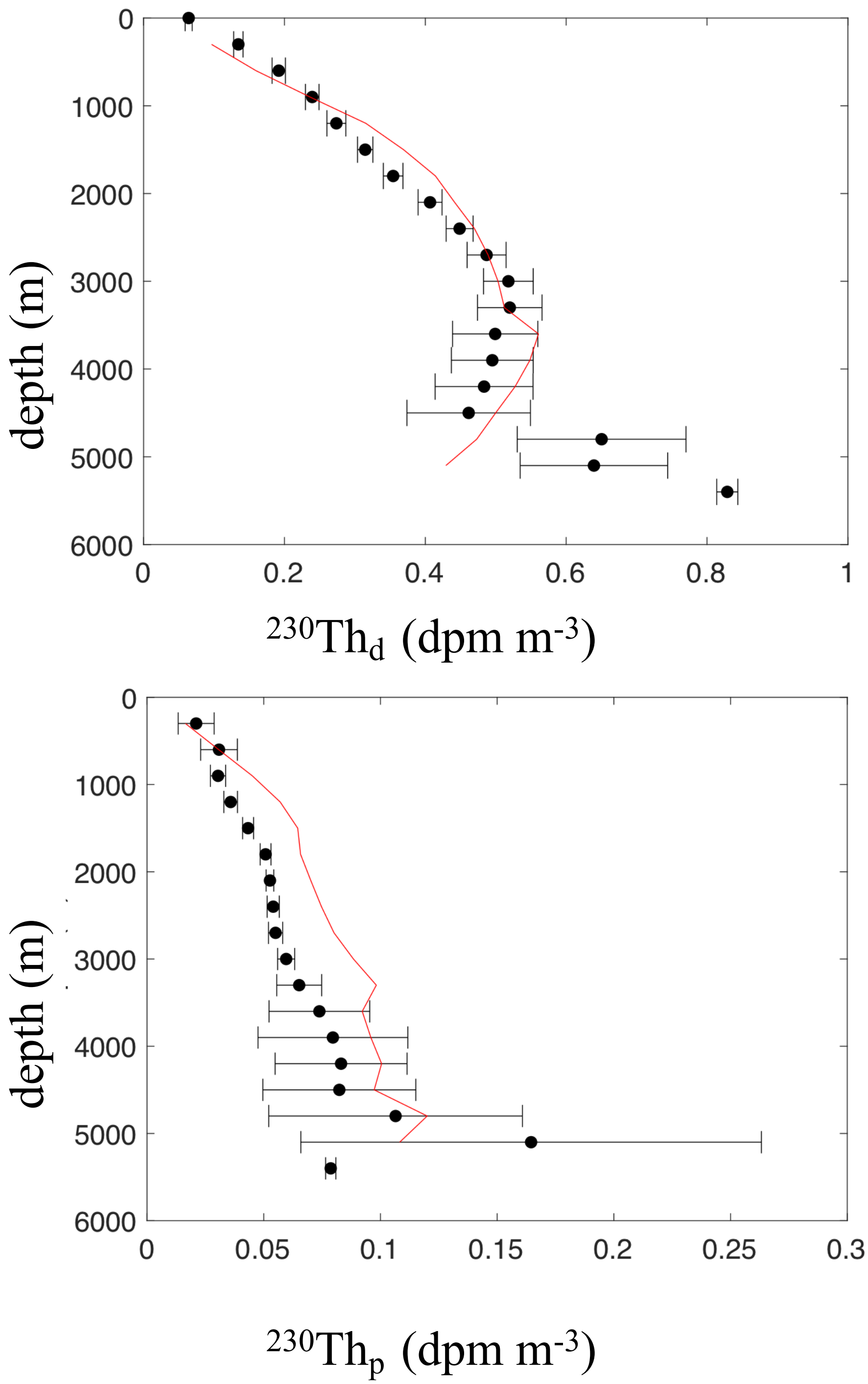

Fig. 9. Profile of station-averaged $^{230}\mathrm{Th}_d$ (top) and $^{230}\mathrm{Th}_p$ (bottom) as calculated from pre-GEOTRACES and GA03 measurements (black circles) and as simulated in the reference solution (red line). The circles show averages of measurements from several stations with the following exceptions: for $^{230}\mathrm{Th}_d$ the shallowest circle is a measurement from a single station (OC278-5), and for $^{230}\mathrm{Th}_{d,p}$ the deepest circle is a measurement from a single station (GT11-12). The horizontal bars show the standard errors of the averages (measurement error for the shallowest $^{230}\mathrm{Th}_d$ measurement and the deepest $^{230}\mathrm{Th}_{d,p}$ measurements; Table 1). The extreme values of $^{230}\mathrm{Th}_p$ near the bottom of stations GT11-04 and GT11-08 are excluded from the station-averaged profile of the measurements.

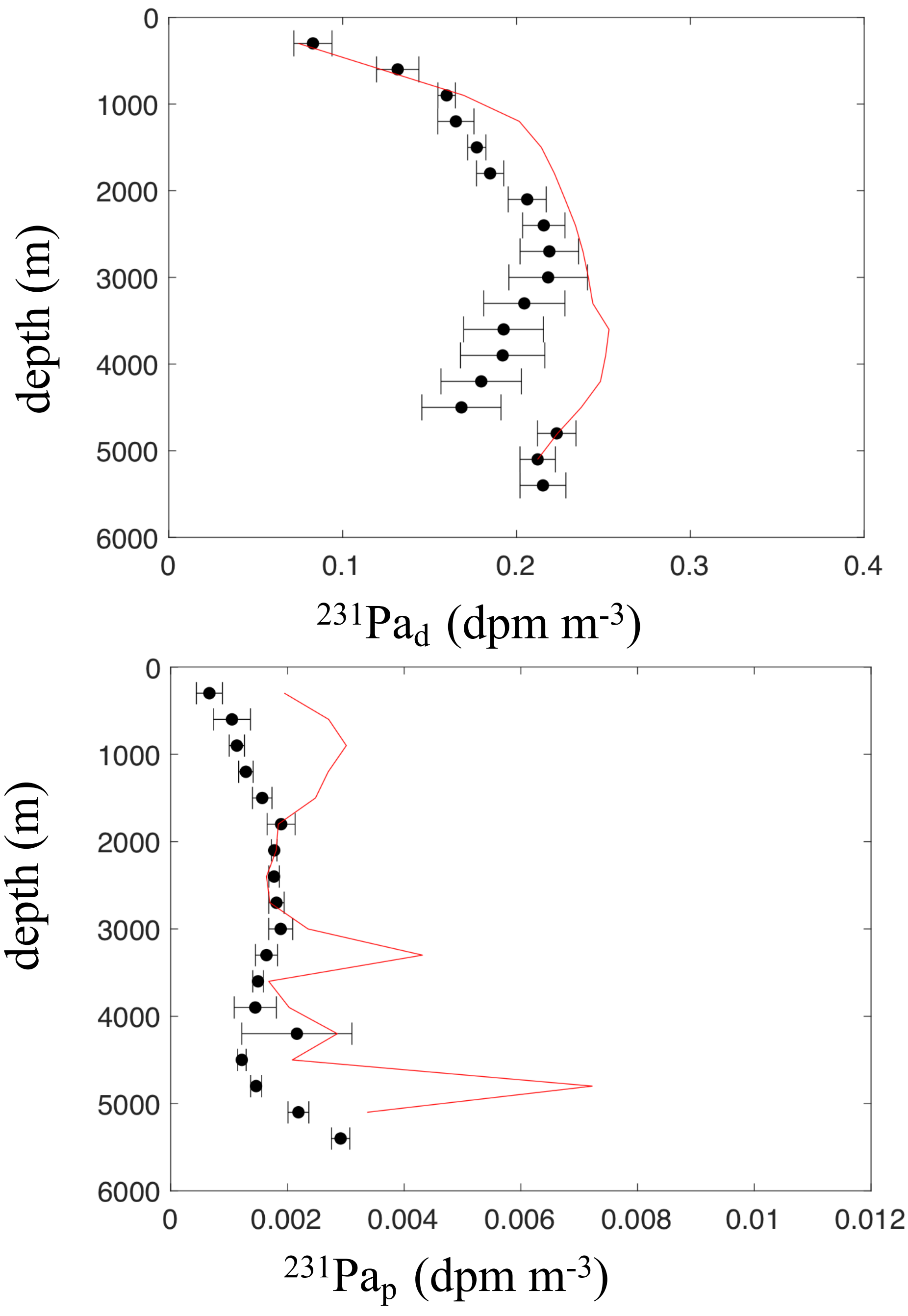

Fig. 10. Profile of station-averaged $^{231}Pa_d$ (top) and $^{231}Pa_p$ (bottom) as calculated from pre-GEOTRACES and GA03 measurements (black circles) and as simulated in the reference solution (red line). The circles show averages of measurements from several stations with the following exceptions: for $^{231}Pa_d$ ($^{231}Pa_p$), the three (four) deepest circles show measurements from a single station (GT11-12). The horizontal bars show the standard errors of the averages (measurement error for the three (four) deepest measurements of $^{231}Pa_d$ ($^{231}Pa_p$); Table 1). The extreme values of $^{231}Pa_p$ near the bottom of stations GT11-04 and GT11-08 are excluded from the station-averaged profile of the measurements.

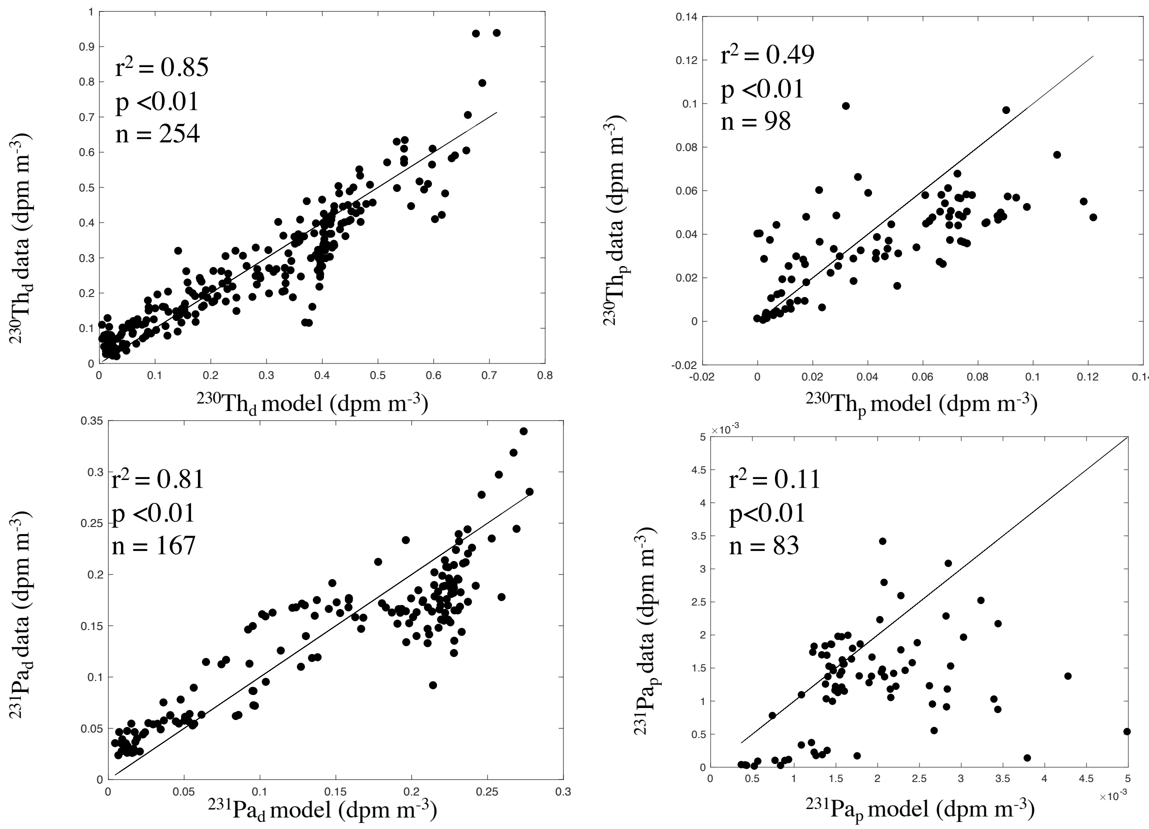

Fig. 11. Scatter plots of measured radionuclide activities versus simulated radionuclide activities in the reference solution. Shown in each panel are the squared Pearson correlation coefficient (r^2), the p value of the correlation, and the number of measurements (n). In each panel, the black line is the line of perfect agreement. For panel (b) and (d), the extreme measured values of $^{230}\mathrm{Th}_p$ and $^{231}\mathrm{Pa}_p$ near the bottom of stations GT11-04 and GT11-08, along with the corresponding model values, are excluded from the scatter plot.

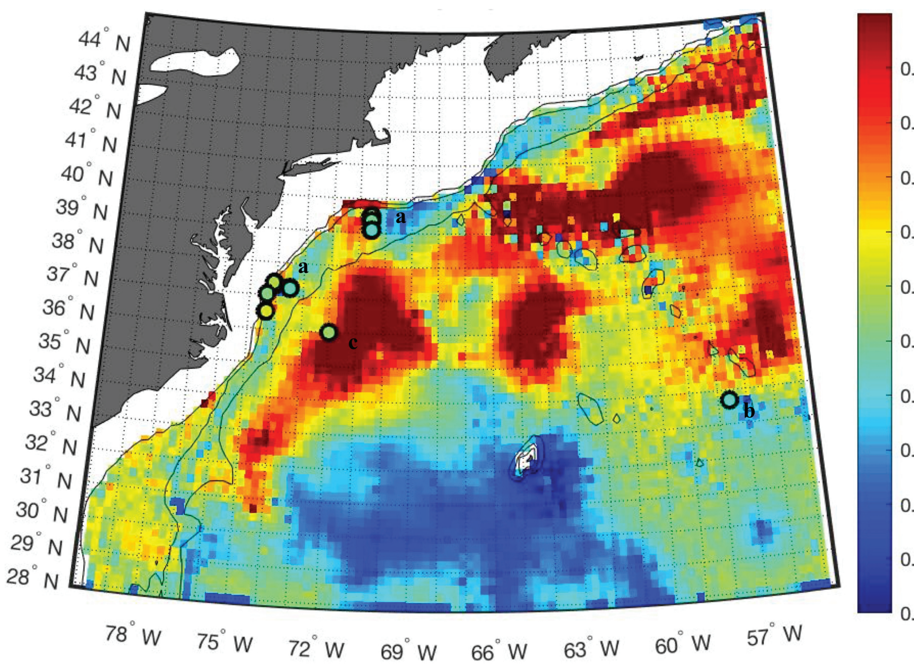

Fig. 12. Distribution of near-bottom $^{231}\mathrm{Pa}_p/^{230}\mathrm{Th}_p$ in the reference experiment. The filled circles are surface sediment data (Table 5), and the solid black lines are the 200 m, 1000 m, and 3000 m isobath, respectively.

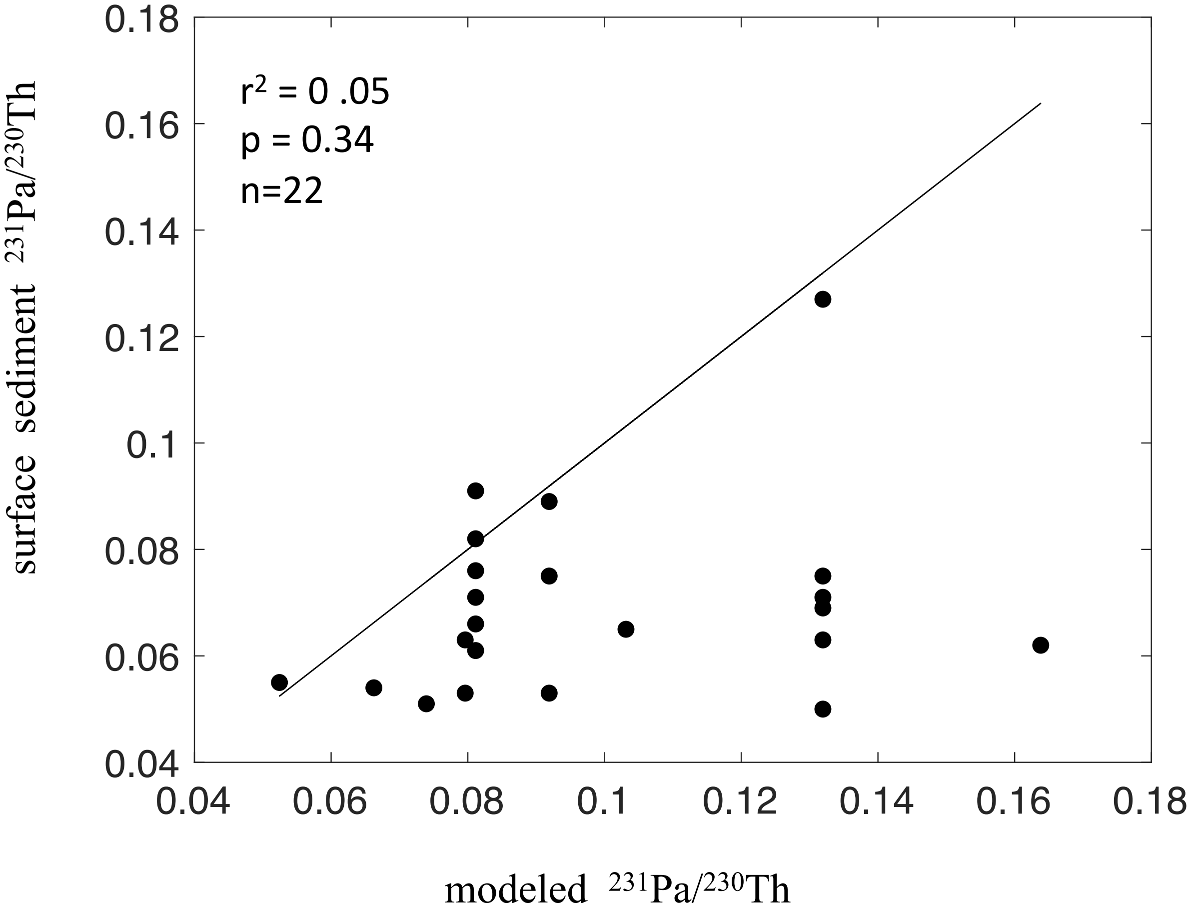

Fig. 13. Scatter plot of surface sediment ^{231}Pa/^{230}Th data versus the near-bottom $^{231}\mathrm{Pa}_p/^{230}\mathrm{Th}_p$ simulated near the corresponding data location in the reference experiment. The regression coefficient (slope) is 0.35 ± 0.36 (one standard error) and the Pearson correlation coefficient is 0.21 ($n = 22$). The black line is the line of perfect agreement.

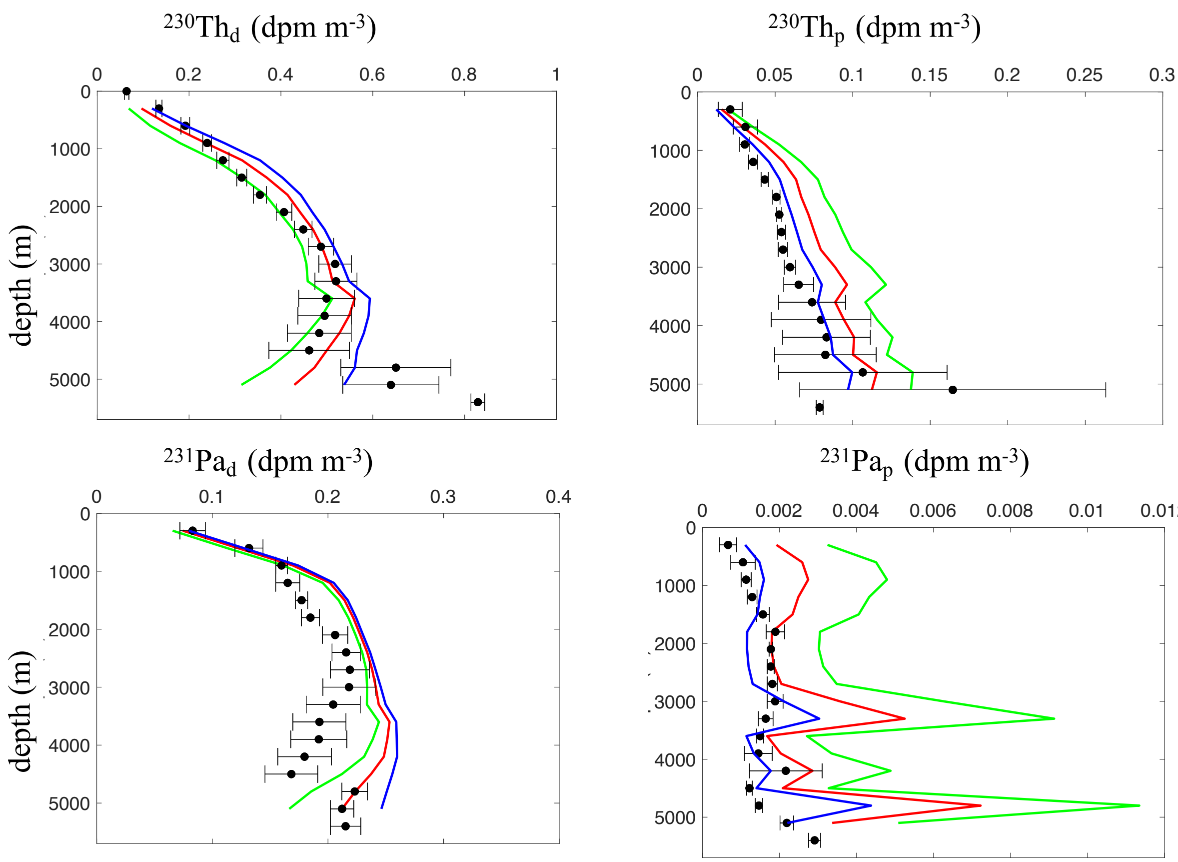

Fig. 14. Profile of station-averaged $^{230}\mathrm{Th}_{d,p}$ (top) and $^{231}\mathrm{Pa}_{d,p}$ (bottom) as calculated from (pre-)GEOTRACES measurements (black circles) and as simulated for $k_1'(\mathrm{Th}) = 0.02$ yr^{-1} mg^{-1} m^3 and $k_1'(\mathrm{Pa}) = 0.01$ yr^{-1} mg^{-1} m^3 (blue lines), $k_1'(\mathrm{Th}) = 0.04$ yr^{-1} mg^{-1} m^3 and $k_1'(\mathrm{Pa}) = 0.02$ yr^{-1} mg^{-1} m^3 (red, reference solution), and $k_1'(\mathrm{Th}) = 0.08$ yr^{-1} mg^{-1} m^3 and $k_1'(\mathrm{Pa}) = 0.04$ yr^{-1} mg^{-1} m^3 (green). The circles show averages of measurements from several stations, with the exceptions listed in Figure 9 for $^{230}\mathrm{Th}_{d,p}$ and in Figure 10 for $^{231}\mathrm{Pa}_{d,p}$. The horizontal bars show the standard errors of the averages (measurement error for the shallowest $^{230}\mathrm{Th}_d$ measurement, the deepest $^{230}\mathrm{Th}_{d,p}$ measurements, and the three (four) deepest measurements of $^{231}\mathrm{Pa}_d$ ($^{231}\mathrm{Pa}_p$); Table 1). The extreme values of $^{230}\mathrm{Th}_p$ (Fig. 3) and $^{231}\mathrm{Pa}_p$ (Fig. 6) near the bottom of stations GT11-04 and GT11-08 are excluded from the station-averaged profile of the measurements.

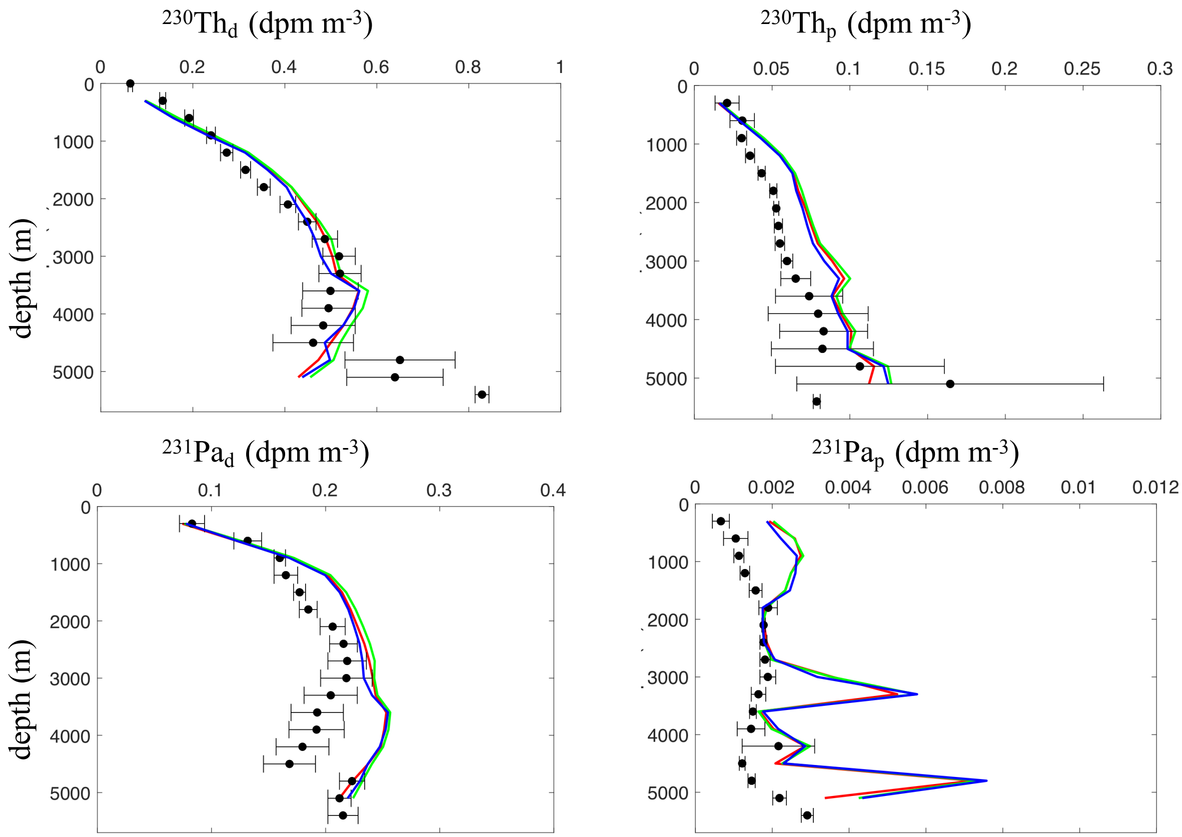

Fig. 15. Profile of station-averaged $^{230}\mathrm{Th}_{d,p}$ (top) and $^{231}\mathrm{Pa}_{d,p}$ (bottom) as calculated from (pre-)GEOTRACES measurements (black circles) and as simulated when the strength of the DWBC at its inflow location is set to 10 Sv (green lines), 20 Sv (red, reference solution), and 40 Sv (blue). The circles show averages of measurements from several stations, with the exceptions listed in Figure 9 for $^{230}\mathrm{Th}_{d,p}$ and in Figure 10 for $^{231}\mathrm{Pa}_{d,p}$. The horizontal bars show the standard errors of the averages (measurement error for the shallowest $^{230}\mathrm{Th}_d$ measurement, the deepest $^{230}\mathrm{Th}_{d,p}$ measurements, and the three (four) deepest measurements of $^{231}\mathrm{Pa}_d$ ($^{231}\mathrm{Pa}_p$); Table 1). The extreme values of $^{230}\mathrm{Th}_p$ (Fig. 3) and $^{231}\mathrm{Pa}_p$ (Fig. 6) near the bottom of stations GT11-04 and GT11-08 are excluded from the station-averaged profile of the measurements.

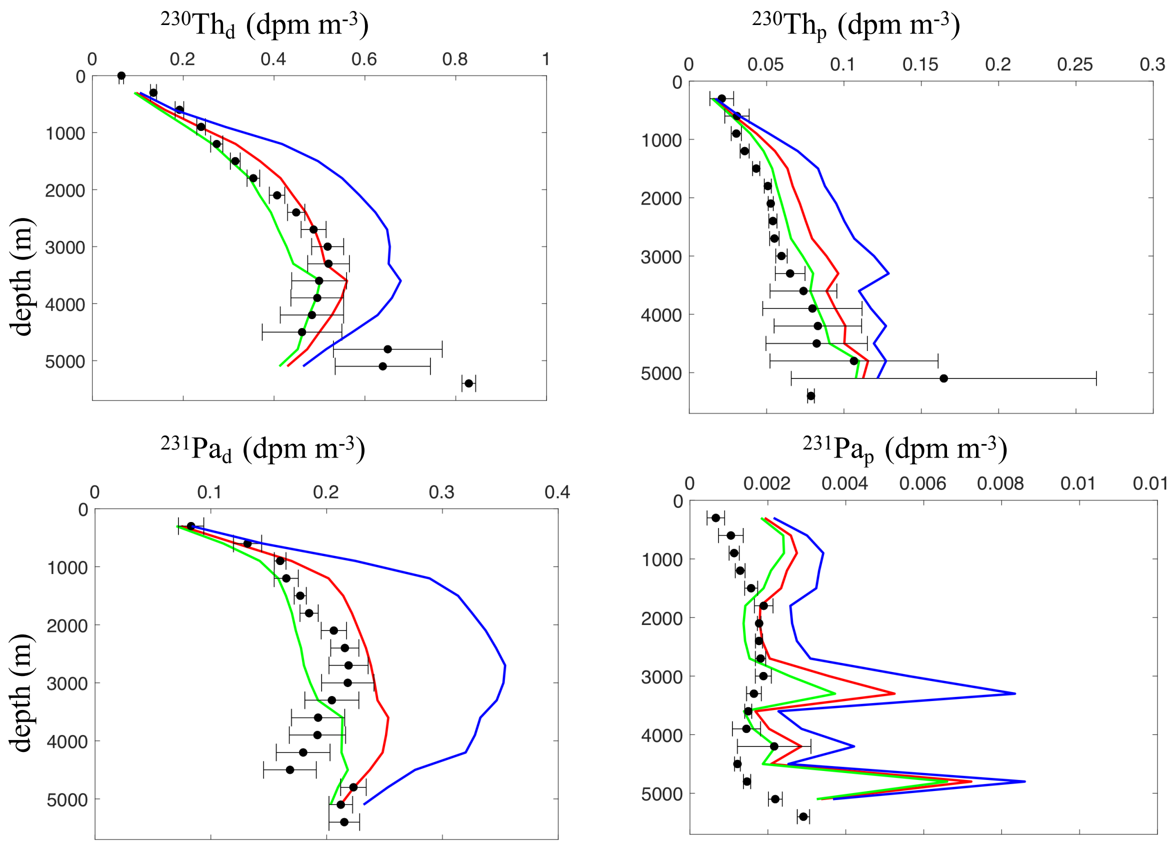

Fig. 16. Profile of station-averaged $^{230}Th_{d,p}$ (top) and $^{231}Pa_{d,p}$ (bottom) as calculated from (pre-)GEOTRACES measurements (black circles) and as simulated when the radionuclide activities at the DWBC inflow are halved (green lines) or doubled (blue) compared to their values in the reference solution (red). The circles show averages of measurements from several stations, with the exceptions listed in Figure 9 for $^{230}Th_{d,p}$ and in Figure 10 for $^{231}Pa_{d,p}$. The horizontal bars show the standard errors of the averages (measurement error for the shallowest $^{230}Th_d$ measurement, the deepest $^{230}Th_{d,p}$ measurements, and the three (four) deepest measurements of $^{231}Pa_d$ ($^{231}Pa_p$); Table 1). The extreme values of $^{230}Th_p$ (Fig. 3) and $^{231}Pa_p$ (Fig. 6) near the bottom of stations GT11-04 and GT11-08 are excluded from the station-averaged profile of the measurements.

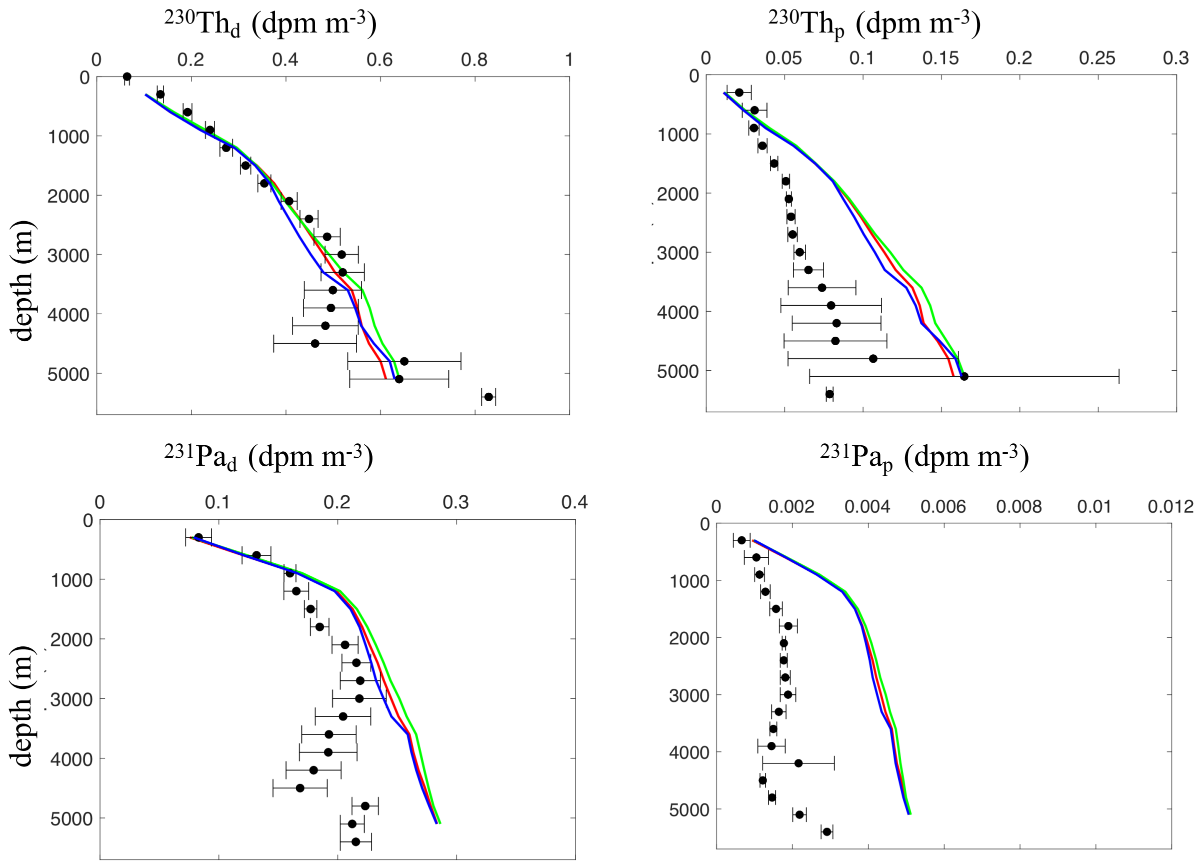

Fig. 17. Profile of station-averaged $^{230}\mathrm{Th}_{d,p}$ (top) and $^{231}\mathrm{Pa}_{d,p}$ (bottom) as calculated from (pre-)GEOTRACES measurements (black circles) and as simulated for uniform k_1(Th) and k_1(Pa) when the strength of the DWBC at its inflow location is set to 10 Sv (green lines), 20 Sv (red), and 40 Sv (blue). The circles show averages of measurements from several stations, with the exceptions listed in Figure 9 for $^{230}\mathrm{Th}_{d,p}$ and in Figure 10 for $^{231}\mathrm{Pa}_{d,p}$. The horizontal bars show the standard errors of the averages (measurement error for the shallowest $^{230}\mathrm{Th}_d$ measurement, the deepest $^{230}\mathrm{Th}_{d,p}$ measurements, and the three (four) deepest measurements of $^{231}\mathrm{Pa}_d$ ($^{231}\mathrm{Pa}_p$); Table 1). The extreme values of $^{230}\mathrm{Th}_p$ (Fig. 3) and $^{231}\mathrm{Pa}_p$ (Fig. 6) near the bottom of stations GT11-04 and GT11-08 are excluded from the station-averaged profile of the measurements.

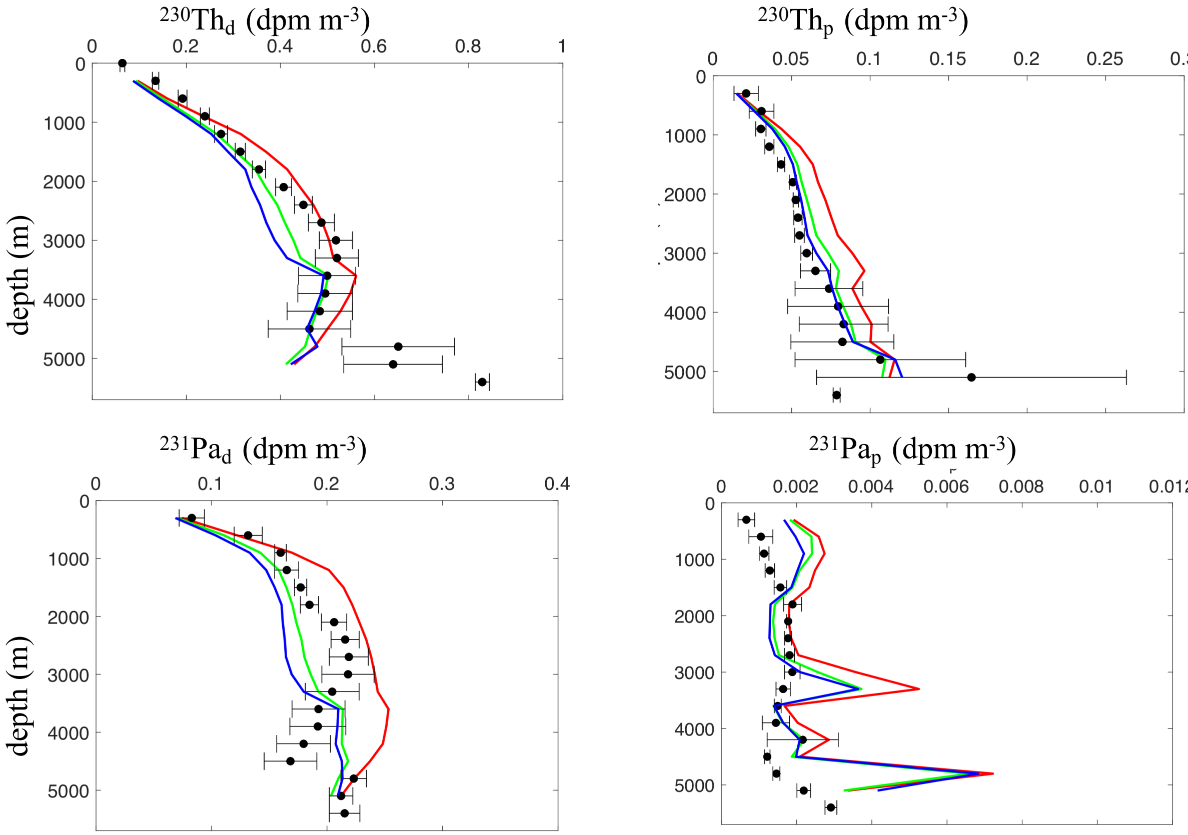

Fig. 18. Profile of station-averaged $^{230}Th_{d,p}$ (top) and $^{231}Pa_{d,p}$ (bottom) as calculated from (pre-)GEOTRACES measurements (black circles) and as simulated for the reference experiment (red), when the radionuclide activities at the DWBC inflow locations are halved (green), and when the radionuclide activities at the DWBC inflow locations are halved, and the DWBC at its inflow is 40 Sv (blue). The circles show averages of measurements from several stations, with the exceptions listed in Figure 9 for $^{230}Th_{d,p}$ and in Figure 10 for $^{231}Pa_{d,p}$. The horizontal bars show the standard errors of the averages (measurement error for the shallowest $^{230}Th_d$ measurement, the deepest $^{230}Th_{d,p}$ measurements, and the three (four) deepest measurements of $^{231}Pa_d$ ($^{231}Pa_p$); Table 1). The extreme values of $^{230}Th_p$ (Fig. 3) and $^{231}Pa_p$ (Fig. 6) near the bottom of stations GT11-04 and GT11-08 are excluded from the station-averaged profile of the measurements.

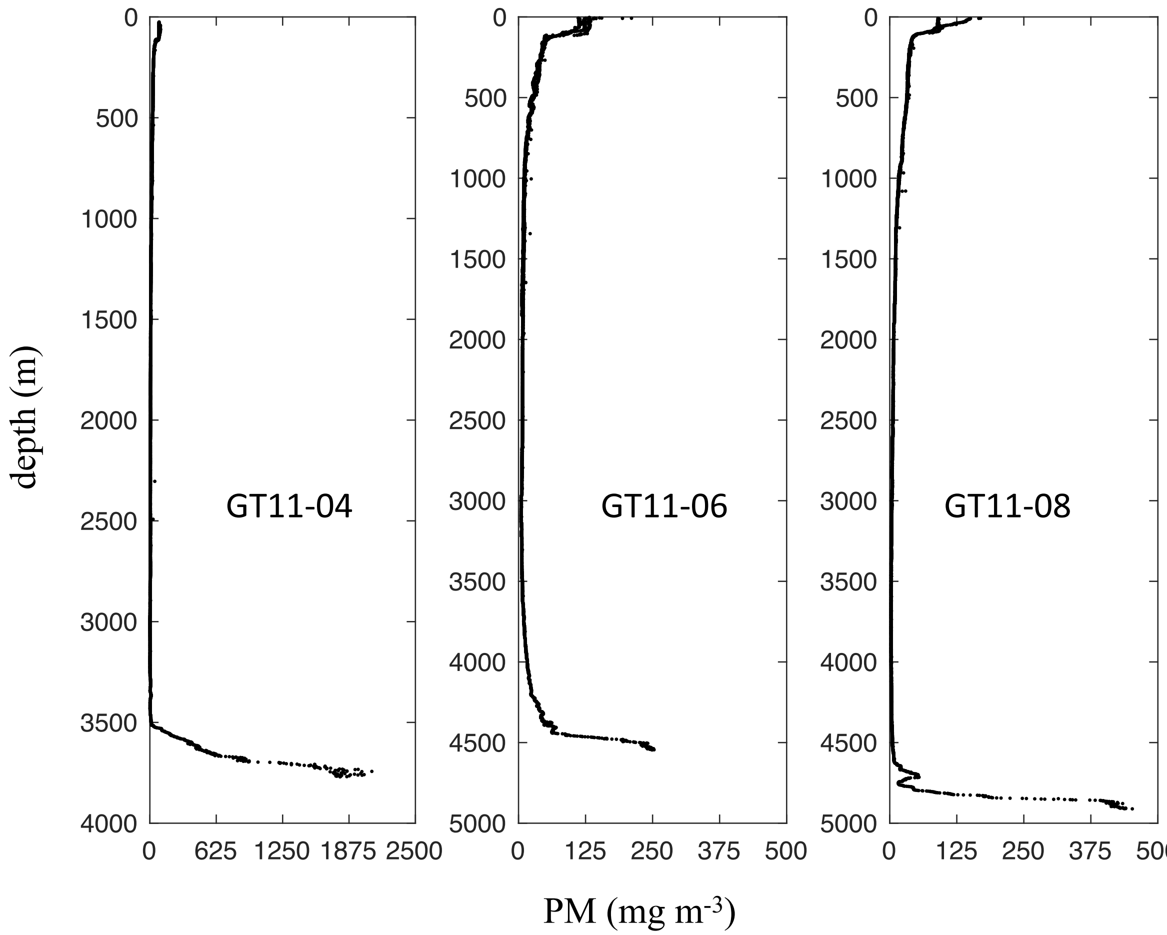

Fig. 19. Vertical profiles of optically derived particulate matter concentration at stations GT11-04, GT11-06, and GT11-08 between the New England continental shelf and Bermuda. Particulate matter concentration is estimated from beam attenuation coefficient measurements available in the GEOTRACES Intermediate Data Product (Schlitzer et al. 2018) using the empirical relationship between PM concentration and BAC due to particles as reported by Gardner et al. (2018b).

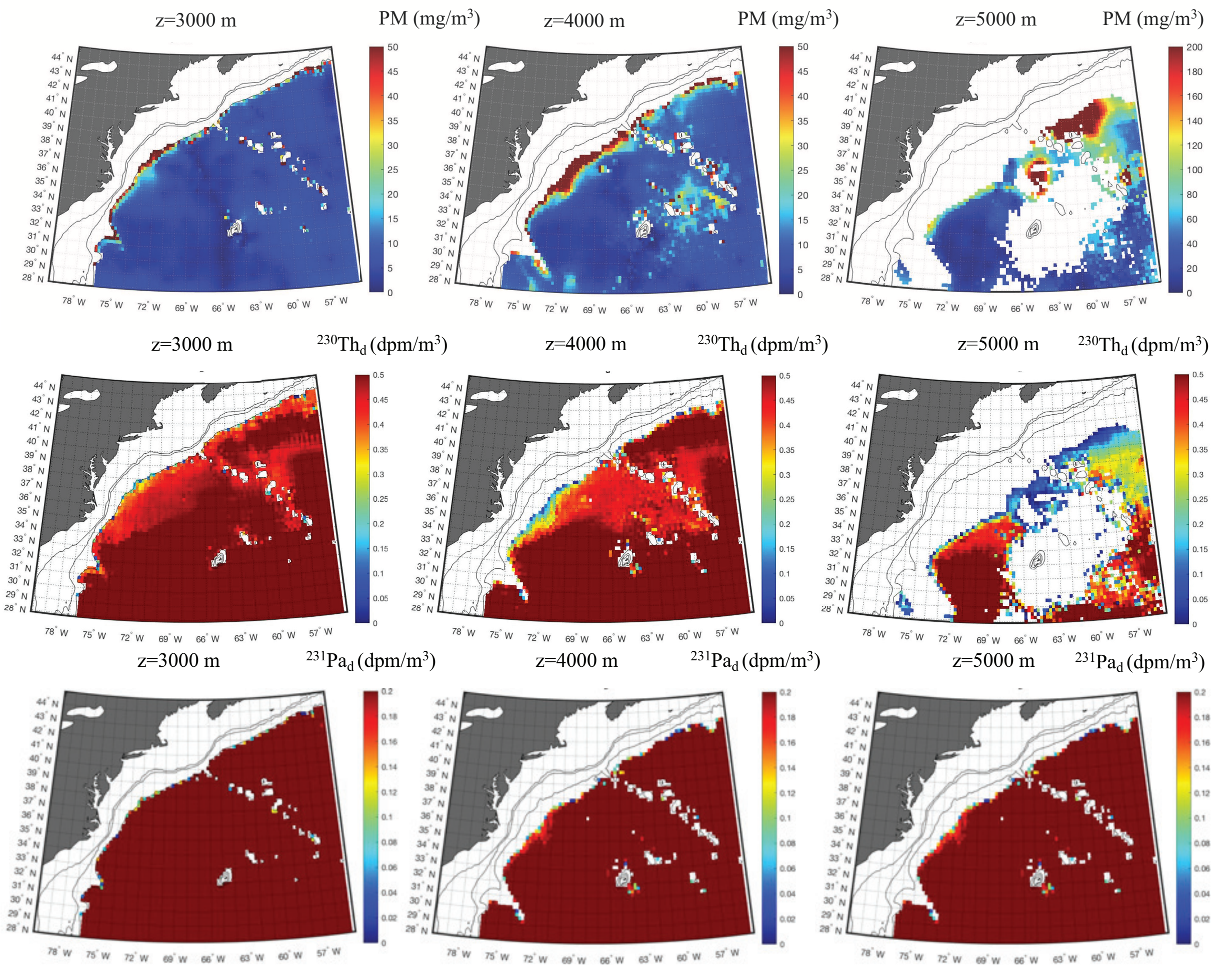

Fig. 20. Distributions of particulate matter concentration as estimated from optical measurements compiled by Gardner et al. (2017) (top three panels), $^{230}\mathrm{Th}_d$ activity as simulated in the reference solution (middle panels), and $^{231}\mathrm{Pa}_d$ activity as simulated in the reference solution (bottom panels). The left, middle, and right panels show distributions at a depth of, respectively, 3000 m, 4000 m, and 5000 m.

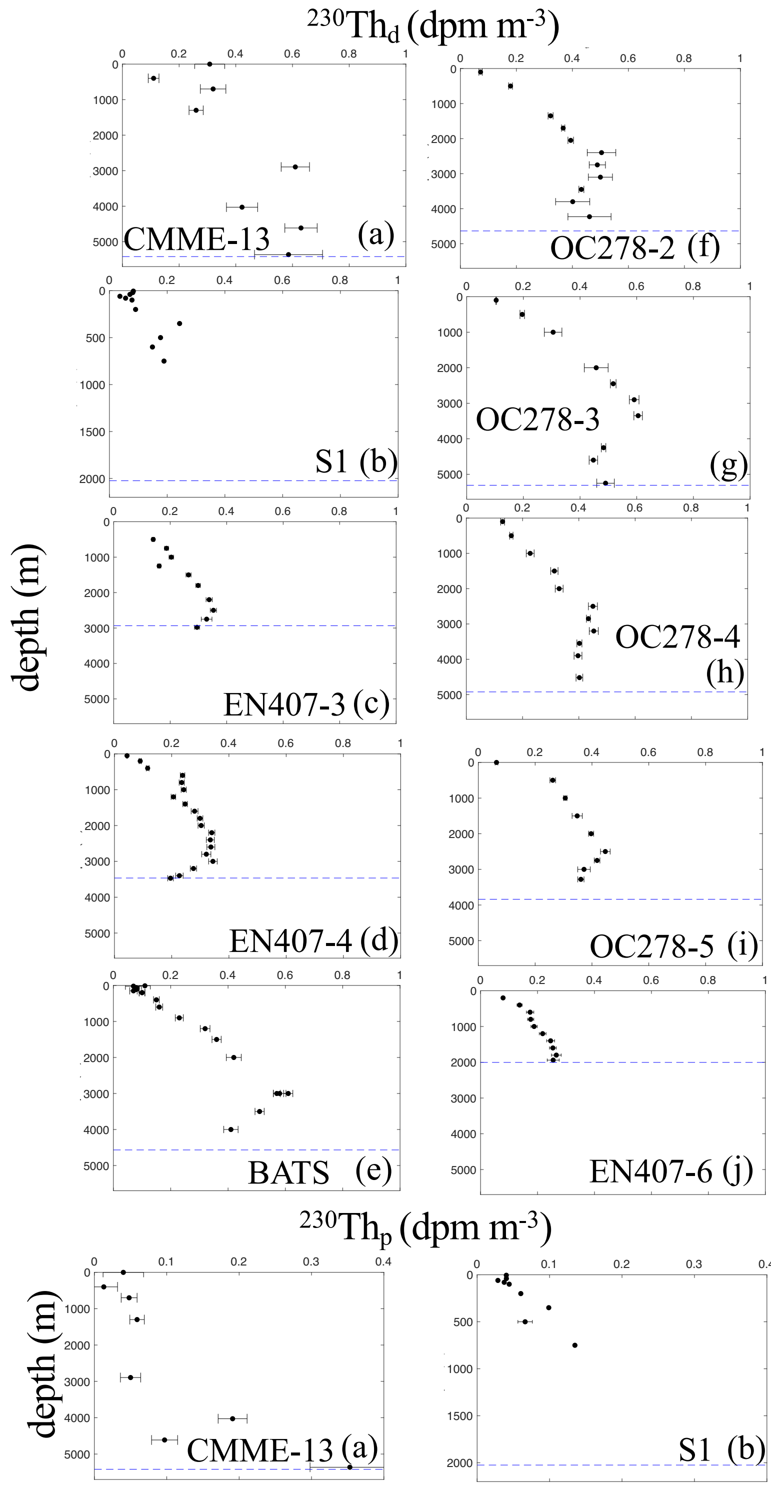

Figure A1. Profiles of dissolved and particulate ^{230}Th activities measured in the western North Atlantic prior to the GEOTRACES program. The horizontal bars show the measurement errors (Table 1), the horizontal dashed line indicates water depth (from Ryan et al. (2009)), and the stations are identified with their names and with letters located in figure 3 (see Table 1 for data sources).

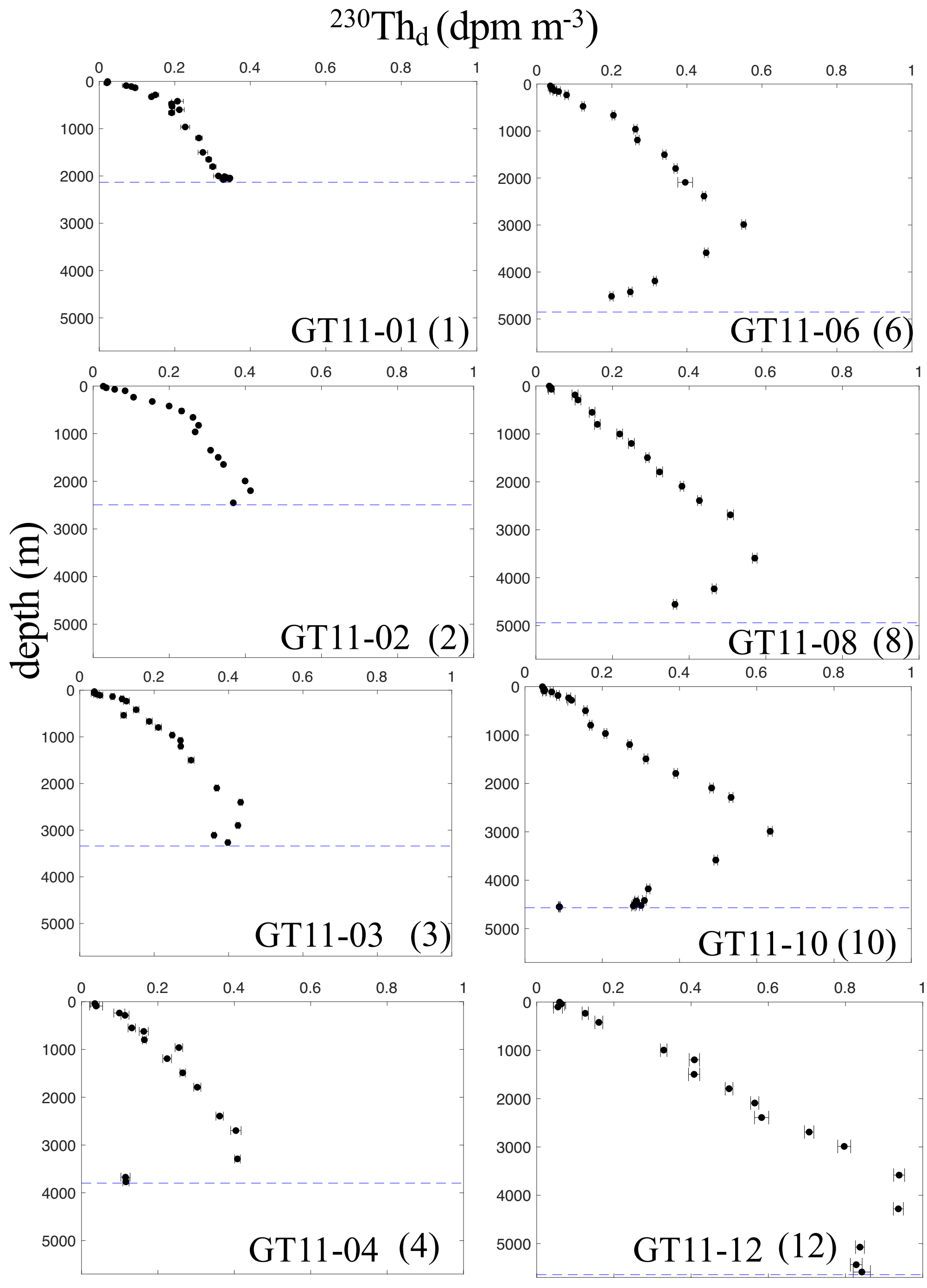

Figure A2. Profiles of dissolved ^{230}Th activity measured in the western North Atlantic along the GEOTRACES section GA03. The horizontal bars show the measurement errors (Table 1), the horizontal dashed line indicates water depth (maximum depth from CTD), and the stations are identified with their names and with numbers located in figure 3 (data from Hayes et al. (2015a)).

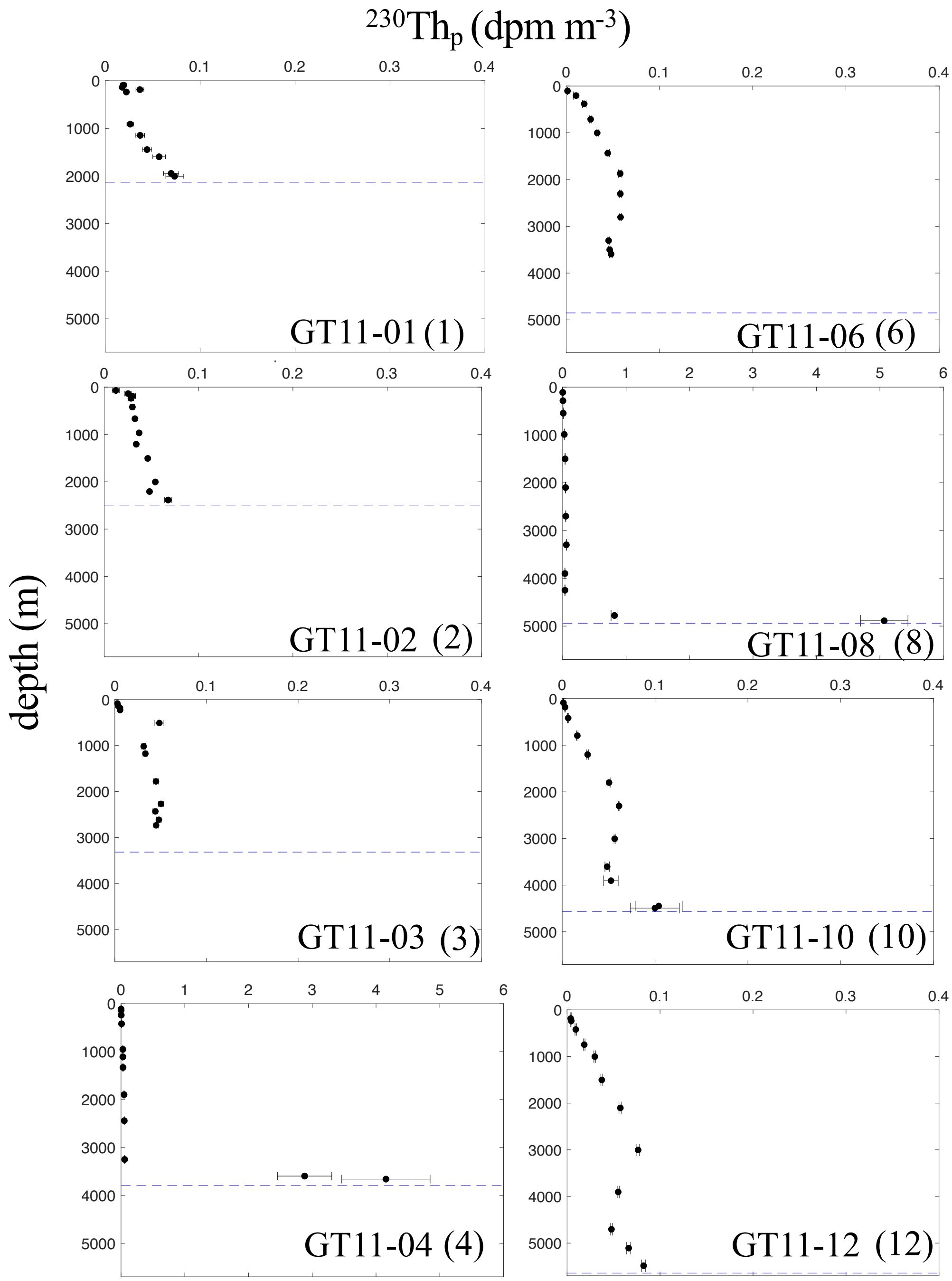

Figure A3. Profiles of particulate ^{230}Th activity measured in the western North Atlantic along the GEOTRACES section GA03. The horizontal bars show measurement errors (Table 1), the horizontal dashed line indicates water depth (maximum depth from CTD), and the stations are identified with their names and with numbers located in figure 3. Note that $^{230}Th_p$ data from stations GT11-04 and GT11-08 are plotted with a different scale than for the other stations (data from Hayes et al. (2015a)).

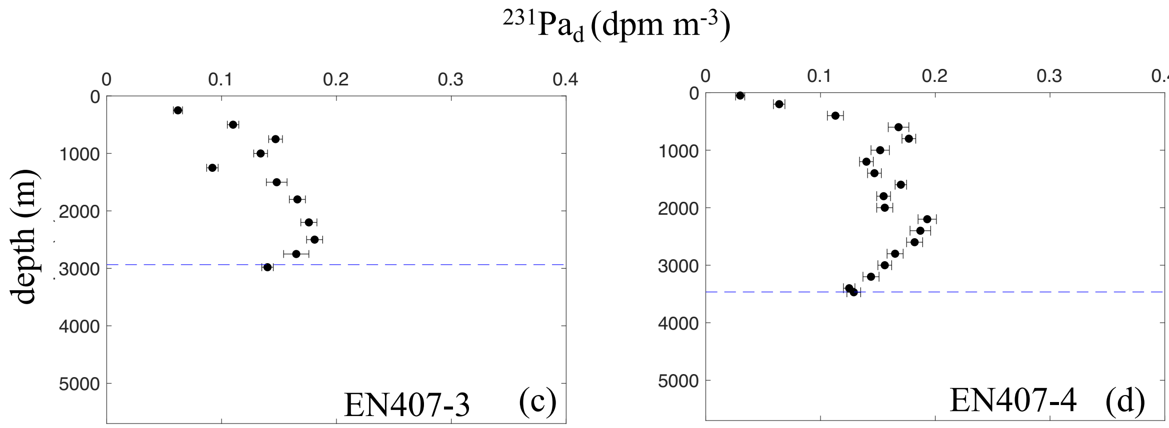

Figure A4. Profiles of dissolved ^{231}Pa activity measured in the western North Atlantic prior to the GEOTRACES program. The horizontal bars show measurement errors (Table 1), the horizontal dashed line indicates water depth (from Ryan et al. (2009)), and the stations are identified with their names and with letters located in figure 3 (see Table 1 for data sources).

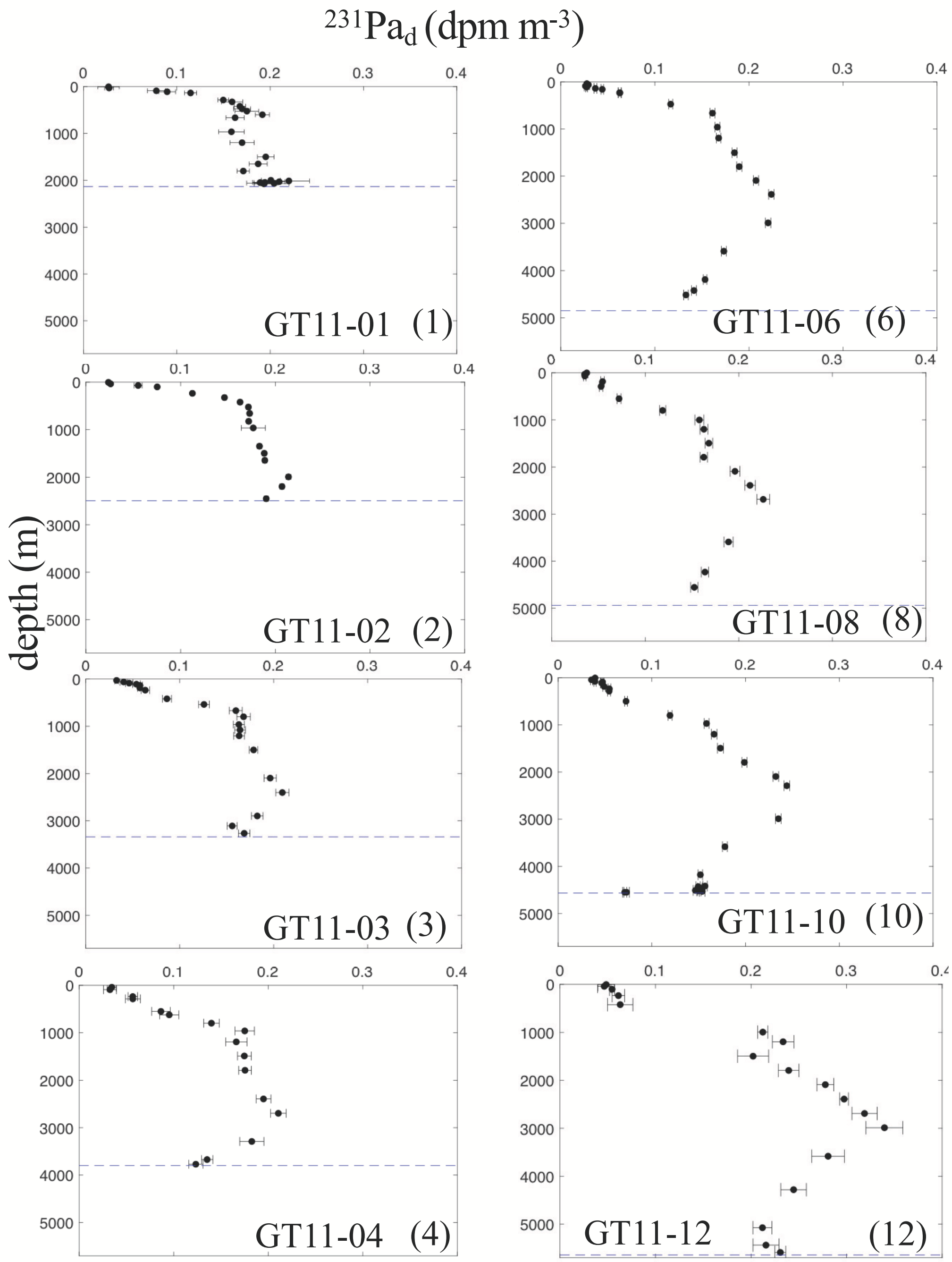

Figure A5. Profiles of dissolved ^{231}Pa activity measured in the western North Atlantic along the GEOTRACES section GA03. The horizontal bars show measurement errors (Table 1), the horizontal dashed line indicates water depth (maximum depth from CTD), and the stations are identified with their names and with numbers located in figure 3 (data from Hayes et al. (2015a)).

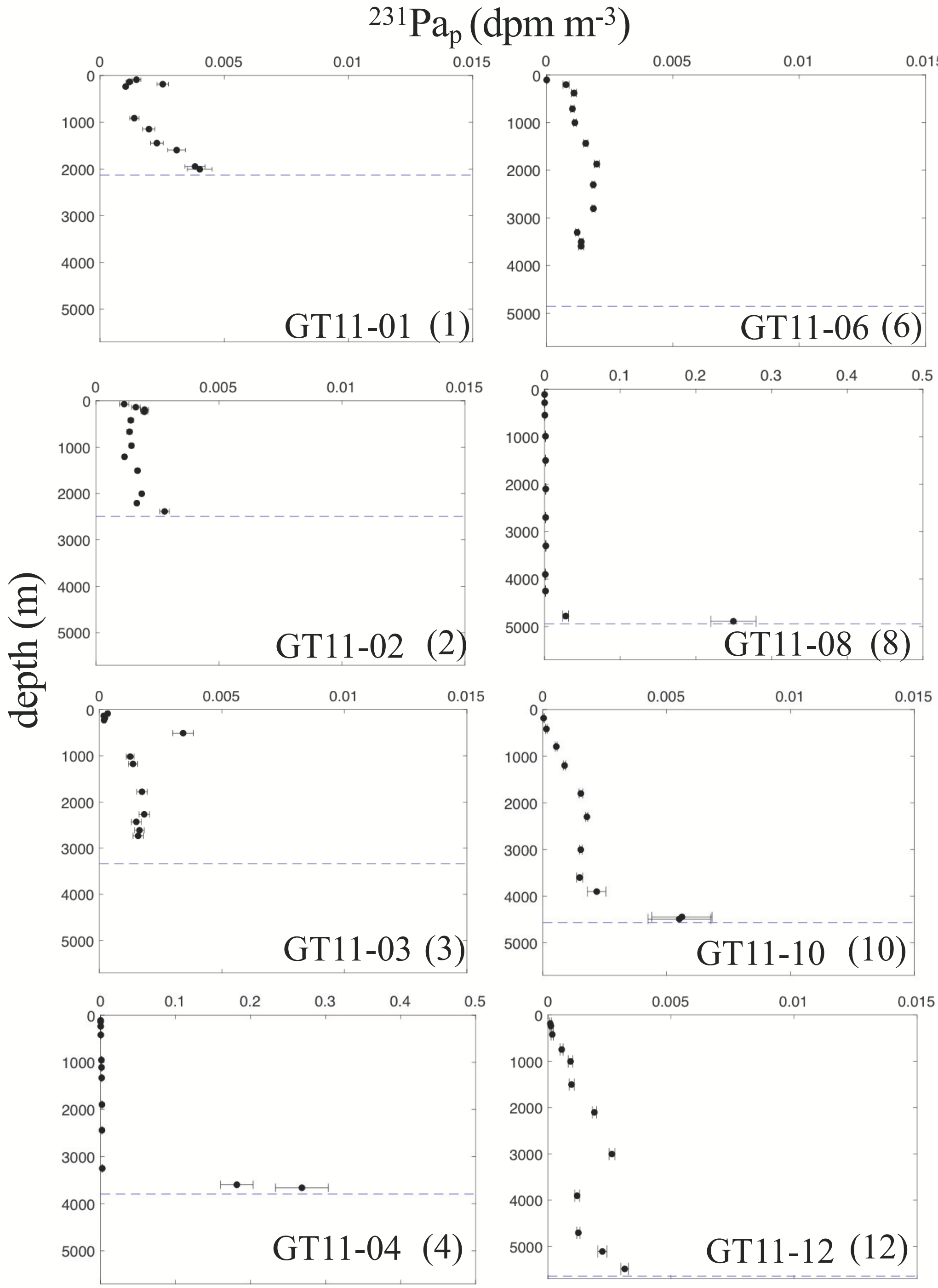

Figure A6. Profiles of particulate ^{231}Pa activity measured in the western North Atlantic along the GEOTRACES section GA03. The horizontal bars show measurement errors (Table 1), the horizontal dashed line indicates water depth (maximum depth from CTD), and the stations are identified with their names and with numbers located in figure 3. Note that $^{231}Pa_p$ data from stations GT11-04 and GT11-08 are plotted with a different scale than for the other stations (data from Hayes et al. (2015a)).

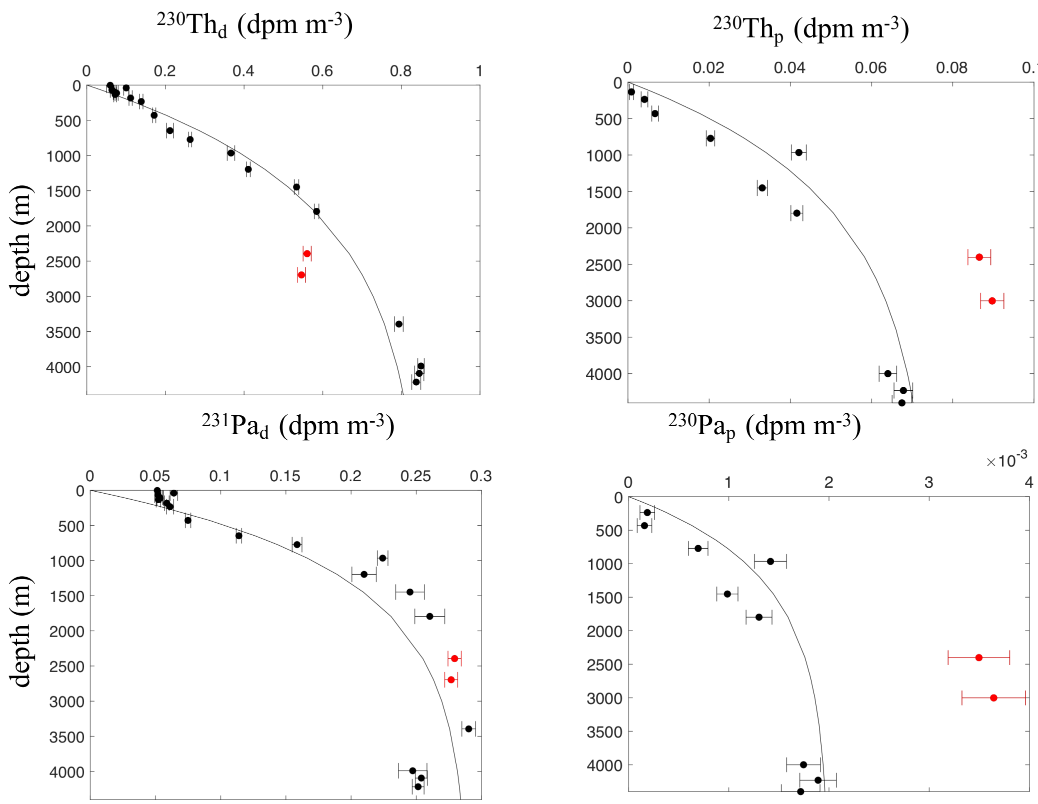

Figure A7. Profiles of $^{230}\mathrm{Th}_{d,p}$ and $^{231}\mathrm{Pa}_{d,p}$ measured at station GT11-14 (circles). The red circles are samples presumably influenced by the TAG hydrothermal vent, which is located to the east of GT11-14. The black lines are analytical profiles which approximate station GT11-14 measurements and are used as initial and lateral boundary conditions (Eq. C11). The horizontal bars show the measurement errors (Table 1; data from Hayes et al. (2015a)).

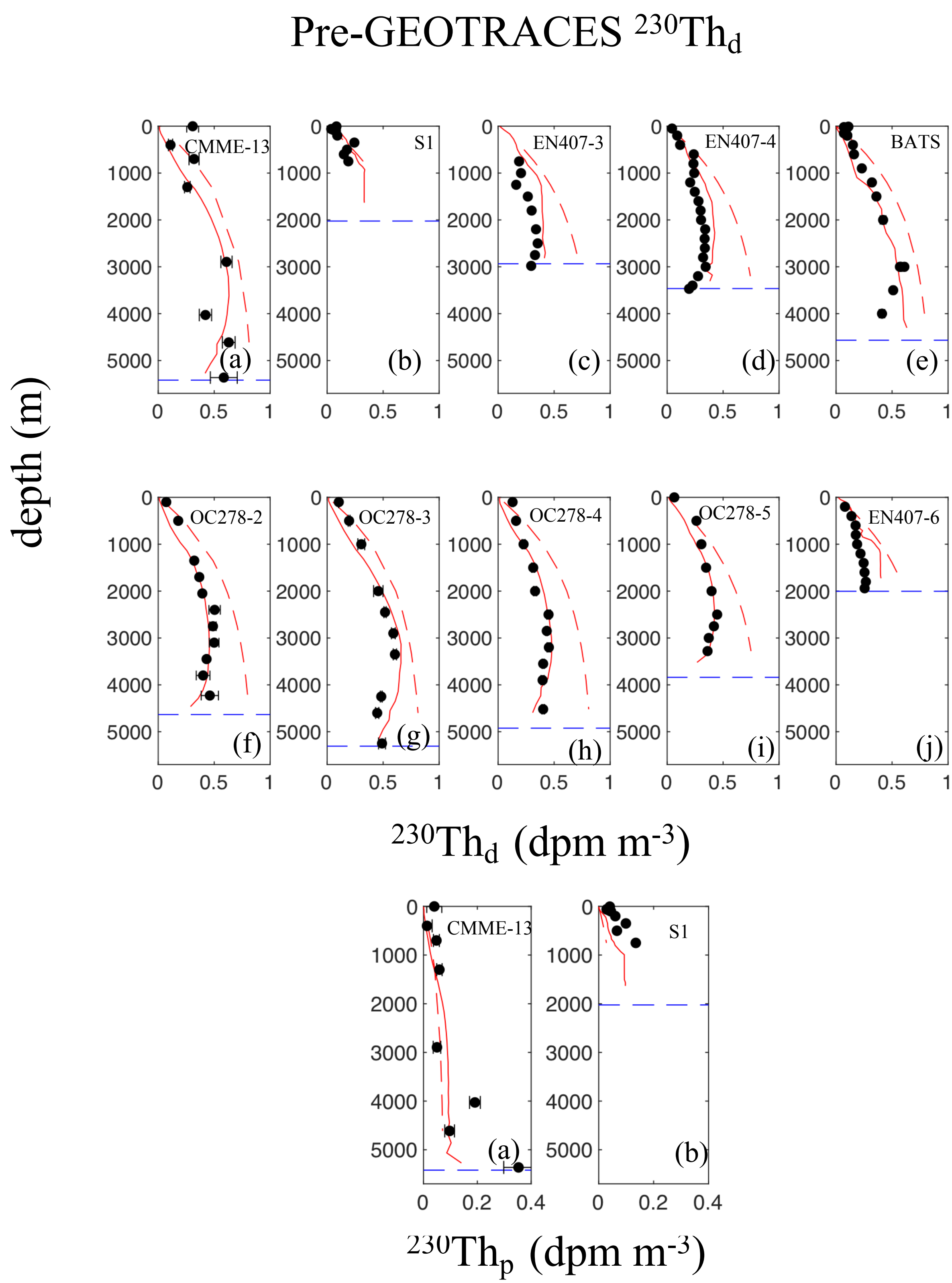

Figure A8. Profiles of $^{230}Th_d$ and $^{230}Th_p$ as measured at pre-GEOTRACES stations (black circles) and as simulated in the reference solution near these stations (red solid line). The horizontal bars show the measurement errors (Table 1), the horizontal dashed line indicates water depth (from Ryan et al. (2009)), and the red dashed line is the $^{230}Th_d$ or $^{230}Th_p$ profile used as initial conditions and prescribed at the open boundaries. The stations are identified with their names and with letters located in figure 3.

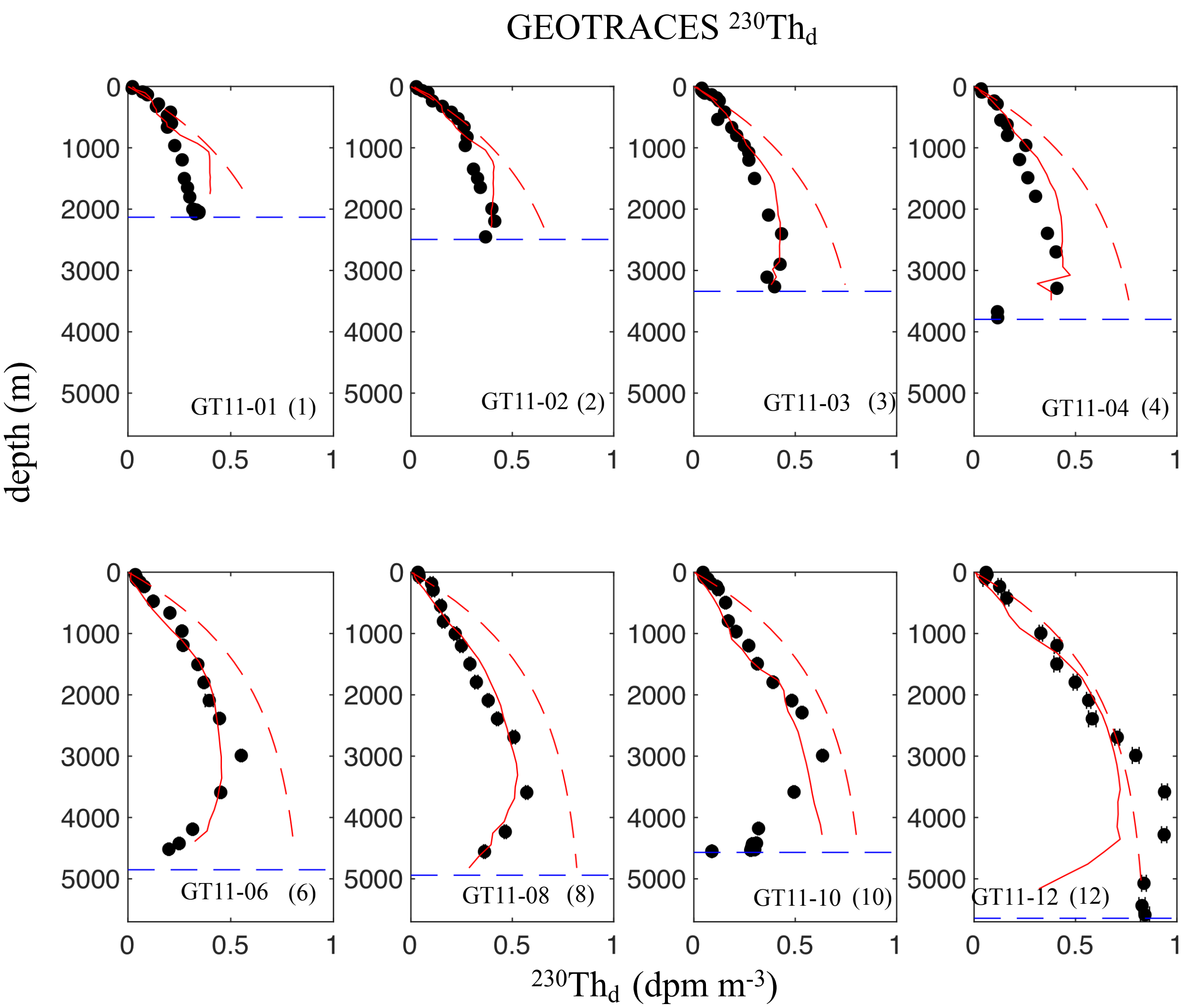

Figure A9. Profiles of $^{230}Th_d$ as measured at GA03 stations (black circles) and as simulated in the reference solution near these stations (red solid line). The horizontal bars show the measurement errors (Table 1), the horizontal dashed line indicates water depth (maximum depth from CTD), and the red dashed line in each panel is the $^{230}Th_d$ profile used as initial conditions and prescribed at the open boundaries. The stations are identified with their names and with numbers located in figure 3.

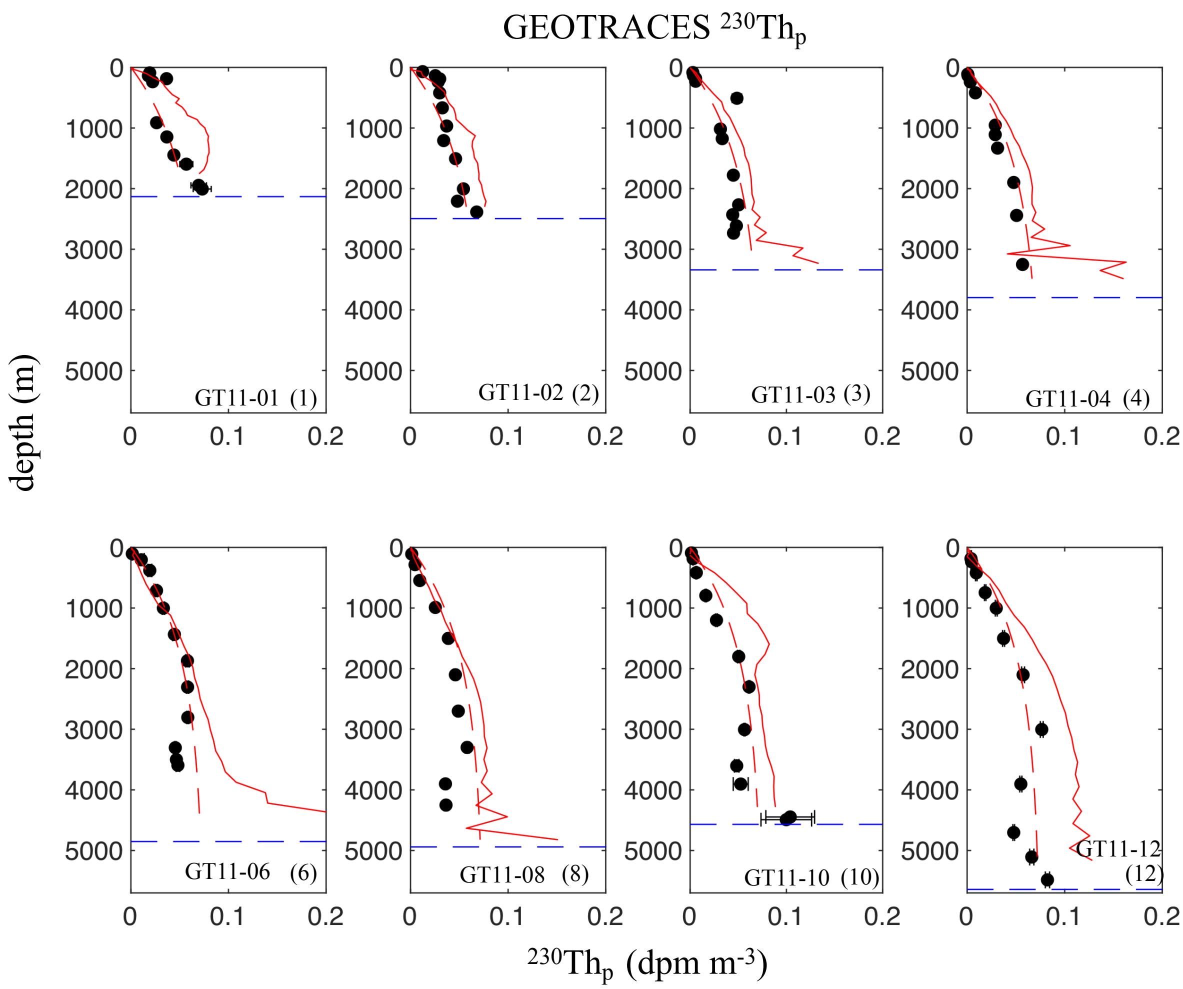

Figure A10. Profiles of $^{230}Th_p$ as measured at GA03 stations (black circles) and as simulated in the reference solution near these stations (red solid line). The horizontal bars show the measurement errors (Table 1), the horizontal dashed line indicates water depth (maximum depth from CTD), and the red dashed line in each panel is the $^{230}Th_p$ profile used as initial conditions and prescribed at the open boundaries. The stations are identified with their names and with numbers located in figure 3. The extreme values of $^{230}Th_p$ near the bottom of stations GT11-04 and GT11-8 (Fig. A3) are excluded from this figure.

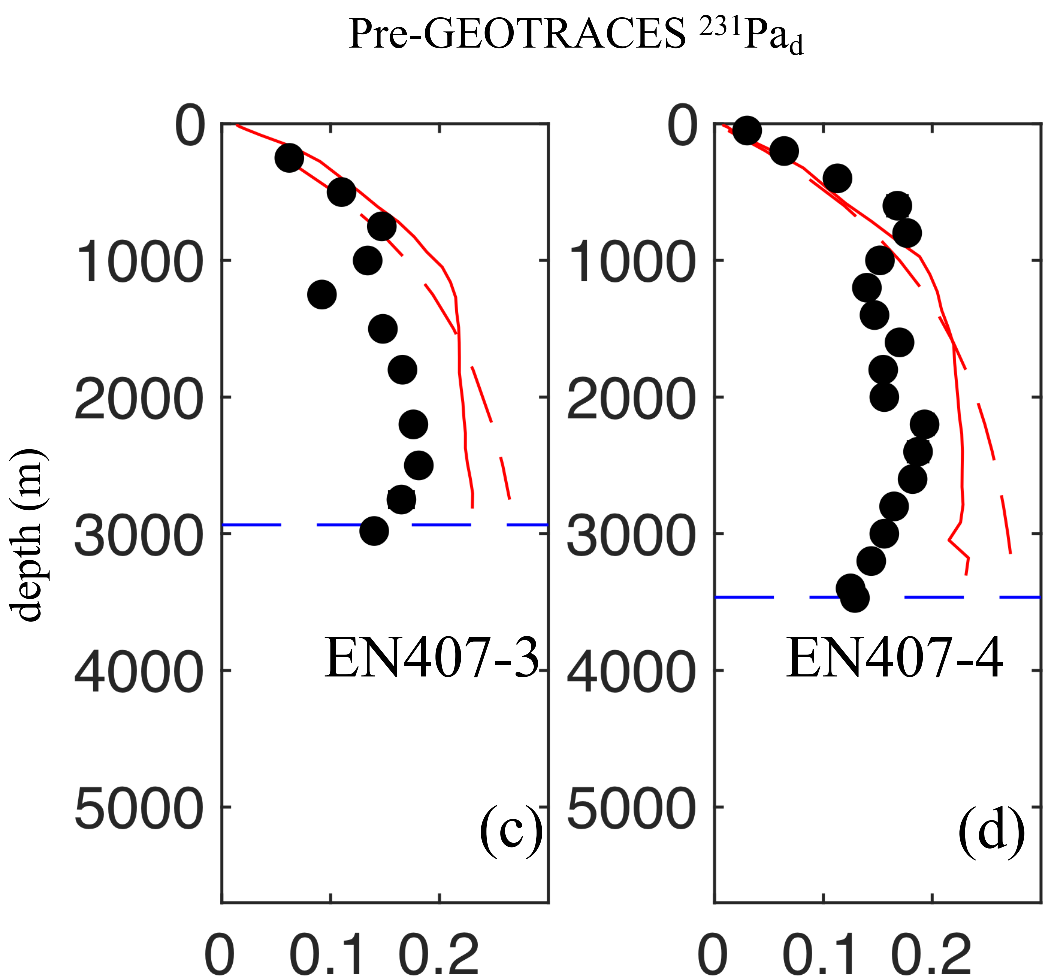

Figure A11. Profiles of $^{231}Pa_d$ as measured at pre-GEOTRACES stations (black circles) and as simulated in the reference solution near these stations (red solid line). The horizontal bars show the measurement errors (Table 1), the horizontal dashed line indicates water depth (from Ryan et al. (2009)), and the red dashed line is the $^{231}Pa_d$ profile used as initial conditions and prescribed at the open boundaries. The stations are identified with their names and with letters located in figure 3.

^{231}Pa$_d$ (dpm m^{-3})

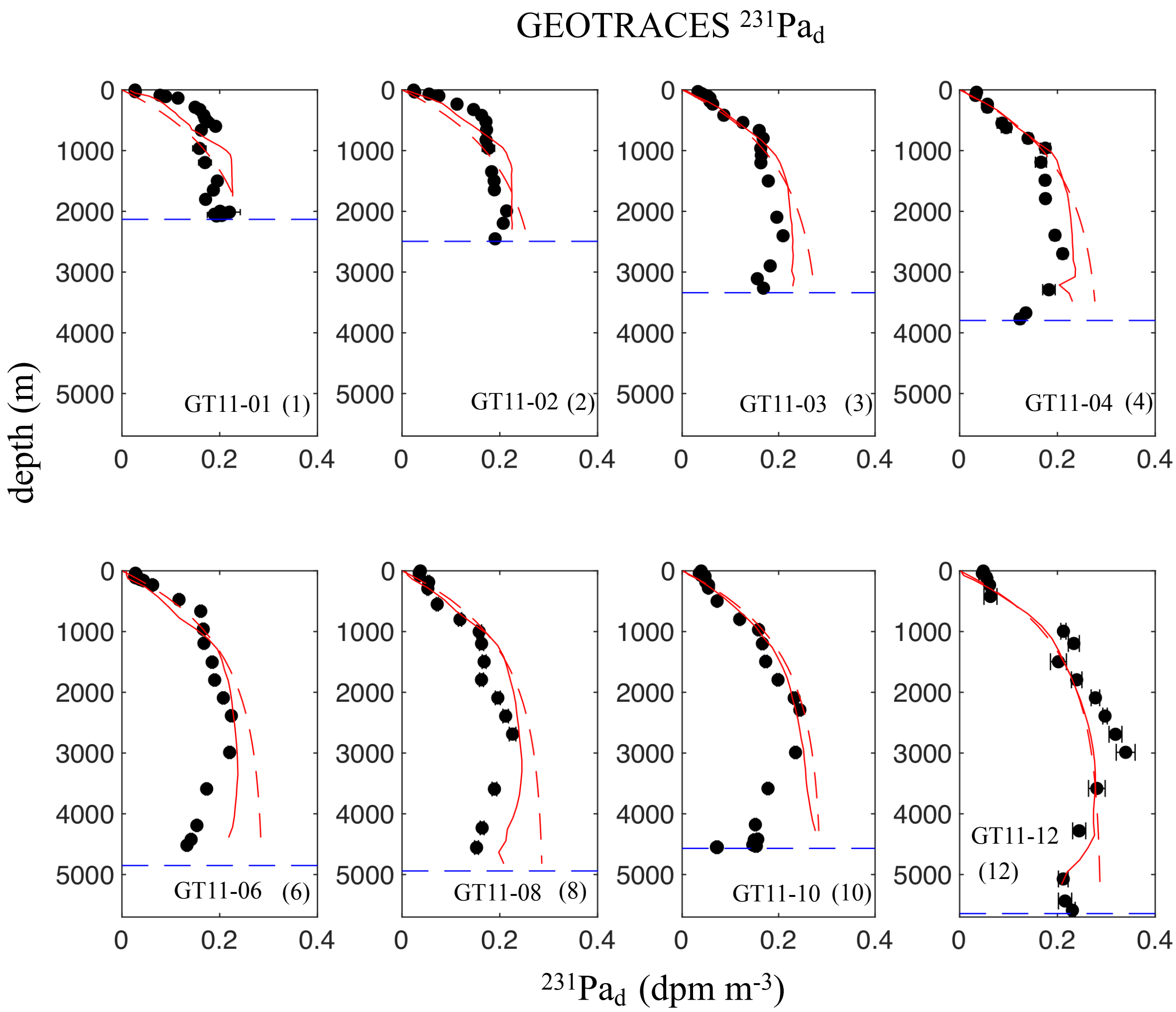

Figure A12. Profiles of ^{231}Pa$_d$ as measured at GA03 stations (black circles) and as simulated in the reference solution near these stations (red solid line). The horizontal bars show the measurement errors (Table 1), the horizontal dashed line indicates water depth (maximum depth from CTD), and the red dashed line in each panel is the ^{231}Pa$_d$ profile used as initial conditions and prescribed at the open boundaries. The stations are identified with their names and with numbers located in figure 3.

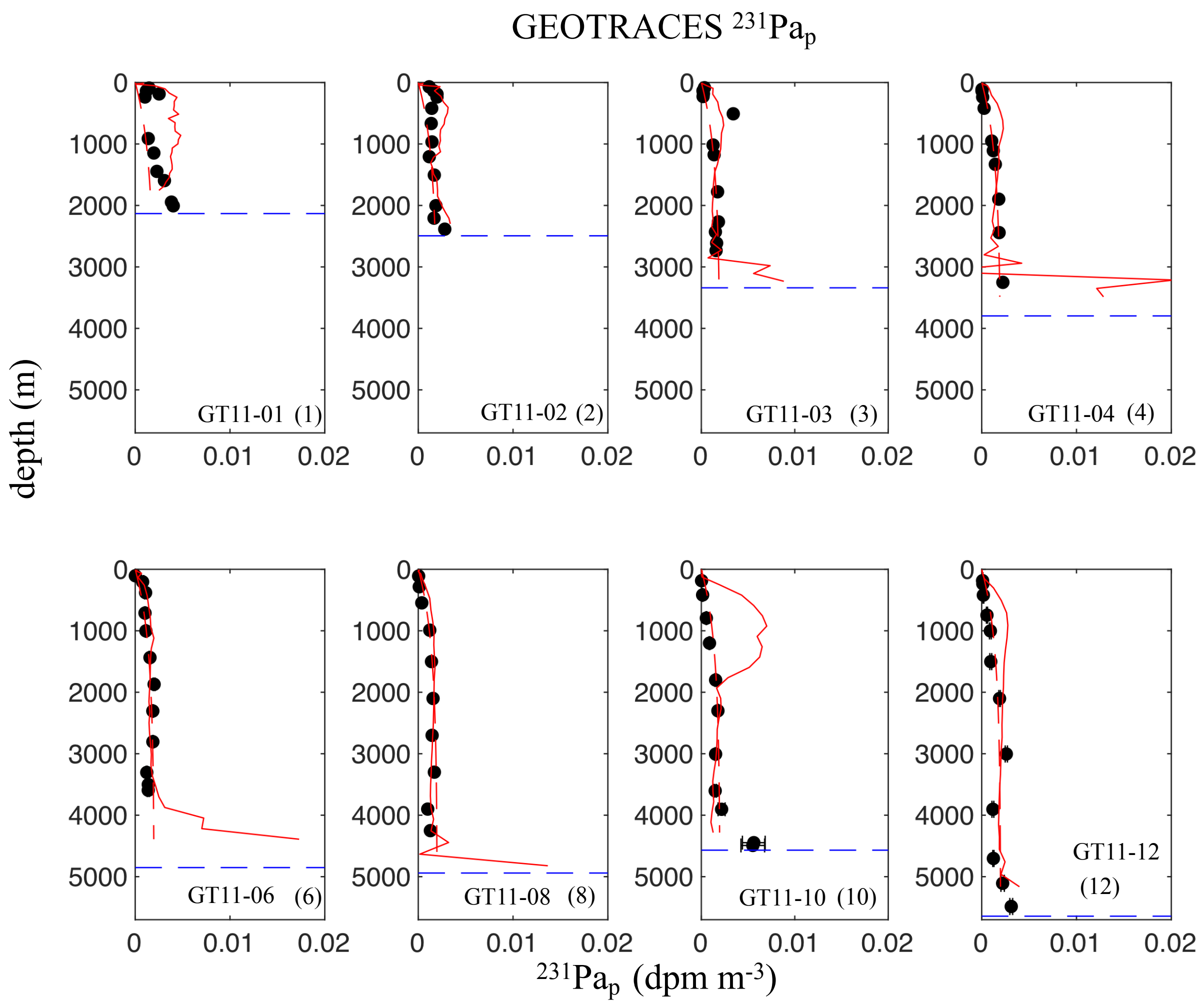

Figure A13. Profiles of $^{231}Pa_p$ as measured at GA03 stations (black circles) and as simulated in the reference solution near these stations (red solid line). The horizontal bars show the measurement errors (Table 1), the horizontal dashed line indicates water depth (maximum depth from CTD), and the red dashed line in each panel is the $^{231}Pa_d$ profile used as initial conditions and prescribed at the open boundaries. The stations are identified with their names and with numbers located in figure 3. The extreme values of $^{231}Pa_p$ near the bottom of stations GT11-04 and GT11-08 (A6) are excluded from this figure.